

## ABSTRACT

Title of Dissertation:      RESONANCES  
                                  IN  
                                  RING,  
                                  SATELLITE,  
                                  AND  
                                  PLANETARY  
                                  SYSTEMS

Thomas Rimlinger  
Doctor of Philosophy, 2020

Dissertation Directed by: Professor Douglas P. Hamilton  
                                  Department of Astronomy

In this thesis, we study the origin and evolution of planets, rings, and moons in the context of orbital dynamics. In particular, we investigate the Kepler 36 exoplanet system, which features two known planets whose semimajor axes differ by 0.01 AU but whose densities differ by nearly a factor of 10, in contrast to predictions from standard Solar System evolution theory. We use resonance and perturbation theory to show that these planets could have migrated to their current positions through a swarm of smaller bodies that knocked them progressively closer together.

We then develop a set of orbital elements designed to be used for a body orbiting an oblate host such as Saturn. Our corrections properly vanish in the limit that the oblateness terms go to 0, in contrast to the so-called “epicyclic elements,” which do not correctly reduce to their osculating counterparts. We compare the accuracy of our elements to the epicyclic elements as well as a simple numerical fit.

We also provide an explicit inverse function for our elements that transforms them back to state vectors.

Next, we study the confinement of narrow, eccentric rings. Dozens of these odd structures are known to orbit the three outer planets as well as several small bodies, but simple theory predicts they should spread on timescales as short as tens of years. The standard confinement theory suggests that these rings can be “shepherded” by nearby satellites, but most narrow rings lack such nearby satellites. We argue that by circularizing, eccentric rings can lengthen their spreading timescales by a factor of  $10^5$ . We support our theory with simulations of narrow eccentric ringlets and find that we can self-confine the Titan ringlet at Saturn.

Finally, we consider the formation and evolution of Saturn’s largest moon, Titan. No self-consistent theory exists that can explain all of its unusual features, including its enormous mass, “lonely” location within Saturn’s satellite system, and relatively high orbital eccentricity and inclination. We argue that Titan could have formed from a dynamical instability within a resonant chain of moons similar to the modern-day Galilean chain of Io, Europa, and Ganymede at Jupiter. We simulate this process for a wide variety of tidal migration and eccentricity damping strengths along with over a hundred unique possible mass distributions and find that instabilities are rare but possible.

Resonances in Ring, Satellite, and Planetary Systems

by

Thomas Rimlinger

Dissertation submitted to the Faculty of the Graduate School of the  
University of Maryland, College Park in partial fulfillment  
of the requirements for the degree of  
Doctor of Philosophy  
2020

Advisory Committee:

Professor Douglas P. Hamilton, Chair/Advisor

Professor Pamela Abshire

Dr. Joseph Hahn

Professor Coleman Miller

Professor Derek Richardson

© Copyright by  
Thomas Rimlinger  
2020

## Acknowledgments

None of this would have been possible without Bernadette's unshakeable, unending, and unconditional love and support. I also owe a massive debt to the many friends who have supported me these past years: Sarah Lee, Greta Park, Jialu Li, Sophia Alapati, Ginny Cunningham, and so many others. Of course, I also thank my sister and parents for being there for me every day of my life. Finally, I am grateful to Doug for his patient guidance each step of the way.

# Table of Contents

Acknowledgements	ii
Table of Contents	iii
Chapter 1: Introduction	1
1.1 The Two-Body Problem	1
1.2 The N-Body Problem	5
1.3 Perturbations	7
1.4 Mean Motion Resonances	9
1.5 Thesis Outline	11
Chapter 2: Exploring the Origin and Evolution of the Kepler 36 System	14
2.1 Introduction	14
2.1.1 Previous Work	14
2.1.2 Our Model	19
2.2 Simulations	21
2.2.1 Damping Forces	21
2.2.2 Collisions	22
2.2.3 Initial Conditions	25
2.3 RESULTS	27
2.3.1 Sample Simulation	27
2.3.2 Effect of a Single Collision	30
2.3.3 Individual Simulations	34
2.3.4 Summary and Mass Calculations	38
2.4 Comparison to Observations	45
2.5 DISCUSSION	50
2.5.1 Broader Implications	50
2.5.2 Limitations	51
2.6 CONCLUSIONS	52
Chapter 3: Perturbed Orbital Elements	55
3.1 Introduction	55
3.1.1 The Two-Body Problem	55
3.1.2 Epicyclic Elements	57
3.2 Alternative Choices of Elements	58
3.2.1 Analytic	58

3.2.2	Numerical . . . . .	67
3.3	Comparisons . . . . .	72
3.4	Conclusions . . . . .	76
3.4.1	Summary . . . . .	76
3.4.2	Future Work . . . . .	77
Chapter 4: Self-Confining Narrow Eccentric Rings		79
4.1	Introduction . . . . .	79
4.1.1	Observations of Narrow Rings . . . . .	79
4.1.2	Shepherd Satellites . . . . .	82
4.1.3	Our Model - An Internal Energy Source . . . . .	83
4.1.4	Self-Confinement . . . . .	86
4.2	Ring Integration with epi_int . . . . .	88
4.2.1	Self-Gravity . . . . .	89
4.2.2	Viscosity . . . . .	91
4.2.3	Numerical Error . . . . .	92
4.3	Results . . . . .	94
4.3.1	Ring Equilibra . . . . .	94
4.3.2	Addition of Viscosity . . . . .	97
4.3.3	Titan Ringlet . . . . .	98
4.4	Discussion . . . . .	101
4.4.1	Continued Model Testing . . . . .	101
4.4.2	Different Integrator . . . . .	102
Chapter 5: Titan's Unstable Origins		105
5.1	Introduction . . . . .	105
5.1.1	Background . . . . .	105
5.1.2	Orbital Evolution After Formation . . . . .	108
5.2	Integration Setup . . . . .	109
5.2.1	Initial Conditions . . . . .	109
5.2.2	Tidal Forces . . . . .	112
5.3	Results . . . . .	115
5.3.1	Overview . . . . .	115
5.3.2	Individual Simulations . . . . .	116
5.4	Discussion . . . . .	117
5.4.1	Review . . . . .	117
5.4.2	Future Work . . . . .	122
Chapter 6: Conclusions		124
6.1	Summary of Results . . . . .	124
6.2	Future Directions . . . . .	125
6.3	Facilities and Software used in this Thesis . . . . .	126

## List of Figures

1.1	<p>Depiction of an orbit (blue ellipse) relative to some reference line (black line). Points A and P are the apoapse and periapse, respectively; the orange line connecting them is the line of apses and has length <math>AP = 2a</math> for semimajor axis <math>a</math>. Point C is the center, where <math>AC = CP = a</math>. Point F is one of the two foci (the other is not labeled); the lines FP and FA are the periapse and apoapse distances, respectively, where <math>FP = a(1 - e)</math> and <math>FA = a(1 + e)</math> for eccentricity <math>e</math>. The length CF is the distance from center to focus such that <math>CF = ae</math>. The angle between the orange line of apsides and the black reference line is the argument of periapse <math>\omega</math>. Finally, point B is the location of the body, and the angle from periapse to body (i.e., between the orange line <math>\overline{FP}</math> and the green line <math>\overline{FB}</math>) is the true anomaly <math>\nu</math>, where <math>FB = \frac{a(1-e^2)}{1+e \cos \nu}</math>. For a Kepler orbit, <math>FB = r</math>. This example uses the elements <math>e = 0.7</math>, <math>\omega = 30^\circ</math>, and <math>\nu = 130^\circ</math>. . . . .</p>	12
1.2	<p>Depiction of a leapfrog integration scheme. Position <math>x</math> is updated at integer subscripts of time <math>t</math>, whereas velocity <math>v</math> is updated at half-integer subscripts. Source: <a href="https://www.astro.umd.edu/\protect\unhbox\voidb@x\protect\penalty\@M\{}ricotti/NEWWEB/teaching/ASTR415/class15.pdf">https://www.astro.umd.edu/\protect\unhbox\voidb@x\protect\penalty\@M\{}ricotti/NEWWEB/teaching/ASTR415/class15.pdf</a> . . . . .</p>	13
2.1	<p>Instances of confirmed planets with period <math>P &lt; 16</math> days, radius <math>R &lt; 4R_\oplus</math>, and period and radius errors less than one per cent, using 64 bins. The red bars correspond to planets with <math>R &lt; 1.8R_\oplus</math>, which [1] designate as super-Earths. The blue bars conversely correspond to those planets they designate as sub-Neptunes. Sub-Neptune frequency peaks at <math>P \sim 4</math> days. Data taken from the exoplanet.eu catalog and current as of 18 May 2020. . . . .</p>	17

2.2 Sample integration. We plot the mean motion ratio  $\frac{n_1}{n_2}$ , semimajor axes  $a_1$  and  $a_2$ , and eccentricities  $e_1$  and  $e_2$  of both planets. The subscripts 1 and 2 denote Kepler 36b and c, respectively. Initial planetary masses and orbital elements are as in Table 2.2. The inner planet feels no drag force (i.e.,  $k_{a,1} = 0$ ), while  $k_{a,2} = 4 \times 10^{-7} \text{ yr}^{-1}$ . The eccentricity damping strengths are  $k_{e,1} = 3 \times 10^{-4} \text{ yr}^{-1}$  and  $k_{e,2} = 10^{-7} \text{ yr}^{-1}$ . The vertical dashed lines mark entrance ( $\sim 1.25 \times 10^6 \text{ yr}$ ) and exit ( $2.0 \times 10^6 \text{ yr}$ ) into the 2:1 MMR as well as entrance into the 3:2 MMR ( $\sim 2.4 \times 10^6 \text{ yr}$ ). The effects of collisions at 0.5, 1.0, 1.5, and  $2.0 \times 10^6 \text{ yr}$  are readily apparent, particularly in the  $e_1$  plot. . . . . 29

2.3 Inner and outer  $e$  resonances for the 2:1 MMR (top two panels) and 3:2 MMR (bottom two panels), where the subscripts 1 and 2 denote Kepler 36b and c, respectively, and  $\bar{\lambda}$  and  $\varpi$  denote mean longitude and longitude of periaapse, respectively. The inner  $e$  resonance is active for both 2:1 MMR captures, whereas the outer one is only active for the second capture. . . . . 31

2.4 Two simulations showing the minimum  $\frac{\delta v}{v}$  required to eject Kepler 36b and c from the 2:1 MMR, with semimajor axis drag applied to the outer body only ( $k_{a,2} = 4 \times 10^{-6} \text{ yr}^{-1}$ ) and no eccentricity damping on either. The planets' masses are as in Table (2.2), and Kepler 36's mass is  $1.113 M_\odot$  [2]. At 3,000 yr, the planets are in the 2:1 MMR, and at 5,000 yr, we apply a kick to the inner body in the  $\hat{v}$  direction. For  $\frac{\delta v}{v} = 0.00166$  (the blue curve), corresponding to an estimated impactor mass of  $2.17 M_{\text{Moon}}$ , the bodies remain in resonance but librate with a much greater amplitude. For  $\frac{\delta v}{v} = 0.00167$  (the green curve), corresponding to an estimated impactor mass of  $2.18 M_{\text{Moon}}$ , the bodies exit resonance. . . . . 33

2.5 Example of permanent 7:6 capture with four collisions, at 0.5, 1, 1.5, and  $2 \times 10^6 \text{ yr}$ . We display results between  $0.9$  and  $2.5 \times 10^6 \text{ yr}$  to highlight the interesting behavior therein. The top panel shows the mean motion ratio of the two planets; the second and third show the inner and outer planetary semimajor axes; and the fourth and fifth show the inner and outer planetary eccentricities. We denote entry into and exit from resonance with dotted vertical lines; the specific resonances are noted, although we are unsure of the 4:3 (see text). Our disk parameters were  $k_{a,1} = 5 \times 10^{-8} \text{ yr}^{-1}$ ,  $\frac{k_{e,1}}{k_{a,1}} = 1$ ,  $\frac{k_{e,2}}{k_{a,2}} = 30$ , and  $k_{a,2} = 4 \times 10^{-7} \text{ yr}^{-1}$ . Given typical impactor eccentricities of 0.25, we estimate that the inner body accreted  $\sim 1.50 M_\oplus$ , ending with  $4.8 M_\oplus$  – about 10 per cent above the observed value of  $4.45 M_\oplus$  (see Table 2.1). . . . . 35

2.6	Example of permanent 7:6 capture with nine collisions. We display only results between 2 and $6 \times 10^6$ yr. As in Fig. 2.5, the mean motion ratio in the interval marked “4:3 (?)” librates about an unusual value (here $\sim 1.364$ ); we are again unsure if this truly is the 4:3 MMR. Our disk parameters were $k_{a,1} = 2 \times 10^{-7} \text{ yr}^{-1}$ , $\frac{k_{e,1}}{k_{a,1}} = 30$ , $\frac{k_{e,2}}{k_{a,2}} = 1$ , and $k_{a,2} = 4 \times 10^{-7} \text{ yr}^{-1}$ . We estimate that the inner body accreted $\sim 1.89M_{\oplus}$ , ending with $5.19M_{\oplus}$ . . . . .	37
2.7	Example of permanent 7:6 capture with fifteen collisions. We display only results between 3 and $9 \times 10^6$ yr. Our disk parameters were $k_{a,1} = 10^{-7} \text{ yr}^{-1}$ , $\frac{k_{e,1}}{k_{a,1}} = 30$ , $\frac{k_{e,2}}{k_{a,2}} = 300$ , and $k_{a,2} = 4 \times 10^{-7} \text{ yr}^{-1}$ . We estimate that the inner body accreted $\sim 4.63M_{\oplus}$ , ending with $7.33M_{\oplus}$ . . . . .	39
2.8	Final estimated mass, using three different assumptions for $e_i$ , for each simulation that ended in or near the 7:6 MMR. The solid black line indicates Kepler 36b’s current observed mass. . . . .	40
2.9	Number of simulations that ended in or near the 7:6 MMR for each number of collisions $N$ . Little more than the broad outlines of a pattern can be seen. . . . .	42
2.10	Simulated (top) versus observed (bottom) resonance incidence for selected MMRs. In the simulated plot, we refer to the resonance in which each simulation ended; we have excluded simulations that ended with swapped planetary positions (1,923 of 7,020 total), did not end in resonance (172), or ended in an unidentified resonance (327). Observed data is taken from exoplanet.eu and is current as of 18 May 2020; we only include confirmed, radially adjacent planets with period errors known to be less than one per cent. Results for $\xi = 1, 0.75$ , and $0.5$ are shown overlaid upon each other (see text). As $\xi$ decreases, the observed data increasingly resembles the simulated data, most notably for $\xi = 0.5$ (blue). . . . .	49
3.1	Typical average eccentricity $e$ error (green) and semimajor axis $a$ error (red) versus number of points $N$ from our numerical fit using $\gamma = 20$ , i.e., in which we print twenty times per orbit. We have normalized the error by the true quantity; that is, we define the error in a quantity $x$ as $\frac{ x_{\text{true}} - x_{\text{calc}} }{x_{\text{calc}}}$ , where $x_{\text{true}}$ is the true value of $x$ and $x_{\text{calc}}$ is the calculated value. Ellipse parameters were $a = 1$ and $e = 0.001$ ; we rotated the periapse point 0.01 radians counter-clockwise each output. We have marked the $N$ corresponding to the first dip for both sets of errors. . . . .	70

3.2	Doubly averaged errors on $a$ and $e$ versus output interval (i.e., $\frac{1}{\gamma}$ ). Whereas in Fig. (3.1), each plotted point was the average error over a simulation, here the point at output interval = $\frac{1}{20} = 0.05$ in the top panel is the average of all red points from $N = 30$ to 70 in Fig. (3.1); likewise for the bottom panel and green points. The other points in each panel are similar averages for different choices of output interval. All simulations were again performed using $a = 1$ and $e = 0.001$ with periapse rotation of 0.01 rad per output. The inset in the bottom panel zooms in on the output interval from 31.46 to 31.49, showing the large dip in errors there; this is discussed further in the text. . . .	71
3.3	The geometric $a$ (top) and $e$ (middle), and $q$ error (bottom) for ten orbits of a test particle around Saturn. The dark blue curve is the epicyclic elements, the cyan curve is the fitted numerical elements, and the green curve is the analytic elements. The dotted lines in the bottom plot are the average $q$ error values. The numerical elements appear to perform best; their average $q$ error is closest to 0, and the libration amplitude for both $q$ error and $e$ is lower than that of the other two sets. . . .	74
3.4	Average $q$ error of analytic (green), numerical/fitted (cyan), and epicyclic (blue) elements. The sizes of the circles signify the relative $q$ amplitudes but are NOT to scale. We show results for $e \approx 0.1J_2$ (top panel), $e \approx J_2$ (middle panel), and $e \approx 10J_2$ (bottom panel). Results for Earth, Uranus, and Saturn are displayed in the left, middle, and right columns, respectively. The simulation from Fig. (3.3) is summarized in the top panel's Saturn column. We logarithmically space the columns according to the planetary $J_2$ . The fitted elements always have the lowest error and have the lowest amplitude in every case except at Uranus with $e \approx 10J_2$ and at Saturn with $e \approx J_2$ . . . .	75
4.1	Schematic showing the energy cycle of a non-spreading ringlet. In the top left diagram (1), pericenter collisions kick the innermost ringlet further inwards. In (2) and (3), this ringlet then begins to circularize and differentially precess until the point of closest approach between the ringlet and the rest of the ring is close enough to begin transferring energy in (4). This leads the ring back to its initial configuration with a slightly lower eccentricity. . . .	87

4.2	<p>Display of the fractional <math>z</math> component of angular momentum <math>\frac{ \Delta L_z }{ L_z }</math> for four two-dimensional ring simulations that differ only in their timesteps. The rings have eccentricity <math>e = 0.005</math> and density <math>\sigma = 10^{-6}</math> in units of <math>M_{\text{Saturn}} = 5.6846 \times 10^{29}</math> g and <math>r_{\text{ring}} = 1.178145 \times 10^{10}</math> cm. For ease of comparison to theory, we use two streamlines, each with 250 particles. The initial semimajor axes of the two streamlines are <math>1.0005 r_{\text{ring}}</math> and <math>0.9995 r_{\text{ring}}</math>. The initial <math>\Delta e</math> is <math>10^{-5}</math>. There is no viscosity. The timestep for the simulation corresponding to the dark blue line is five orbits, while the timestep for the simulation represented by the green line is 0.5 orbits, etc. The green and red lines nearly lie atop each other. Note the linear growth in angular momentum error as the number of timesteps increases, regardless of the actual timestep value. Even varying the timestep over several orders of magnitude does little to change the rate of growth. . . . .</p>	93
4.3	<p>Three plots displaying the evolution of a ring that has been slightly perturbed from its equilibrium. The simulated libration time agrees very well with that predicted by [3] (see text). Initial conditions are identical to those in Fig. 4.2 – the only forces active are the ring’s self-gravity and the gravity from the oblate host planet. Our timestep was five orbital periods. From top to bottom, the panels feature the difference between outer and inner longitudes of periapse, the <math>q</math> parameter, and the difference <math>\Delta a</math> between the center of the ring and its edge, equal to half the width of the ring. . . . .</p>	94
4.4	<p>Five simulations of librating ringlets identical except for timestep. Only the differences in longitudes of periapse have been plotted. The blue curve has a timestep of 0.016 orbital periods, green has 0.08 orbital periods, red has 0.16, cyan 0.32, and magenta 0.63. Despite the wide range of stepsizes, all curves maintain very similar libration periods. . . . .</p>	96
4.5	<p>Several plots describing the evolution of a viscous, self-gravitating, narrow eccentric ringlet of two streamlines with sixteen particles per streamline. The ring is initialized with <math>\Delta a = 10^{-4} r_{\text{ring}}</math>, <math>e = 10^{-3}</math>, <math>\Delta e = 10^{-5}</math>, and <math>\sigma = 4.4 \times 10^{-8}</math> in the units of Fig. 4.2. Both shear and bulk viscosity equaled <math>2114 \text{ cm}^2 \text{ s}^{-1}</math>. While these viscosity values are about an order of magnitude greater than is typical [4], they permitted us to greatly speed up the simulation while retaining a similar, if accelerated, evolution. The top panel features the difference between outer and inner longitudes of periapse. The second and third, and fourth panels from the top feature the <math>q</math> parameter, the eccentricity gradient term <math>a \frac{de}{da}</math>, and the inner and outer eccentricities <math>e_{in}</math> and <math>e_{out}</math>, respectively. The fifth panel shows <math>\frac{\Delta L}{L}</math>, which is consistently <math>&lt; 10^{-7}</math> until the spike at the end indicating the onset of numerical instability. The bottom panel shows the difference <math>\Delta a</math> between the center of the ring and its edge, equal to half the width of the ring. . . . .</p>	97

4.6	Several plots describing a possible evolutionary path of the Titan ringlet. In this two-dimensional simulation, the ring spreads until $t \sim 110$ , but then contracts until $t \sim 150$ . The reason for such contraction is easiest to see via panel 1 – the ring “overshoots” the equilibrium twist value and starts to compensate. After briefly spreading again, it reaches its equilibrium at $t \sim 300$ and remains confined. All parameters of the host planet (e.g., mass, radius, etc.) are again equal to those of Saturn. The initial inner and outer semimajor axes are $1 - 1.6 \times 10^{-6}$ and $1 + 1.6 \times 10^{-6}$ respectively, using a length unit of $7.7871 \times 10^9$ cm (see Table 4.1). The initial eccentricity of the inner streamline is 0.00026, while the initial $\Delta e$ is 0. The ring begins with a very small pericenter twist of $-0.062^\circ$ . Both shear and bulk viscosity parameters are $63.4 \text{ cm}^2 \text{ s}^{-1}$ . Density is $8.93 \text{ g cm}^{-2}$ . The ring is in equilibrium from $t \sim 300$ to the end of the integration. . . .	99
4.7	Identical to Fig. 4.6 except run for ten times longer. While the ring is in equilibrium and the eccentricity is above $e_{crit}$ , i.e., from $t \sim 300 - 1300$ , the ring spreads quite slowly, although once it is sufficiently circular, the spreading timescale shortens considerably. . .	100
5.1	Dynamical instability among an initially resonant chain of satellites. We plot semimajor axis $a$ (blue), periapse distance $q$ (red), and apoapse distance $Q$ (green) for all three bodies. We used $\frac{k_{2p}}{Q_p} = 10^{-3}$ and $\frac{k_{2s}}{Q_s} = 6 \times 10^{-4}$ with a mass distribution of $\log_2 \left( \frac{m_2}{m_1} \right) = -4$ and $\log_2 \left( \frac{m_3}{m_1} \right) = -1.5$ and a speed-up factor $C$ of 1000. The middle satellite’s orbit almost immediately crosses both of its neighbors’, and it is ejected at $\sim 140$ Myr. We have scaled the time axis accordingly with our speed-up factor. . . . .	118
5.2	Five notable resonant arguments for the simulation in Fig. 5.1. From top down: the Laplace resonance argument $\varphi_L$ , the inner and outer eccentricity resonance arguments $\varphi_{21,i}$ and $\varphi_{21,o}$ , respectively, between bodies 1 and 2, and the inner and outer eccentricity resonance arguments $\varphi_{32,i}$ and $\varphi_{32,o}$ , respectively, between bodies 2 and 3. All resonances are active for most of the simulation, as denoted by the libration of their arguments around fixed values. In particular, both the outer eccentricity resonance between bodies 1 and 2 and the inner eccentricity resonance between bodies 2 and 3 are active, rapidly forcing up the eccentricity of the middle satellite. . . . .	119

5.3	Crossing orbits, but no dynamical instability, between an initially resonant chain of satellites (compare with Fig. 5.1). We again used $\frac{k_{2P}}{Q_P} = 10^{-3}$ and $\frac{k_{2s}}{Q_s} = 6 \times 10^{-4}$ but with a mass distribution of $\log_2\left(\frac{m_2}{m_1}\right) = -4$ and $\log_2\left(\frac{m_3}{m_1}\right) = -2.5$ and a speed-up factor $C$ of 100. The middle satellite's orbit almost immediately crosses that of the inner body, but not the outer body, and the system does not go unstable. Again scaling our time accounting for the speed-up factor, we integrated for 4 Gyr. We show only the time up to 700 Myr to highlight the interesting behavior at the beginning of the integration.	120
5.4	The same resonant arguments as plotted in Fig. 5.2, now for the simulation presented in Fig. 5.3. All resonances are initially active, but following a significant perturbation at $\sim 250$ Myr, $\varphi_{32,o}$ permanently ceases libration even as the others eventually recover.	121

## Chapter 1: Introduction

This thesis is focused on the orbital motions of rings, moons, and planets. We extensively use orbital elements, perturbation theory, and numerical integration in the main body of the thesis and accordingly supply a brief introduction to those topics here.

### 1.1 The Two-Body Problem

To a decent approximation, all major Solar System bodies from Mercury to Pluto follow circular orbits around either the Sun or a planet. On closer inspection, of course, this model falls apart; sufficiently precise observations of the planets' positions, for example, are incompatible with circular orbits regardless of what they are centered on. Kepler's model, as outlined by his three "Laws," is much more accurate. Planets are now assigned elliptical orbits with one focus at the Sun (the First Law), they sweep out equal areas in equal times (the Second), and the square of their periods is proportional to the cube of their orbital semimajor axes (the Third). Although originally found empirically for the planets, these laws can be derived for any two masses  $M$  and  $m$  interacting solely via gravity using just two equations and the assumption that  $M \gg m$ . This assumption is appropriate for planets orbiting

the Sun as well as satellites or rings orbiting a planet – such orbits are called “Kepler orbits” – and will be used for the rest of this thesis unless otherwise noted.

First, we need Newton’s law of gravitation describing the force  $\mathbf{F}_g$  between two masses separated by a displacement vector  $\mathbf{r}$ :

$$\mathbf{F}_g = -\frac{GMm}{r^3}\mathbf{r}, \quad (1.1)$$

where  $G \approx 6.67430 \times 10^{-11} \text{ m}^3 \text{ kg}^{-1} \text{ s}^{-2}$  is the universal gravitational constant and  $r = |\mathbf{r}|$ . We also need Newton’s Second Law,  $\mathbf{F} = m\ddot{\mathbf{r}}$ , equating the force  $\mathbf{F}$  upon a body of mass  $m$  to the acceleration  $\ddot{\mathbf{r}}$  it experiences. With these additions, we can rewrite Eq. (1.1) as:

$$\ddot{\mathbf{r}} = -\frac{GM}{r^2}\hat{\mathbf{r}}, \quad (1.2)$$

where  $\mathbf{r} = r\hat{\mathbf{r}}$ .

We can now sketch the derivation of Kepler’s Laws; interested readers can consult, e.g., [5] or [6] for more detail. By crossing both sides of Eq. (1.2) with  $\mathbf{r}$  and integrating, one can show the existence of a conserved quantity: the *angular momentum* per unit mass  $\mathbf{h} = h\hat{\mathbf{h}} = \mathbf{r} \times \dot{\mathbf{r}}$ . This leads immediately to Kepler’s Second Law; one finds that  $\dot{A} = \frac{h}{2}$ , where  $A = \int_{t_1}^{t_2} \dot{A} dt$  is the area of the orbit swept out between arbitrary times  $t_1$  and  $t_2$ . Next, by taking the second time derivative of  $\mathbf{r} = r\hat{\mathbf{r}}$  and setting it equal to the right hand side (RHS) of Eq. (1.2), one can show that two bodies in a bound system interacting solely via gravity will follow static confocal ellipses whose common focus is their center of mass, or barycenter.

Recalling our assumption that  $M \gg m$ , where here  $M$  is the solar mass and  $m$  is the planetary mass, we can approximate the Solar System's barycenter as the center of the Sun: thus, Kepler's First Law. This procedure also yields  $h^2 = GMa(1 - e^2)$  for orbital semimajor axis  $a$  and eccentricity  $e$ . Thus, integrating  $A = \int_{t_1}^{t_2} \dot{A} dt$  over an orbital period yields Kepler's Third Law.

The general equation of a rotated, off-center ellipse is given as:

$$P_1x^2 + P_2xy + P_3y^2 + P_4x + P_5y = 1 \quad (1.3)$$

for constant parameters  $P_1, P_2, P_3, P_4,$  and  $P_5$ . For a non-rotated ellipse, the  $P_2$  term vanishes; for an ellipse centered at  $(0, 0)$ , the  $P_4$  and  $P_5$  terms vanish. For a non-rotated ellipse centered on  $(0, 0)$ , the  $P_1$  and  $P_3$  terms reduce to their familiar values,  $P_1 = a^{-2}$  and  $P_3 = b^{-2}$  for semimajor axis  $a$  and semiminor axis  $b$ .

Since the orbits are ellipses, we can describe them using Eq. (1.3); since they are static, all five parameters must be constant. This implies the existence of more conserved quantities; for a two-dimensional orbit, only the  $z$  component of  $\mathbf{h}$  is non-zero, so we need four more. Given Newton's Third Law, which states that that forces the two bodies exert on each other are equal and opposite, we can show that their barycenter cannot accelerate; thus, we can always transform to an inertial frame of reference in which it is constant. This provides two more conserved quantities, which specifically account for parameters  $P_4$  and  $P_5$  in Eq. (1.3). We get the fourth by dotting both sides of Eq. (1.2) with  $\mathbf{r}$ , which yields the *energy* per unit mass  $C = \frac{1}{2}v^2 - \frac{GM}{r}$ , where the speed  $v = |\dot{\mathbf{r}}|$ . The last is somewhat more obscure: the

*eccentricity vector*  $\mathbf{e} = \frac{1}{GM}\mathbf{v} \times \mathbf{h} - \hat{\mathbf{r}}$ , which points from apoapse to periapse and whose magnitude  $e$  equals the orbital eccentricity [6].

We typically want a more direct description of an orbit than this. To that end, one can show that  $C = -\frac{GM}{2a}$ ; recalling that  $h^2 = GMa(1 - e^2)$ , we see that energy and angular momentum respectively control the size and shape of the orbit. Furthermore, one can use  $\mathbf{e}$  to calculate the argument of periapse  $\omega$ , which describes the orientation of the orbit relative to some fixed reference point. These three quantities –  $a$ ,  $e$ , and  $\omega$  – are commonly cited parameters called orbital elements, and for a two-dimensional system, they are sufficient to completely describe the orbital path.<sup>1</sup> If we incline the orbit relative to some reference plane (e.g., the plane of the ecliptic for planetary orbits), then we produce two more orbital elements; the inclination angle  $i$  and the longitude of ascending node  $\Omega$ , which describes the relative orientation of the orbital and reference planes. We do not need any additional conserved quantities to find  $i$  and  $\Omega$ ; the  $x$  and  $y$  components of  $\mathbf{h}$  are no longer zero for three-dimensional orbits and are used to calculate these two additional elements.

Although we only need three parameters to describe a two-dimensional *orbit* (and five for a three-dimensional orbit), we need one more to describe *motion*. One can see this by directly integrating Eq. (1.2) to get  $r$ , which produces  $kN$  linearly independent parameters for  $N$  bodies in  $k$  dimensions. Common choices for this last parameter are the true (or mean) anomaly (or longitude), all of which describe the

---

<sup>1</sup>If we locate  $M$  at the origin, the center offset must always have magnitude  $ae$  and direction  $(-\cos\omega, -\sin\omega)$ .

body’s location on its orbit. Although this is mathematically unsatisfying – these choices are not constants – the typical alternative is the time of periapse passage, which is constant but much less practically useful, and this thesis will not reference it again.

This completes the two-body problem. Given a position and velocity vector for each body at any point in time, we can determine their positions and velocities at all times. What if we add more bodies?

## 1.2 The N-Body Problem

Although it is beyond the scope of this thesis to prove so here, the  $N$ -body problem – that is, determining the motions of  $N$  bodies analytically for all time – is sadly unsolvable for  $N > 2$ ; there are simply not enough additional constants of motion. Although special cases of the three-body problem do have analytic solutions, if we want to predict the general motions of more than two bodies, we must resort to numerical integration. The underlying mathematics have now been studied for over two centuries [7]; interested readers may consult [8] or [9] for more details.

Various integration schemes exist, but the only one used in this thesis is the (second-order) *symplectic* integrator, which splits Eq. (1.2) into two equations, one of which is integrated for velocity, and the other for position:

$$\dot{\mathbf{v}} = \frac{GM}{r^2} \hat{\mathbf{r}} \quad \dot{\mathbf{r}} = \mathbf{v}. \quad (1.4)$$

A single step forward in time (called the “timestep”) is typically ordered as “kick-

drift-kick” (update velocity, then position, then velocity again) or “drift-kick-drift” (vice versa). We give one example of a “kick-drift-kick” scheme in which position and velocity are updated from step  $n$  to step  $n + 1$  here:

$$\mathbf{v}_{n+\frac{1}{2}} = \mathbf{v}_n + \left(\frac{\Delta t}{2}\right) \dot{\mathbf{v}}(\mathbf{r}_n) \quad (1.5)$$

$$\mathbf{r}_{n+1} = \mathbf{r}_n + \Delta t \mathbf{v}_{n+\frac{1}{2}} \quad (1.6)$$

$$\mathbf{v}_{n+1} = \mathbf{v}_{n+\frac{1}{2}} + \left(\frac{\Delta t}{2}\right) \dot{\mathbf{v}}(\mathbf{r}_{n+1}) \quad (1.7)$$

where  $\Delta t$  is the *timestep*. Since the velocity and position are updated “out of sync” with each other, this is often called the leapfrog method – see Fig. 1.2.

Note that Eqs. (1.5), (1.6), and (1.7) are time reversible. To go backwards in time, one uses the same steps, replacing  $\Delta t$  with  $-\Delta t$ , and ends at precisely the same position and velocity whence they started. As a result, this method (and in fact any symplectic integrator, by definition) conserves orbit-averaged energy and angular momentum – there are no secular errors in either quantity. This is only possible because the acceleration,  $\ddot{\mathbf{r}}$ , is a function solely of position and not velocity. For this reason, symplectic integrators can remain stable far longer than non-symplectic alternatives such as standard Runge-Kutta methods.

To show that our leapfrog algorithm truly is accurate to second order <sup>2</sup> in  $\Delta t$ , we substitute Eq. (1.5) into Eq. (1.6) and write  $\mathbf{v}$  as  $\dot{\mathbf{r}}$ , which produces the

---

<sup>2</sup>One might find it strange that any errors in  $\mathbf{r}$  exist at all given that there are no secular errors in energy or angular momentum. The reason is that the integrator is not actually conserving the true energy, but rather a slightly perturbed one.

following expression for the estimated  $\mathbf{r}_{n+1}$ :

$$\mathbf{r}_{n+1, \text{ est.}} = \mathbf{r}_n + \Delta t \dot{\mathbf{r}}_n + \left( \frac{(\Delta t)^2}{2} \right) \ddot{\mathbf{r}}_n. \quad (1.8)$$

The true expression for  $\mathbf{r}_{n+1}$  can be expressed as a Taylor expansion<sup>3</sup>:

$$\mathbf{r}_{n+1, \text{ true}} = \mathbf{r}_n + \Delta t \dot{\mathbf{r}}_n + \left( \frac{(\Delta t)^2}{2} \right) \ddot{\mathbf{r}}_n + \mathcal{O}((\Delta t)^3). \quad (1.9)$$

The error on  $\mathbf{r}_{n+1}$  is the difference between Eqs. (1.8) and (1.9), which in turn is  $\mathcal{O}((\Delta t)^3)$ . Higher-order integrators are possible via, e.g. [10], [11], [12], but we do not consider them here.

### 1.3 Perturbations

Thus far, the only force we have considered is gravity, and we have tacitly assumed that all bodies are zero-dimensional point particles. Despite being far more complex in general, reality does offer the lone simplification that many systems of interest (and all systems of interest to this thesis) are dominated by a single mass, such as the Sun and planets or Jupiter and its moons. This allows us to recast the  $N$ -body problem as  $N - 1$  two-body problems subject to various *perturbations*.<sup>4</sup> While an  $N$ -body integrator of the type described above can easily account for perturbations that conserve energy and angular momentum (e.g., gravity from other planets to Earth's orbit around the Sun), others (e.g. gas drag or tidal forces) are

---

<sup>3</sup>This is an exact expression for constant acceleration, but in reality the acceleration itself is changing.

<sup>4</sup>Kepler's Laws implicitly do this recasting while ignoring all perturbations.

more challenging to include, and we require other means of approximating them.

Recall that in the two-body problem, both bodies move on static ellipses. In fact, only pure gravity (or, interestingly, a simple harmonic oscillator) can produce such orbits. If pure gravity is perturbed, the ellipses will no longer remain static. Converting  $C$ ,  $\mathbf{h}$ , and  $\mathbf{e}$  to the orbital elements will not produce constant  $a$ ,  $e$ , etc., but rather the so-called “osculating” elements – the elements of the orbit the bodies would take if the perturbation vanished upon their calculation. The osculating elements will vary in time, and given the radial, tangential, and normal components of the force, we can write down what this variation will be via [13].

This thesis will largely be concerned with near-equatorial orbits, so we will ignore variations in  $i$  and  $\Omega$ , while variations in  $\omega$  will be due to conservative forces that our numerical integrator, HNBody, can accommodate naturally [14]. Thus, we will limit our interest to  $\dot{a}$  and  $\dot{e}$ :

$$\frac{\dot{a}}{a} = 2\sqrt{\frac{a}{\mu(1-e^2)}} [Re \sin \nu + T(1 + e \cos \nu)] \quad (1.10)$$

$$\frac{\dot{e}}{e} = \sqrt{a\mu^{-1}(e^{-2} - 1)} [R \sin \nu + T(\cos \nu + \cos E)], \quad (1.11)$$

where  $\mu = G(M + m)$  for central mass  $M$  and perturbed body mass  $m$ ,  $E$  is eccentric anomaly, defined via  $\cos E = \frac{x}{a}$ , and  $R$  and  $T$  are the radial and tangential components of the perturbing force, respectively. We see immediately that only forces in the orbital plane can affect  $a$  and  $e$ . Furthermore, for constant  $R$  and  $T$ , there can be no secular changes to  $e$ ; this is not the case for  $a$ .

When we include perturbing forces, we typically care less about their precise forms, which may be disputed in any case, and more about the timescales on which they act and the secular effects they have on  $a$  and  $e$ . We can then include extra forces in our numerical integrations that have these desired effects despite not being “correct” using Eqs. (1.10) and (1.11). For example, if we wish to simulate secular  $a$  changes but no secular  $e$  changes, we can include an extra force pointed in the tangential direction that is constant over an orbit period. We can then multiply it by whatever constant is required to produce the desired timescale. This strategy allows us fine control over the perturbations we simulate; we can pick and choose the effects we wish to enhance or ignore.

## 1.4 Mean Motion Resonances

A system of multiple bodies orbiting one high-mass object offers the possibility of *mean motion resonances*, which occur when the mean motions of two or more bodies are a ratio of low integers.<sup>5</sup> One example in nature can be found between Neptune and Pluto, which are in the 3:2 (or 2:3) mean motion resonance: Pluto completes almost exactly two orbits for every three of Neptune. Even though their orbits cross, this resonance ensures that Pluto and Neptune are always more than 20 AU [5] from each other, preventing Neptune from scattering its tiny neighbor.

We shall presently examine how resonances perturb the orbits of the bodies that inhabit them. First, however, we note that the mathematics behind resonant interactions is far more complex than our simplified treatment here. Our discus-

---

<sup>5</sup>Many kinds of resonances exist, but this thesis will focus on just this one.

sion will highlight and heuristically explain some results relevant to this thesis, but readers interested in a proper treatment may consult [5], [15], [16], [17], or [18].

Consider a system of two coplanar resonant planets orbiting a star in which the inner planet's orbit is eccentric while the outer planet's orbit is circular. Considering only perturbations from the outer planet on the inner, [5] show that in general, orbit-averaged tangential forces will nudge the latter's orbit until conjunctions occur at its periapse. At this point, orbit-averaged tangential forces vanish, making this configuration a stable equilibrium; there is also an unstable equilibrium in which conjunctions occur at the inner planet's apoapse.

This stable equilibrium, however, is a moving target. Each time the inner planet approaches conjunction, the outer planet pulls it outward, slowing its motion and rotating its periapse. Thus, orbit-averaged tangential forces always exist and period ratios are never truly exact; one must always correct for this periapse rotation.<sup>6</sup> Ultimately, the inner planet will librate around the equilibrium. In the case where the inner planet's orbit is circular, the outer planet's orbit is eccentric, and we consider only perturbations from the inner planet on the outer, the stable equilibrium is now at the outer planet's apoapse, and the unstable one is at its periapse.

Such behavior has two important consequences for this thesis. First, bodies in resonance will *stay* in resonance absent a very powerful perturbation that knocks them sufficiently far from their equilibrium. In future chapters, we will subject res-

---

<sup>6</sup>In the case of mutually inclined orbits, the two orbital planes may also rotate relative to each other, necessitating a further correction.

onant bodies to extra forces that change their semimajor axes, but because of this phenomenon, their orbit-averaged period ratios will not change. Second, the tangential forces near periapse on the librating body must change its orbital eccentricity. To see this, recall Eq. (1.11); at periapse,  $\cos \nu = 1$  and  $\cos E = 1$  by convention, so if  $T$  is non-zero, there must likewise be a non-zero  $\dot{e}$ .

## 1.5 Thesis Outline

This thesis will be structured as follows. Chapter 2 will study the origins of the Kepler 36 planetary system, which features two planets of very different densities whose orbits are radially close to each other, contrary to the expectations of standard solar system formation theory. Chapter 3 will derive a set of “geometric” orbital elements that vary far less than the standard osculating elements under the perturbation that arises from an oblate central body. Chapter 4 will examine a new formation model for Titan, Saturn’s largest moon, in which several resonating satellites (similar to the modern-day Galilean moons at Jupiter) undergo dynamical instability and merge. Chapter 5 will present a new theory for how narrow eccentric rings can remain confined to radial widths of approximately 1-10 km even in the absence of nearby “shepherd” satellites. Finally, Chapter 6 will summarize the results of the thesis.

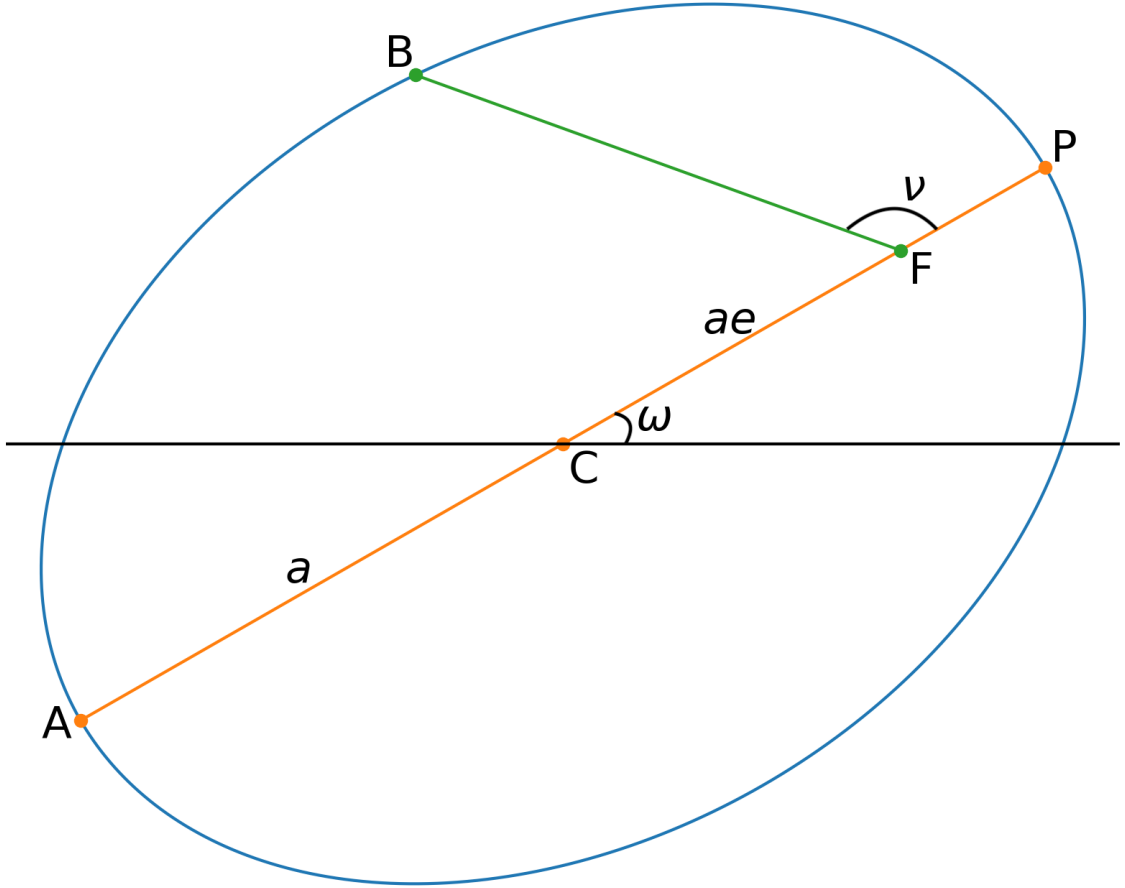


Figure 1.1: Depiction of an orbit (blue ellipse) relative to some reference line (black line). Points A and P are the apoapse and periapse, respectively; the orange line connecting them is the line of apses and has length  $AP = 2a$  for semimajor axis  $a$ . Point C is the center, where  $AC = CP = a$ . Point F is one of the two foci (the other is not labeled); the lines FP and FA are the periapse and apoapse distances, respectively, where  $FP = a(1 - e)$  and  $FA = a(1 + e)$  for eccentricity  $e$ . The length CF is the distance from center to focus such that  $CF = ae$ . The angle between the orange line of apses and the black reference line is the argument of periapse  $\omega$ . Finally, point B is the location of the body, and the angle from periapse to body (i.e., between the orange line  $\overline{FP}$  and the green line  $\overline{FB}$ ) is the true anomaly  $\nu$ , where  $FB = \frac{a(1-e^2)}{1+e \cos \nu}$ . For a Kepler orbit,  $FB = r$ . This example uses the elements  $e = 0.7$ ,  $\omega = 30^\circ$ , and  $\nu = 130^\circ$ .

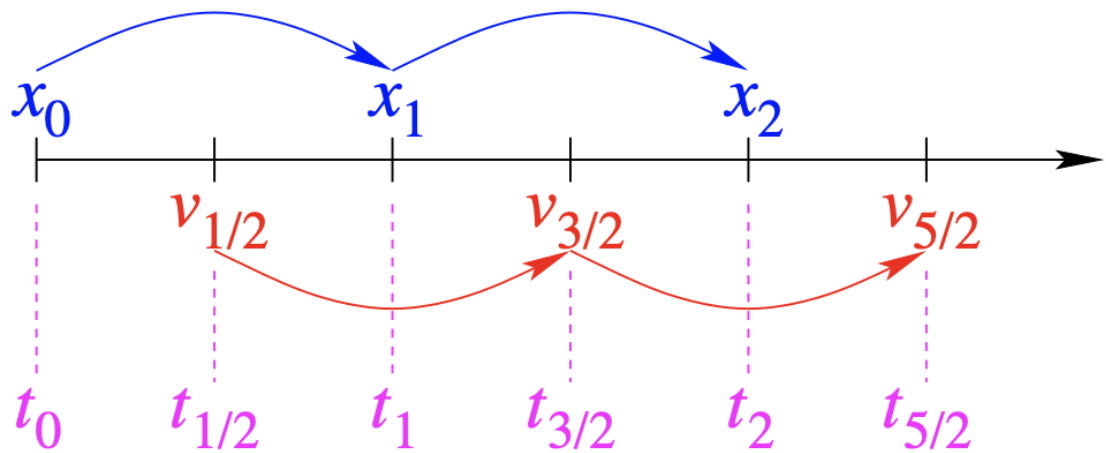


Figure 1.2: Depiction of a leapfrog integration scheme. Position  $x$  is updated at integer subscripts of time  $t$ , whereas velocity  $v$  is updated at half-integer subscripts. Source: <https://www.astro.umd.edu/~ricotti/NEWWEB/teaching/ASTR415/class15.pdf>

## Chapter 2: Exploring the Origin and Evolution of the Kepler 36 System

In this Chapter, we examine two unusual exoplanets; despite a huge difference in densities, their orbits are extremely close together, and they both lie very close to their host star. Such a configuration is wholly alien to residents of the Solar System, which has a very different architecture. How did these exoplanets get to their current positions with their current densities? We use perturbation and resonance theory to investigate this question in a self-consistent, natural way. This chapter has been submitted for publication to the Monthly Notices of the Royal Astronomical Society.

### 2.1 Introduction

#### 2.1.1 Previous Work

Among the most dynamically interesting extra-solar planets (exoplanets) are those in so-called ‘tightly packed’ systems, which feature multiple bodies all orbiting close both to their host star and to each other. One such system is Kepler 36 (Table 2.1).

These planets have two notable features. First, they are located very near one

Name	Semimajor Axis (AU)	Density (g cm <sup>-3</sup> )	Mass (M <sub>⊕</sub> )
Kepler 36b	0.1153 ± 0.0015	7.46 <sup>+0.74</sup> <sub>-0.59</sub>	4.45 <sup>+0.33</sup> <sub>-0.27</sub>
Kepler 36c	0.1283 ± 0.0016	0.89 <sup>+0.07</sup> <sub>-0.05</sub>	8.08 <sup>+0.60</sup> <sub>-0.46</sub>

Table 2.1: Key properties of Kepler 36b and c. Data taken from [19].

another and are also within 1 per cent of the 7:6 orbital mean motion resonance (MMR), i.e., their periods are very close to a 7:6 ratio. Second, their densities differ by nearly a factor of 10 despite their small radial separation. The placement of a gaseous sub-Neptune so close to a rocky super-Earth defies standard formation models that predict planetary systems to be segregated by both mass and density, as the Solar System is. This chapter proposes a new evolutionary path in which these planets migrate past other more common resonances and terminate at the 7:6 MMR in their current locations.

Several works instead posit that high-energy protostellar radiation might significantly alter these planets’ atmospheres [1, 20, 21, 22]. They argue that the elevated X-ray and XUV (extreme ultraviolet) flux of a young star could strip the atmospheres of high-density, close-in planets. In their now-standard model, [1] initialize both planets at their current orbits with identical H/He mass fractions ( $\sim 22$  per cent) and radii ( $\sim 10 R_{\oplus}$ ), but different masses ( $m_b \sim 5.7 M_{\oplus}$ ,  $m_c \sim 9.4 M_{\oplus}$ ) and bulk densities ( $\rho_b \sim 0.031 \text{ g cm}^{-3}$ ,  $\rho_c \sim 0.052 \text{ g cm}^{-3}$ ). Kepler 36b loses nearly all of its atmosphere to high-energy stellar radiation within  $10^8$  yr, while Kepler 36c retains roughly half of its own envelope. The authors attribute this difference to Kepler 36c’s greater assumed amount of rocky material (7.34 M<sub>⊕</sub> compared to 4.45 M<sub>⊕</sub> for Kepler 36b) and predict that Kepler 36b should lose its envelope approximately three times faster than Kepler 36c despite receiving only about 24 per cent more

radiation. Since they receive similar amounts of radiation, the planets’ atmosphere retention rates are largely determined by their core masses; by fine-tuning them, the authors reproduce the observed masses and densities of the Kepler 36 planets. [21] and [22] study similar formation scenarios without fundamentally modifying the idea that stellar XUV radiation is responsible for the density disparity between these two planets.

More generally, [1] predict that the incidence of sub-Neptune planets ( $1.8 < \text{radius} < 4.0 R_{\oplus}$ ), should decline rapidly for periods  $\lesssim 10$  days, while the incidence of smaller planets should simultaneously rise. In Fig. 2.1, we compare these predictions to the modern planetary database found at [exoplanet.eu](http://exoplanet.eu). Current observations show that while the frequency of sub-Neptunes does decline for shorter periods, this decline begins at  $\sim 4$  days, much closer than the 10-day prediction of [1]. A steady increase in the number of small planets as the stellar distance decreases from 10 d to 1 d periods is also apparent in Fig. 2.1. The correlation between these two trends is not strong.

[23] study a scenario in which the density disparity between the planets is due entirely to the composition of their feeding zones. In their picture, Kepler 36b is rocky because it is formed from the mergers of several rocky bodies totaling  $3 M_{\oplus}$ ; likewise for Kepler 36c and two icy bodies totaling  $7.3 M_{\oplus}$ . These are reasonably close to the planets’ current observed masses. Stellar radiation is ignored. Once Kepler 36c forms, it migrates inward toward Kepler 36b, skipping past several resonances but stopping in the 7:6 MMR with Kepler 36b, in which the two planets reside for the remainder of the simulation. While this idea for the density disparity

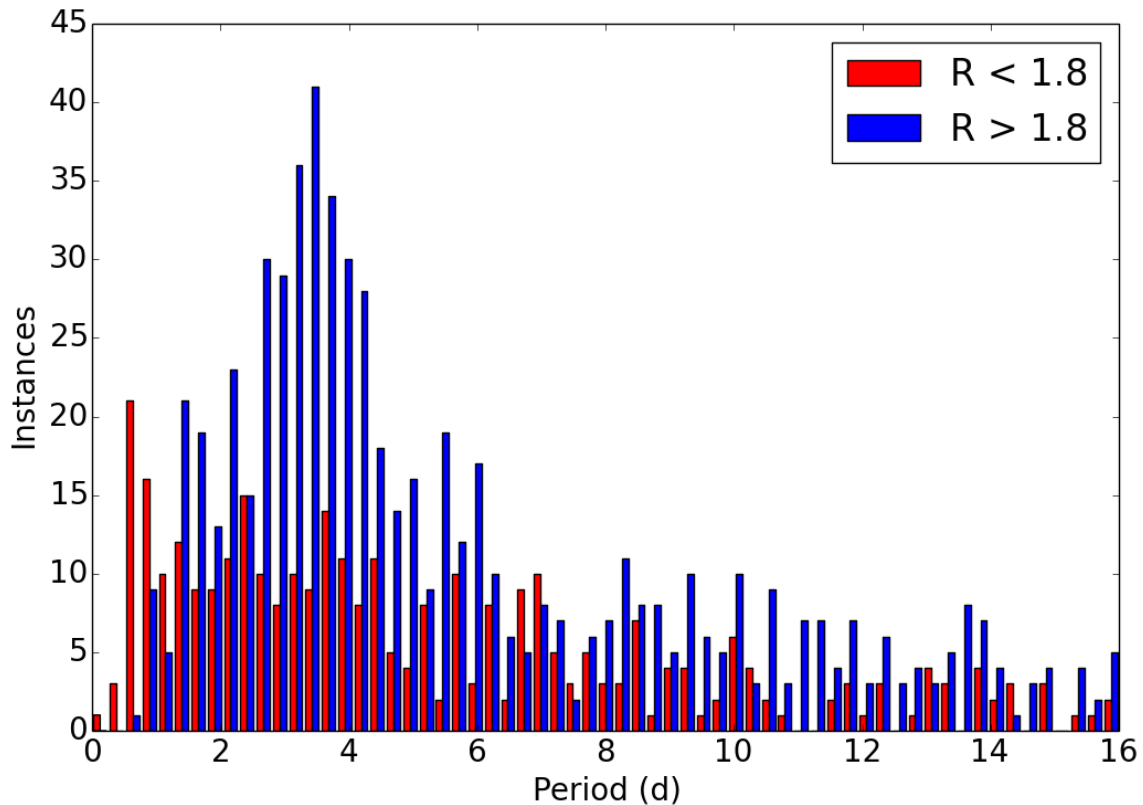


Figure 2.1: Instances of confirmed planets with period  $P < 16$  days, radius  $R < 4R_{\oplus}$ , and period and radius errors less than one per cent, using 64 bins. The red bars correspond to planets with  $R < 1.8R_{\oplus}$ , which [1] designate as super-Earths. The blue bars conversely correspond to those planets they designate as sub-Neptunes. Sub-Neptune frequency peaks at  $P \sim 4$  days. Data taken from the exoplanet.eu catalog and current as of 18 May 2020.

is compelling, we find that convergent migration alone is unlikely to account for the 7:6 MMR. Our simulations (Sec. 2.2) indicate that collisions are necessary to eject bodies from resonance, and in their absence, it is difficult to force planets so close together. Furthermore, [24] find that stochastically forced planets that capture into the 7:6 resonance from disk forces alone are unlikely to stay there permanently.

[24] investigate a different model, in which they place numerous Mars-mass planetary embryos beyond the two planetary orbits; the embryos migrate inwards until they collide with one of the planets, typically the outermost body. After fine tuning the number of embryos, the migration rate, and other parameters, [24] find that these collisions can force the planets past several resonances in which they would otherwise remain trapped. In their scenarios, impacts with embryos that stripped one planet (assumed to have already differentiated) of its less dense outer material produced the density contrast. [24] suggested two possible formation pathways. In the first, the outer planet (which received approximately twice as many impacts as the inner) lost its mantle, and subsequent collisions kicked it past the inner planet, i.e., the planets exchanged positions. In the second, the inner planet was stripped instead, and no such exchange occurred. Each scenario faces significant difficulties reproducing the density contrast; either the planets had to cross orbits without going unstable, or the planet receiving fewer impacts had to lose its mantle while the planet receiving more could not.

Although this model has many appealing aspects, we do not expect Mars-mass embryos to necessarily migrate inward faster than planets with an order of magnitude more mass. [24] assume that the planets would open gaps in the gas disk

(Type II migration) whereas the embryos would not (Type I migration), and that this difference would yield a faster migration rate for the embryos. However, the precise mass range at which planets transition from Type I to Type II migration, and the nature of migration within this range, has enjoyed considerable debate for decades with few firm conclusions beyond general guidelines (e.g. [25], [26], [27]). These analyses are typically subject to various simplifying assumptions about the gas disk itself [28]. In particular, [27] estimate that Type II migration should not begin until planetary mass  $\gtrsim 30M_{\oplus}$  for a typical disk, which would place both Kepler 36 planets firmly in the Type I range. Furthermore, [28] predict that the Type I migration rate should be proportional to mass (their equation 70), implying that planets should migrate faster than embryos. We likewise adopt this requirement.

### 2.1.2 Our Model

In this chapter, we present a formation model for the Kepler 36 planetary system that incorporates many elements of that proposed by [24] but is nevertheless distinct in several ways. In our model, Kepler 36b forms within the ice line with less mass than that which [19] measured, and Kepler 36c forms beyond the ice line with roughly its current mass, perhaps via a similar process to that outlined by [23]. The two planets migrate inward through a protoplanetary disk; Kepler 36c migrates faster, rapidly overtaking its less massive neighbor and capturing it into the 2:1 MMR. After this capture, the two planets migrate in together through a field of embryos and small protoplanets. The inner planet is pushed inward into undepleted

parts of the disk and interacts with these bodies, colliding and merging with many of them. Most small planetesimals are gone at this point, having merged to form the larger planetary embryos. Those that remain play no role in the dynamical evolution of the two planets. In this model, most of the embryo/protoplanet disk accretes onto the inner planet as it migrates inward. Its mass roughly equals the mass of the accreted material, typically ranging from a few Earth masses to several (see Fig. 2.8 in Section 2.3.4).

The likelihood of the smaller bodies colliding with the inner planet, rather than scattering, depends on the inner planet’s escape speed  $v_{\text{esc}}$  and the smaller body’s orbital speed  $v_{\text{orb}}$ ; they preferentially collide for  $v_{\text{esc}} < v_{\text{orb}}$  and preferentially scatter for  $v_{\text{orb}} < v_{\text{esc}}$  [29]. Planet b has a radius of  $1.486 \pm 0.035 R_{\oplus}$  [19]; its mass is given in Table (2.1). These values yield  $v_{\text{esc}} \approx 19.4 \text{ km s}^{-1}$ . This allows us to estimate a critical semimajor axis  $a_{\text{crit}}$  below which an object would preferentially collide with planet b by equating  $v_{\text{esc}}$  with average orbital velocity  $\langle v_{\text{orb}} \rangle \approx \sqrt{\frac{GM}{a_{\text{crit}}}} (1 - \frac{1}{4}e^2)$ , where  $G$  is the gravitational constant,  $M$  is the mass of Kepler 36, and  $a$  and  $e$  are the semimajor axis and eccentricity of the smaller body, respectively. Taking  $e = 0.2$ , this yields  $a_{\text{crit}} \approx 2.57 \text{ AU}$ , somewhat lower than typical ice line estimates for a Sun-like star (see, e.g., [30], [31], [32]). Since we model the inner planet as forming within the ice line and migrating inward, we therefore expect that most close approaches with it should result in collisions, not scattering. As a result, the innermost planet can effectively shield the outermost from the material, as a cowcatcher leading a train shields it from debris on the tracks.

Importantly, some of the collisions are of sufficient strength to eject Kepler 36b

from its resonance entirely. Depending on the direction of impact, either the planet is kicked inward and quickly recaptured by the inwardly moving 2:1 resonance, or it is flung outward and is soon captured by a closer resonance, e.g., the 3:2. These outcomes each occur with a  $\sim 50$  per cent possibility because the planet is about as likely to collide with a slower body (thus losing energy) as a faster one (thus gaining energy). We envision that this process repeats until the planets are left near the 7:6 resonance. Additionally, the accretion of denser material not only raises the bulk density of planet b but also increases its mass to the current measured value; the greater self-gravity also acts to further raise the planet’s density by compression. Earth has a density of  $5.5 \text{ g cm}^{-3}$ , a value enhanced by compression of its iron core, and  $4.5 M_{\oplus}$  of Earth-like material could easily have an average density of  $7.5 \text{ g cm}^{-3}$ .

## 2.2 Simulations

### 2.2.1 Damping Forces

To test our model, we used the symplectic option within the N-body integrator HNBody [14] to simulate two planets orbiting Kepler 36 in a protoplanetary disk. In addition to the normal gravitational forces between the three bodies in the integration, we also included two additional forces via HNDrag, an expansion suite to HNBody, that approximated the semimajor axis drag ( $\dot{a}$ ) and eccentricity damping ( $\dot{e}$ ) effects of the disk. We modeled  $\dot{a}$  with the user-defined force per unit mass  $\mathbf{f}_a = -k_a \mathbf{v}$ , for planetary velocity  $\mathbf{v}$  and strength  $k_a = -\frac{\dot{a}}{2a}$ . This force has the useful property that  $\dot{e} = 0$  when averaged over an orbit. We define the  $e$  damping

force by  $\mathbf{f}_e = -k_e v_r \hat{\mathbf{s}}$ , where  $v_r$  is the radial speed,  $\hat{\mathbf{s}}$  is a unit vector perpendicular to the overall velocity (minimizing changes to the body’s energy), and  $k_e = -\frac{\dot{e}}{2e}$  is analogous to  $k_a$ . The velocities in these forces are expressed in units of initial circular velocity of whichever body to which they are applied, approximately equal to  $22.3 \text{ km s}^{-1}$  for planet b and  $14.1 \text{ km s}^{-1}$  for planet c. With this normalization,  $k_a^{-1}$  and  $k_e^{-1}$  are the approximate timescales of  $\dot{a}$  and  $\dot{e}$ , respectively.

These forces are clearly simplifications of the true forces these planets would experience in a protoplanetary disk. [24] and [33], who investigated the strengths of different orbital resonances in the Solar nebula, suggest two alternatives. [33] considers small planetesimals in a turbulent disk that feel aerodynamic gas drag [34]. By contrast, [24] use a Stokes drag-like force:  $\mathbf{f}_d = -\frac{\mathbf{v}}{2\tau_a} - \frac{\mathbf{v}-\mathbf{v}_c}{\tau_e}$ , where  $\mathbf{v}$  and  $\mathbf{v}_c$  are the planet’s velocity and circular velocity at its current radius, respectively, and  $\tau_a$  and  $\tau_e$  are the migration and eccentricity damping time-scales, respectively.<sup>1</sup> [33] notes that such a force would be appropriate for a laminar (smooth) disk. [27] also assume a viscous, laminar disk for most of their discussion of migration rates.

## 2.2.2 Collisions

We also included collisions, approximated as impulses (changes in velocity  $\delta\mathbf{v}$ ), in our simulations. This technique offered several advantages over the more traditional approach of directly integrating the impactors along with Kepler 36 and its two planets.

First, we could guarantee that a precise number of impacts would occur,

---

<sup>1</sup>Our drag model differs from this only on orbital timescales.

whereas integrating the impactors would have allowed the possibility of no impacts or too many. Clearly, collisions *could* occur in some cases; we simply integrated under the assumption that they did. Second, simulating collisions as impulses gave us perfect control over when they occurred, in what direction, and with what strength, enabling us to easily study and understand the effects of a single collision in great detail. Finally, simulating collisions as impulses dramatically reduced integration time and allowed us to simulate arbitrary numbers of collisions at little extra cost. Since integration time is  $\mathcal{O}(n^2)$  for  $n$  bodies, directly integrating, e.g., 10 impactors in addition to the star and two planets would have increased our computation time by a factor of nearly 20.

We spaced our impacts at intervals of  $5 \times 10^5$  yr; the number of impulses  $N$  ranged between 3 and 15 per simulation. For each of our thirteen choices of  $N$ , we randomly generated five sets of  $N$  values for  $\frac{\delta \mathbf{v}}{v}$  (for 65 sets total); these values were randomly distributed between  $-0.05$  and  $0.05$  to ensure that most impulses would be able to kick planets out of resonance (see Section 2.3.2). We selected our range for  $N$  by estimating the minimum and maximum number of collisions needed to move the planets from the 2:1 MMR to the 7:6 without going beyond it. We thought it highly unlikely that only one or two collisions could knock the bodies across so many resonances. Even if this were possible, and even assuming they kicked the planets towards each other, such powerful collisions could potentially deviate from our perfect-accretion impulse model quite significantly, e.g., could shatter the impacted body. For our maximum case, we considered the “unlucky” scenario in which only  $\frac{1}{3}$  of the impulses pushed the planets together, and each one moved the

planets into the next-closest first-order MMR, for fifteen impulses total. Of course, we could have raised this maximum by allowing still fewer impulses to push the planets together, but we estimated each of our impactors to be several to tens of lunar masses (Section 2.3.2). We wished to avoid adding too much rocky mass to a system that already had several times that of the Solar System’s terrestrial planets.

Impulses with positive  $\delta\mathbf{v}$  were parallel to the impacted planet’s velocity, and those with negative  $\delta\mathbf{v}$  were antiparallel. For each set of disk parameters (Table 2.2), we ran five simulations, each using a different set of impulses. All simulations with the same  $N$  used the same five impulse strength sets. The timing scheme was not random; we chose a uniform interval that was much longer than the  $e$  damping time-scales we tested. Our tests of different uniform intervals, all of which were again much longer than the  $e$  damping time-scale, found only minor differences. In any case, it is not obvious what a more “natural” timing distribution would have looked like. We searched for simulations in which the two planets ended in the 7:6 MMR and separately evaluated how physically likely those scenarios were.

Due to our impulse approximation for collisions, we needed to estimate the impactor masses. Thus, we assigned an orbit with eccentricity  $e_i$  to each impactor and assumed perfect angular momentum conservation, i.e., no loss of fragments:

$$m_i\mathbf{r}_i \times \mathbf{v}_i + m_p\mathbf{r}_p \times \mathbf{v}_p = (m_i + m_p)\mathbf{r}_f \times \mathbf{v}_f, \quad (2.1)$$

where  $\mathbf{r}$  and  $\mathbf{v}$  respectively denote position and velocity,  $m$  denotes mass, and the subscripts i, p, and f respectively denote impactor, planet, and final. At time of

impact,  $\mathbf{r}_i = \mathbf{r}_p$  and  $\mathbf{v}_i \approx (v_p + e_i v_{p,\text{circ}}) \hat{\mathbf{v}}_p$  for planetary circular speed  $v_{p,\text{circ}}$ . With these substitutions, we could solve for  $m_i$  given two subsequent simulation outputs, where the state vectors from the first output provided  $\mathbf{r}_p$  and  $\mathbf{v}_p$ , and those from the second provided  $\mathbf{r}_f$  and  $\mathbf{v}_f$ .

This approach led to some small errors. While in principle, our mass calculation algorithm depended on our output frequency, in practice, we output coordinates frequently enough that each planet’s angular momentum changed very little from one output step to the next; changing this frequency introduced differences of order  $\lesssim 1\%$  to the calculated mass, a value far below the uncertainty in the assumed impactor eccentricity. Most significantly, we did not update Kepler 36b’s mass within the simulation after each impulse. Since the planet masses are comparable and the inner planet often increased in mass by a third or more, not updating Kepler 36b’s mass also introduced some error into our integrations; for example, more massive bodies require more powerful kicks to eject from resonance.

### 2.2.3 Initial Conditions

We performed over 7,000 simulations using the University of Maryland supercomputer `deepthought2`, in which we varied five parameters: the inner planet’s migration rate, inner and outer planet eccentricity damping strengths, number of impulses, and set of impulse strengths. The values that we used for the first four of these parameters as well as planetary masses and initial orbital elements are given in Table 2.2. All integrations ran for  $10^7$  yr except for cases in which the inner body

got within 0.1 AU of the star, at which point our timestep of 0.001 yr was too long to reliably resolve the orbital motion and the simulation came to a pre-programmed halt. Under these conditions, most simulations ended with the two planets near Kepler 36b and c’s observed semimajor axes – each sits just over 0.1 AU from Kepler 36 (Table 2.1). In cases featuring powerful collisions that kicked Kepler 36 b out past c, however, the planets could end up far apart from each other, as the new, faster-migrating inner planet moved away from the new outer planet until it got within 0.1 AU of the star and the simulation ended.

We printed the bodies’ state vectors once per thousand years and prioritized searching a wide parameter space – and finding integrations in which the planets evolved to the current observed Kepler 36 planetary configuration – over confining ourselves to values consistent with a ‘standard’ protoplanetary disk. We do not know, for example, whether the planets opened a gap in the disk, whether the disk was vertically isothermal, the strength of the disk’s viscosity or self-gravity, etc. Furthermore, given that the Kepler 36 system is unusual, the disk in which it evolved may have likewise been unusual. In any case, the specific migration rates of each planet are less important than the relative migration rate of the outer body to the inner one because the relative rate determines how quickly Kepler 36c can ‘catch up’ to Kepler 36b, which in turn drives the resonance dynamics.

Parameter	Kepler 36b	Kepler 36c
$m$ ( $M_{\text{star}}$ )	$10^{-5}$	$2.42659 \times 10^{-5}$
$a$ (AU)	2	5
$e$	0.01	0.01
$i$ ( $^{\circ}$ )	0.002	0.007
$\Omega, \varpi, \lambda$ ( $^{\circ}$ )	0	0
$k_a$ ( $\times 10^{-7}$ yr $^{-1}$ )	0.5, 1, 2	4
$\frac{k_e}{k_a}$	1, 3, 10, 30, 100, 300	1, 3, 10, 30, 100, 300
# Collisions	3, 4, ..., 15	0

Table 2.2: All parameter values used for the two planets in our simulations: planetary mass ( $m$ ), semimajor axis ( $a$ ), eccentricity ( $e$ ), inclination ( $i$ ), longitude of ascending node ( $\Omega$ ), longitude of peripase ( $\varpi$ ), and true longitude ( $\lambda$ ). Quantities separated by commas indicate the different values we used for that parameter. The initial mass of the outer body ( $8.08 M_{\oplus}$ ) corresponds to its current observed mass (hence the large number of significant figures), whereas we have chosen the initial mass of the inner body ( $3.30 M_{\oplus}$ ) to be considerably less than its observed value. The very small inclinations on each body were imposed to allow inclination resonances, but as they are very weak, our integrations remained close to two-dimensional.

## 2.3 RESULTS

### 2.3.1 Sample Simulation

In general, our individual simulations display diverse resonance and impact phenomena, as we illustrate in a custom sample simulation (Fig. 2.2). We include migratory and eccentricity damping forces to mimic the effects of nebular gas and arrange for four impacts to occur on the inner planet at intervals of  $5 \times 10^5$  yr. For simplicity of illustration, only the outer planet feels a migratory force. The inner planet’s eccentricity damping force is 3,000 times stronger than that of the outer planet. These choices allow us to easily see how the planets’ semimajor axes and eccentricities respond to resonance capture and departure. As in the rest of our simulations, we follow the planets’ evolution for  $10^7$  yr, although we only show the

first  $3 \times 10^6$  yr in Fig. 2.2.

At  $\sim 1.25 \times 10^6$  yr, the planets enter the 2:1 MMR. In the top panel, this is immediately evident from the constant mean-motion ratio. Resonance capture is likewise responsible for the changed migration rates in the next two panels; as the inner planet starts moving inward, the outer planet slows somewhat. Finally, the establishment of nonzero eccentricity equilibria in the bottom two panels also tracks resonance capture. These equilibria are due to two competing forces: the resonance pushes eccentricity up, while our damping force pushes it down. At  $1.5 \times 10^6$  yr, the inner planet collides with another embryo and is kicked radially inward, out of the 2:1 MMR; Kepler 36b’s migration ceases and the  $e_1$  equilibrium is destroyed.

Due to its migration, the outer body eventually recaptures the inner body into the 2:1 MMR, and they move in as a unit until  $2 \times 10^6$  yr, whereupon the inner body is hit with yet another embryo. This time, it is knocked outward, closing the radial distance between the planets. As before, the inner body is ejected from the 2:1 MMR, but at  $\sim 2.4 \times 10^6$  yr, the outer body captures the inner into the 3:2 MMR, where the planets remain for the remainder of the integration. The two resonances can be distinguished from one another not only through the different mean-motion ratios in the top panel but also through the different eccentricity equilibrium values in the bottom two.

Notice the responses of the two planets’ eccentricities to the 2:1 MMR. Upon initial entrance at  $\sim 1.25 \times 10^6$  yr, the resonance forces the inner body’s eccentricity to a nonzero value while that of the outer body freely decays. After  $1.5 \times 10^6$  yr, however, both bodies’ eccentricities are forced up. Two distinct resonances are

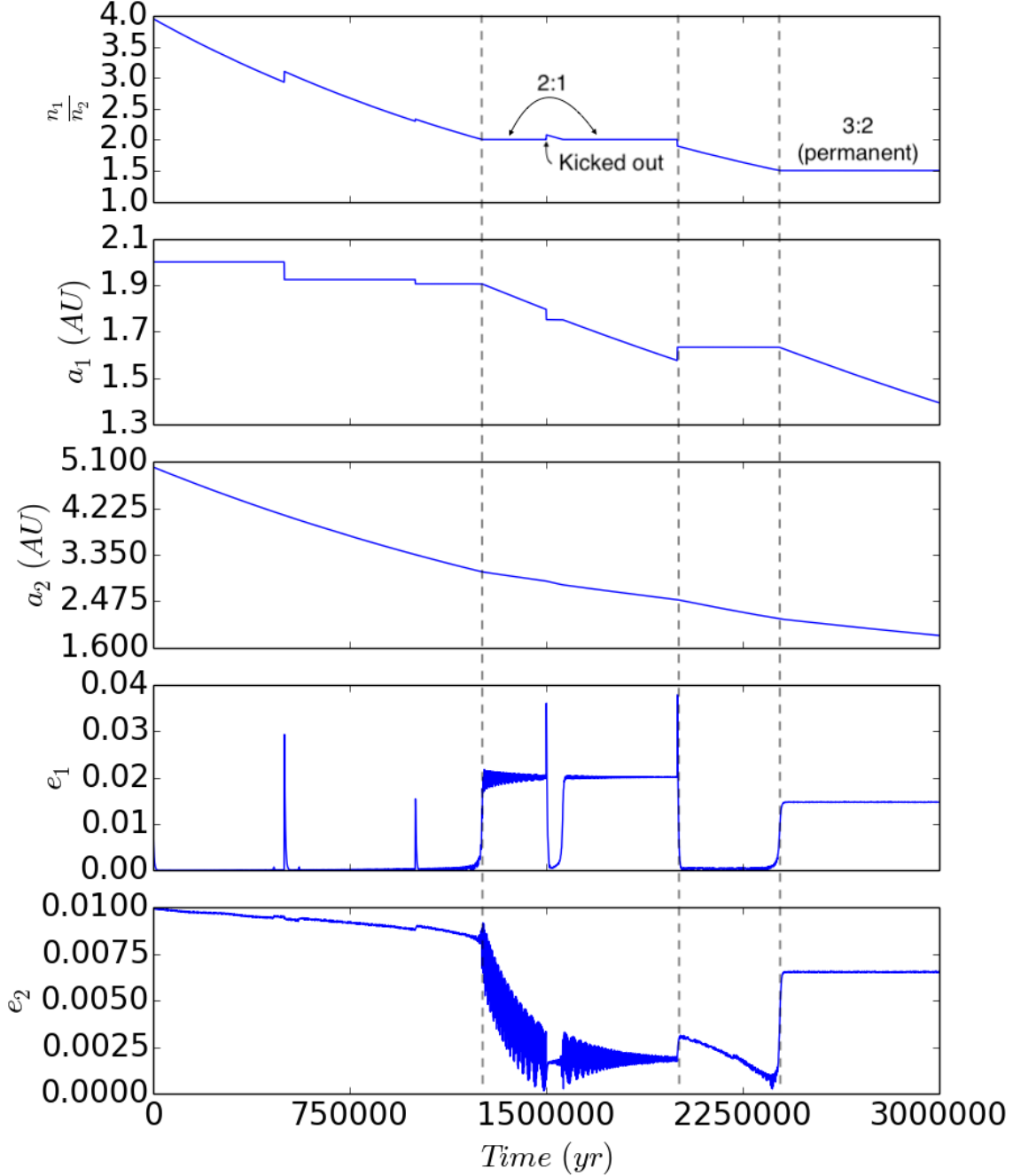


Figure 2.2: Sample integration. We plot the mean motion ratio  $\frac{n_1}{n_2}$ , semimajor axes  $a_1$  and  $a_2$ , and eccentricities  $e_1$  and  $e_2$  of both planets. The subscripts 1 and 2 denote Kepler 36b and c, respectively. Initial planetary masses and orbital elements are as in Table 2.2. The inner planet feels no drag force (i.e.,  $k_{a,1} = 0$ ), while  $k_{a,2} = 4 \times 10^{-7} \text{ yr}^{-1}$ . The eccentricity damping strengths are  $k_{e,1} = 3 \times 10^{-4} \text{ yr}^{-1}$  and  $k_{e,2} = 10^{-7} \text{ yr}^{-1}$ . The vertical dashed lines mark entrance ( $\sim 1.25 \times 10^6 \text{ yr}$ ) and exit ( $2.0 \times 10^6 \text{ yr}$ ) into the 2:1 MMR as well as entrance into the 3:2 MMR ( $\sim 2.4 \times 10^6 \text{ yr}$ ). The effects of collisions at 0.5, 1.0, 1.5, and 2.0  $\times 10^6 \text{ yr}$  are readily apparent, particularly in the  $e_1$  plot.

responsible; they are described by the resonant arguments  $\dot{\phi}_1 = jn_1 - kn_2 - \dot{\varpi}_1$  and  $\dot{\phi}_2 = jn_1 - kn_2 - \dot{\varpi}_2$  for positive integers  $j, k$  with  $j > k$ , where the subscripts 1 and 2 refer to the inner and outer bodies, respectively, and  $n$  and  $\dot{\varpi}$  refer to the bodies' mean motions and rates of periape precession, respectively. These resonances are not precisely colocated, i.e.,  $\dot{\phi}_1 \neq \dot{\phi}_2$ , as  $\dot{\varpi}_1 \neq \dot{\varpi}_2$ . This is due to the substantial planet-planet perturbations, which are strong enough to generate differential precession and split the resonances.

This resonance-splitting phenomenon is displayed in Fig. 2.3, where we plot both first-order resonances for the 2:1 MMR and 3:2 MMR. The inner 2:1  $e$  resonance (top panel) is active during both captures, as denoted by its low-amplitude libration near  $0^\circ$  between  $\sim 1.25 \times 10^6$  and  $2 \times 10^6$  yr, with a swift exit and re-entry at  $1.5 \times 10^6$  yr, as shown by the errant dots there. However, the outer 2:1  $e$  resonance (second panel) is only active during the second capture; it librates around  $180^\circ$ . Both inner and outer  $e$  resonances (third and fourth panels respectively) are also active during the 3:2 MMR capture after  $\sim 2.4 \times 10^6$  yr.

### 2.3.2 Effect of a Single Collision

In Fig. 2.2, kicks removed planets from resonance. We simulated impulses of various strengths and numerically determined that  $\frac{\delta v}{v} \gtrsim 1.67 \times 10^{-3}$  was required to eject planets from the 2:1 MMR (see Fig. 2.4). For such an impulse, assuming  $e_i = 0.2$  (following [24]), we calculate  $m_i \approx 8.05 \times 10^{-8} M_\odot = 2.18 M_{\text{Moon}}$  using our mass-approximation scheme from Section 2.2.2 and the state vectors from the

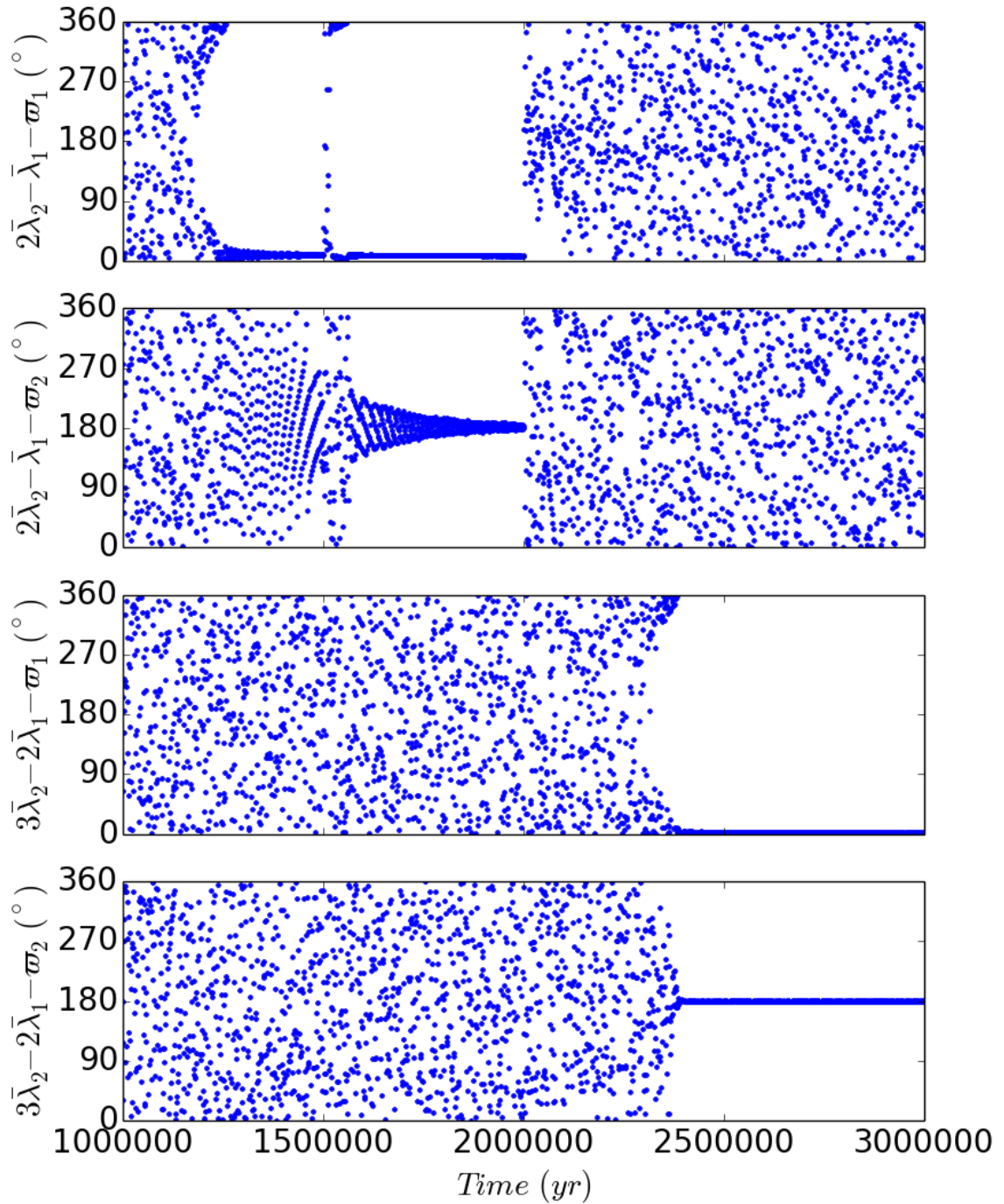


Figure 2.3: Inner and outer  $e$  resonances for the 2:1 MMR (top two panels) and 3:2 MMR (bottom two panels), where the subscripts 1 and 2 denote Kepler 36b and c, respectively, and  $\bar{\lambda}$  and  $\varpi$  denote mean longitude and longitude of periaapse, respectively. The inner  $e$  resonance is active for both 2:1 MMR captures, whereas the outer one is only active for the second capture.

outputs at 5,000 yr and 5,002 yr. Using a length unit of AU and a time unit of yr, these vectors were  $\mathbf{r}_p = (-0.8860873093, -0.2227002668, 2.909956005 \times 10^{-5})$ ,  $\mathbf{v}_p = (1.968863867, -6.93120374, -1.009533242 \times 10^{-4})$ ,  $\mathbf{r}_f = (-0.3684893442, -0.8413240048, 8.438573771 \times 10^{-6})$ ,  $\mathbf{v}_f = (6.453097908, -3.151421393, -2.353317075 \times 10^{-4})$ . One can use the state vectors to reproduce our mass estimate.

[33] and [24] also investigated the  $\frac{\delta v}{v}$  required to knock a larger body out of resonance. [33] analytically found that  $|\frac{\delta v}{v}| \approx \left(\frac{j^2}{j+1}\right)^{1/4} \mu^{1/2} \eta^{1/4}$  for a  $j+1 : j$  MMR (Eq. 30 in [33]). Here,  $\mu$  is the mass of the planet in units of the central star, and  $\eta \approx 0.80e_{\text{eq}}^2(j+1)$  for equilibrium eccentricity  $e_{\text{eq}}$ , yielding  $\frac{\delta v}{v} \approx \sqrt{j\mu e_{\text{eq}}}$ . Taking  $j = 1$ ,  $e_{\text{eq}} = 0.02$ , and  $\mu = 10^{-5}$ , as in Fig. 2.2, Malhotra's expression gives  $\frac{\delta v}{v} \approx 4.5 \times 10^{-4}$ , about a factor of four below our own estimate. The discrepancy may be due to the different context; [33] considered a single self-consistent model in which  $\dot{a}$  and  $\dot{e}$  were derived from a gas drag force. By comparison, we followed no such restrictions, allowing  $\dot{a}$  and  $\dot{e}$  to take a wide variety of independent values. As a result, the equilibrium eccentricity (a product of the eccentricity damping) was considerably less predictive of the resonance width and hence  $\frac{\delta v}{v}$  (a product of the semimajor axis damping) in our simulations as compared to those of [33]. [24] likewise found, using an order-of-magnitude approximation, that  $\frac{\delta E}{E} \approx \sqrt{(j+1)\mu e_{\text{eq}}}$  for fractional change in energy  $\frac{\delta E}{E}$ . For our impulses, which act along the velocity vector of the impacted body,  $\frac{\delta v}{v} \approx \frac{\delta a}{2a} \approx \frac{\delta E}{2E}$ , so the expressions from [33] and [24] agree to within a factor of two.

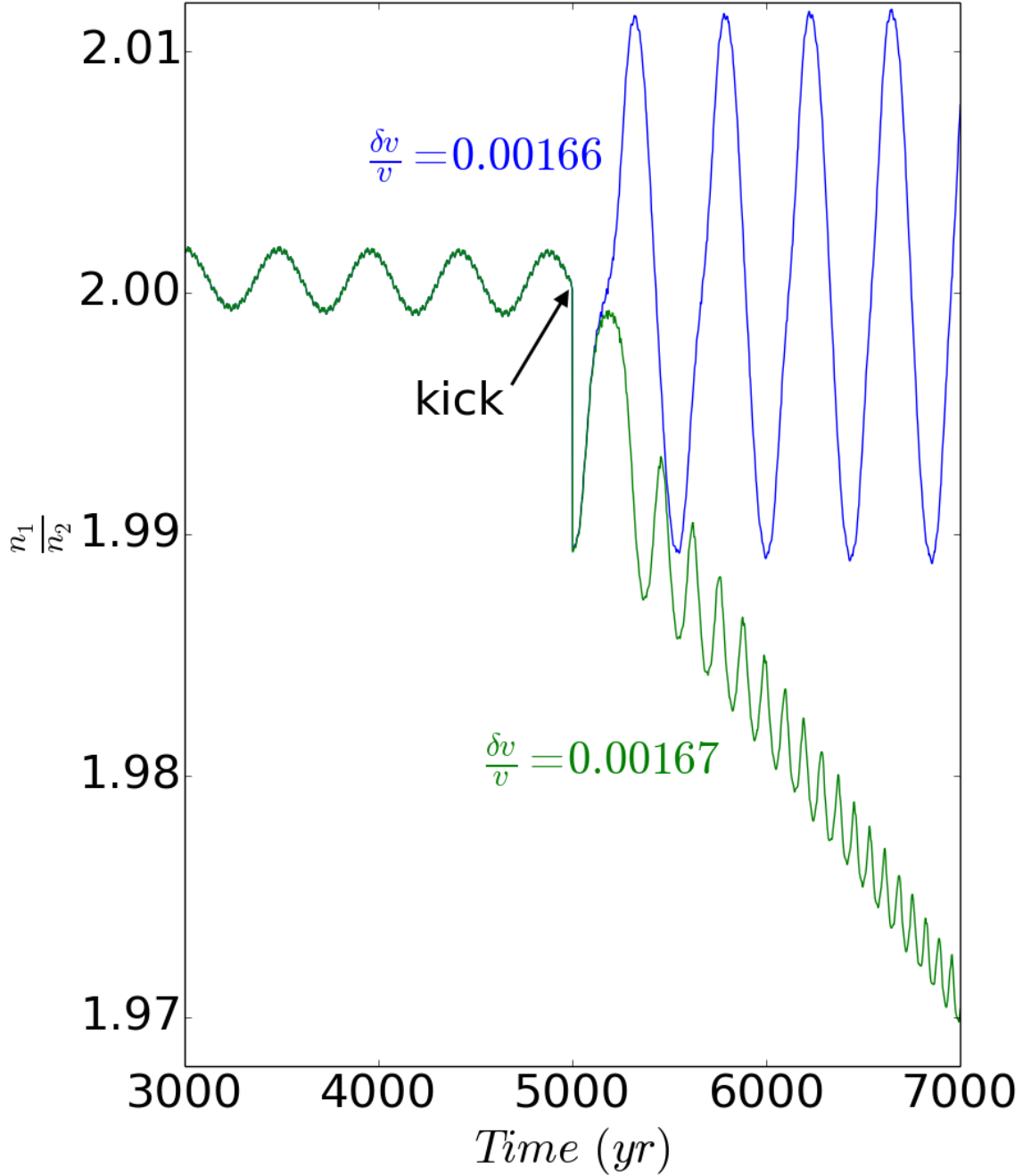


Figure 2.4: Two simulations showing the minimum  $\frac{\delta v}{v}$  required to eject Kepler 36b and c from the 2:1 MMR, with semimajor axis drag applied to the outer body only ( $k_{a,2} = 4 \times 10^{-6} \text{ yr}^{-1}$ ) and no eccentricity damping on either. The planets' masses are as in Table (2.2), and Kepler 36's mass is  $1.113 M_{\odot}$  [2]. At 3,000 yr, the planets are in the 2:1 MMR, and at 5,000 yr, we apply a kick to the inner body in the  $\hat{v}$  direction. For  $\frac{\delta v}{v} = 0.00166$  (the blue curve), corresponding to an estimated impactor mass of  $2.17 M_{\text{Moon}}$ , the bodies remain in resonance but librate with a much greater amplitude. For  $\frac{\delta v}{v} = 0.00167$  (the green curve), corresponding to an estimated impactor mass of  $2.18 M_{\text{Moon}}$ , the bodies exit resonance.

### 2.3.3 Individual Simulations

Our simulations demonstrated several distinct evolutionary paths the two planets could take to the 7:6 MMR. In Fig. 2.5, we show an example that requires only four collisions. This simulation is particularly intriguing due to the behavior from  $\sim 1.8 - 1.9 \times 10^6$  yr, during which the two bodies have sufficiently high eccentricities to experience close approaches during each orbit. These encounters nudge the two bodies closer to each other, seen clearly in the  $a_1$  panel (second from the top). This allows them to go directly to the 6:5 resonance, bypassing the 5:4 entirely and enabling 7:6 capture with relatively few collisions. Note that while we have tentatively identified the resonance from 1.5 to  $\sim 1.8 \times 10^6$  yr as the 4:3, the actual mean motion ratio at that point librates around  $\frac{n_1}{n_2} \sim 1.352$  (we expect libration around  $\frac{n_1}{n_2} \sim 1.333$ ), and both of the 4:3 eccentricity resonance arguments show no evidence of the expected libration about  $0^\circ$  or  $180^\circ$ . While secular effects may have moved the location of the 4:3 MMR, the mean motion ratios for the 6:5 and 7:6 resonances librate around their expected values of  $\frac{n_1}{n_2} \sim 1.2$  and  $\frac{n_1}{n_2} \sim 1.167$ . Investigation of the nearby, weaker 7:5 and 11:8 MMRs likewise proved fruitless – we saw no libration indicative of capture in their resonance arguments. Nevertheless, we know this phenomenon must be an MMR because the mean motion ratio remains flat, and we believe that it is the 4:3 simply because that is the closest strong resonance.

In Fig. 2.6, a series of nine somewhat serendipitous collisions moves the bodies to ever closer resonances, culminating in 7:6 capture. This simulation is fairly representative of our ‘successful’ simulations (i.e., those that end in the 7:6 MMR). Most

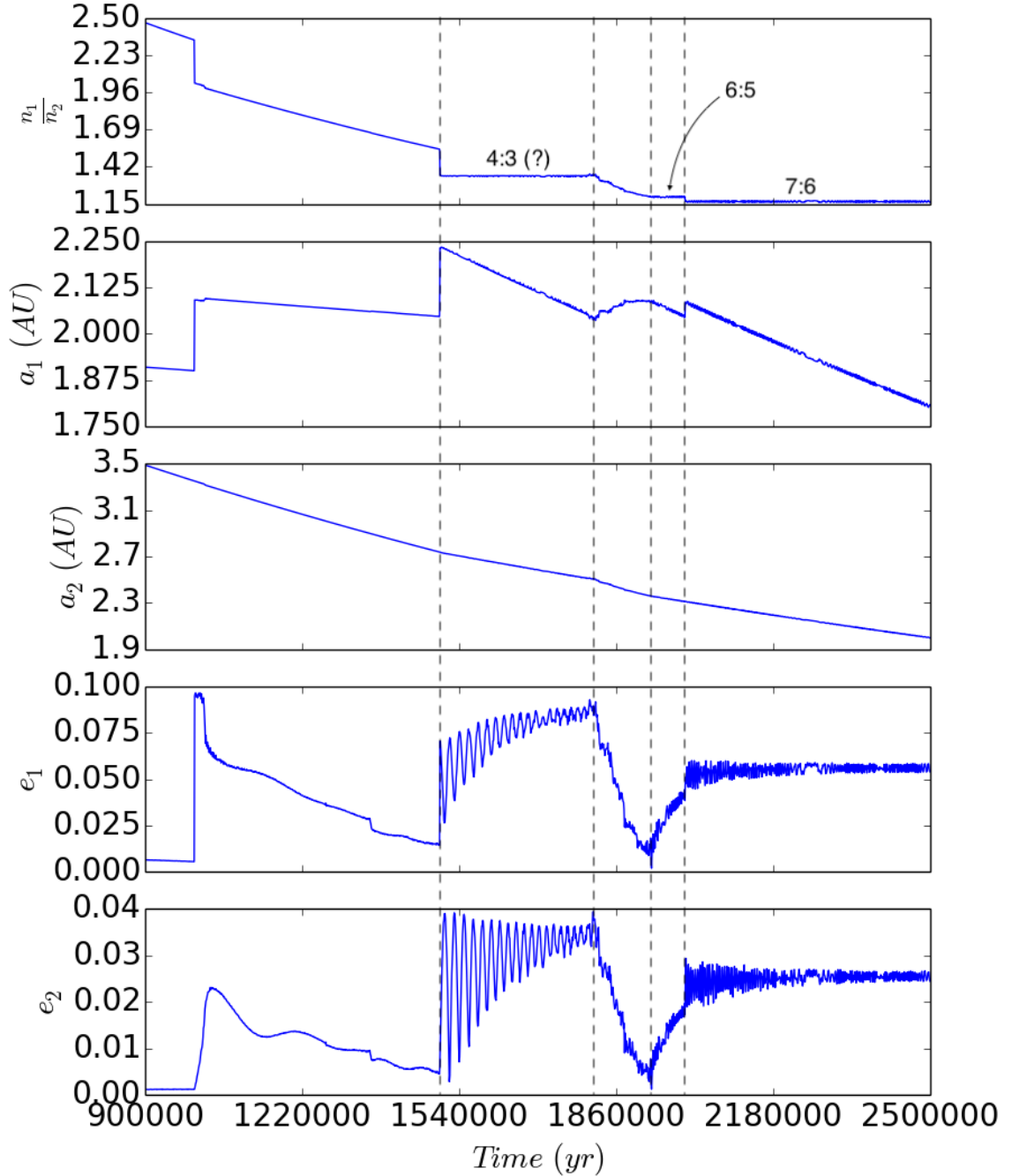


Figure 2.5: Example of permanent 7:6 capture with four collisions, at  $0.5$ ,  $1$ ,  $1.5$ , and  $2 \times 10^6$  yr. We display results between  $0.9$  and  $2.5 \times 10^6$  yr to highlight the interesting behavior therein. The top panel shows the mean motion ratio of the two planets; the second and third show the inner and outer planetary semimajor axes; and the fourth and fifth show the inner and outer planetary eccentricities. We denote entry into and exit from resonance with dotted vertical lines; the specific resonances are noted, although we are unsure of the 4:3 (see text). Our disk parameters were  $k_{a,1} = 5 \times 10^{-8} \text{ yr}^{-1}$ ,  $\frac{k_{e,1}}{k_{a,1}} = 1$ ,  $\frac{k_{e,2}}{k_{a,2}} = 30$ , and  $k_{a,2} = 4 \times 10^{-7} \text{ yr}^{-1}$ . Given typical impactor eccentricities of  $0.25$ , we estimate that the inner body accreted  $\sim 1.50M_{\oplus}$ , ending with  $4.8M_{\oplus}$  – about 10 per cent above the observed value of  $4.45M_{\oplus}$  (see Table 2.1).

impulses not only kick the planets together, but do so with just the right strength – powerful enough to bypass resonances, but weak enough to avoid instability. In addition, the impulses cease immediately after entrance into the 7:6 MMR, ensuring its survival. Unsurprisingly, the probability of all these conditions being present simultaneously is low.

In our final example (Fig. 2.7), we show a simulation with two 7:6 captures, the second of which was permanent. This simulation was noteworthy because of the high number (fifteen) of collisions - the greatest number we tested. Due to  $5 \times 10^5$  yr collision spacing, this meant that several collisions occurred when the planets orbited quite closely to one another after migrating inward for several millions of years. Eccentricity damping prevented orbit crossing, but there were still two interesting consequences. First, as resonances clustered more tightly, planets could be knocked apart and recaptured into a more distant resonance than before; this happened at  $6 \times 10^6$  yr (the planets were kicked from the 7:6 MMR to the 9:7) and at  $7 \times 10^6$  yr (kicked from the 6.5 to the 5:4). The close resonant spacing effectively destroyed the asymmetry in which randomly oriented kicks preferentially moved the planets to successively closer resonances. In turn, this kept them from moving into very close resonances such as the 8:7 or 9:8.

In addition, the bottom two panels, showing the inner and outer planetary eccentricities, clearly show how as the planets get closer and closer, the perturbing force they apply on each other grows. The first eccentricity resonance corresponding to the 3:2 MMR librates very narrowly around its equilibrium value, but as the radial separation between orbits shrinks, each resonance’s libration amplitude increases. In

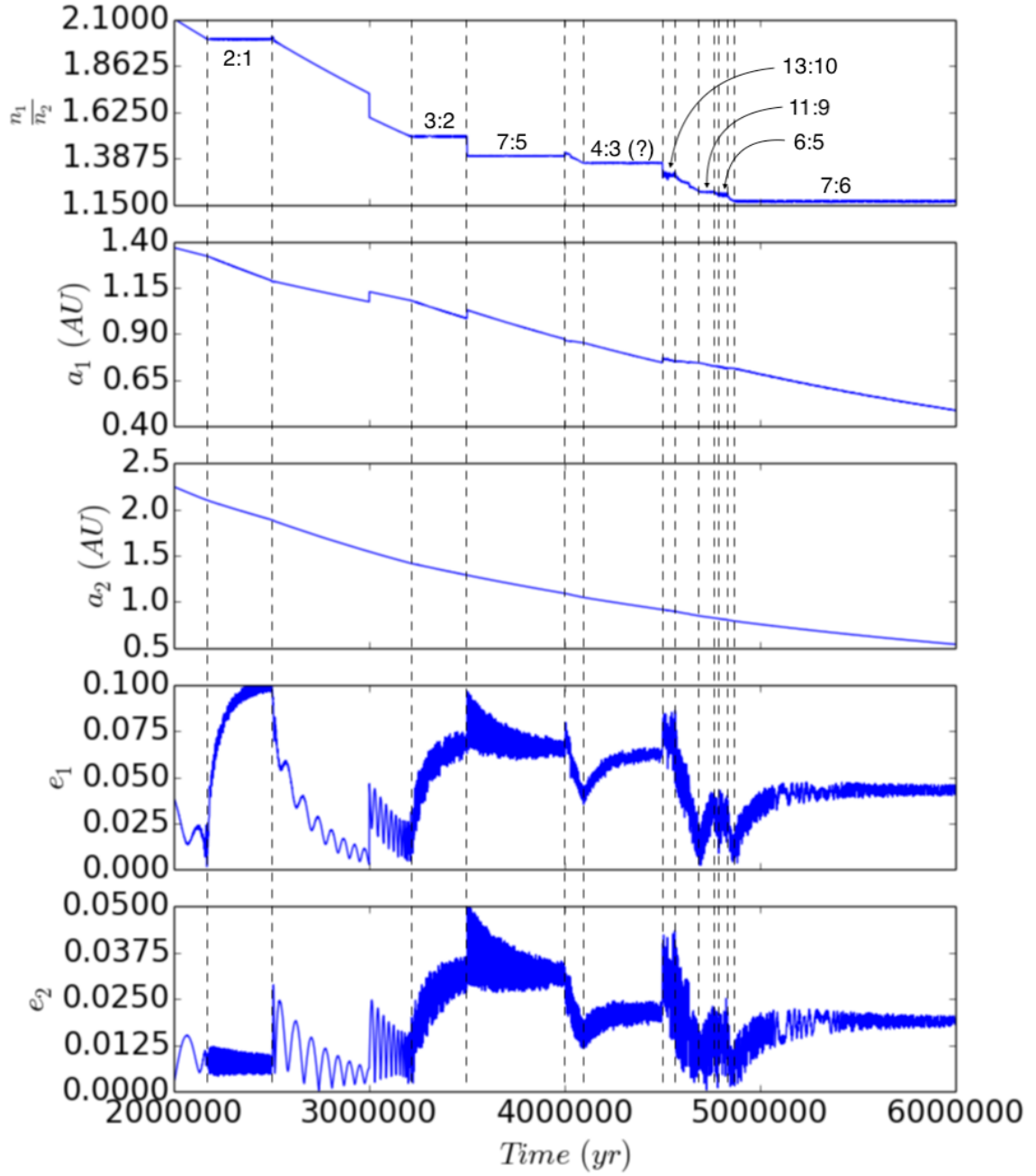


Figure 2.6: Example of permanent 7:6 capture with nine collisions. We display only results between  $2$  and  $6 \times 10^6$  yr. As in Fig. 2.5, the mean motion ratio in the interval marked “4:3 (?)” librates about an unusual value (here  $\sim 1.364$ ); we are again unsure if this truly is the 4:3 MMR. Our disk parameters were  $k_{a,1} = 2 \times 10^{-7} \text{ yr}^{-1}$ ,  $\frac{k_{e,1}}{k_{a,1}} = 30$ ,  $\frac{k_{e,2}}{k_{a,2}} = 1$ , and  $k_{a,2} = 4 \times 10^{-7} \text{ yr}^{-1}$ . We estimate that the inner body accreted  $\sim 1.89M_{\oplus}$ , ending with  $5.19M_{\oplus}$ .

addition, as the planets get very close to each other, the inner and outer eccentricity resonances begin to overlap. [35] derive a criterion that predicts when this overlap begins in the limit of a test particle orbiting an oblate planet; in principle, one could adapt their criterion for our purposes, but that would require estimating secular precession rates and is beyond the scope of this chapter. Since the two resonances are of roughly equal strength, they jostle for control with neither dominating the other, raising the libration amplitude. Finally, note that while the bodies are in the sole second order resonance, the 11:9, their eccentricity oscillations do not appear to damp. This may be due to a longer damping timescale associated with the weaker resonance.

### 2.3.4 Summary and Mass Calculations

Of our 7,020 simulations, 84 (about 1.2 per cent) ended with the two bodies in a resonance with a period ratio within 1 per cent of 7:6. For each of those 84 simulations, we estimated the total accreted mass  $m_{\text{total}}$  assuming a variety of impactor eccentricities  $e_i$ ; Fig. 2.8 shows how  $m_{\text{total}}$  varied with selected  $e_i$  for each simulation.

Since mass varies quite considerably with our choice for  $e_i$ , we cannot conclude how much mass would have ‘actually’ been accreted. Nevertheless, it is clear that, as long as the assumed impactor eccentricity is not too low (the lower the impactor eccentricity, the lower the collision speed between impactor and planet and conversely the higher the impactor mass must be), it is simultaneously possible for the

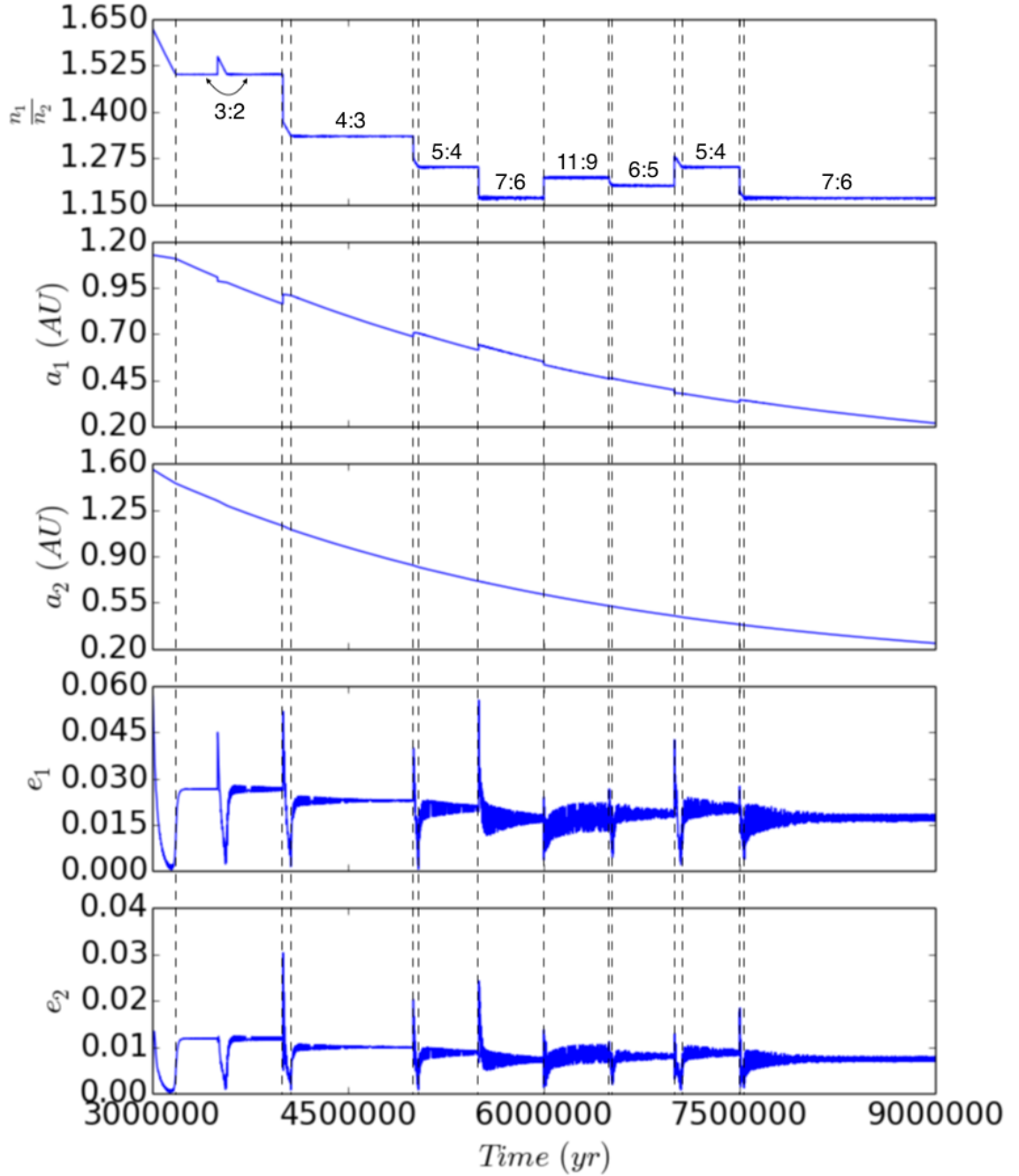


Figure 2.7: Example of permanent 7:6 capture with fifteen collisions. We display only results between  $3$  and  $9 \times 10^6$  yr. Our disk parameters were  $k_{a,1} = 10^{-7} \text{ yr}^{-1}$ ,  $\frac{k_{e,1}}{k_{a,1}} = 30$ ,  $\frac{k_{e,2}}{k_{a,2}} = 300$ , and  $k_{a,2} = 4 \times 10^{-7} \text{ yr}^{-1}$ . We estimate that the inner body accreted  $\sim 4.63M_{\oplus}$ , ending with  $7.33M_{\oplus}$ .

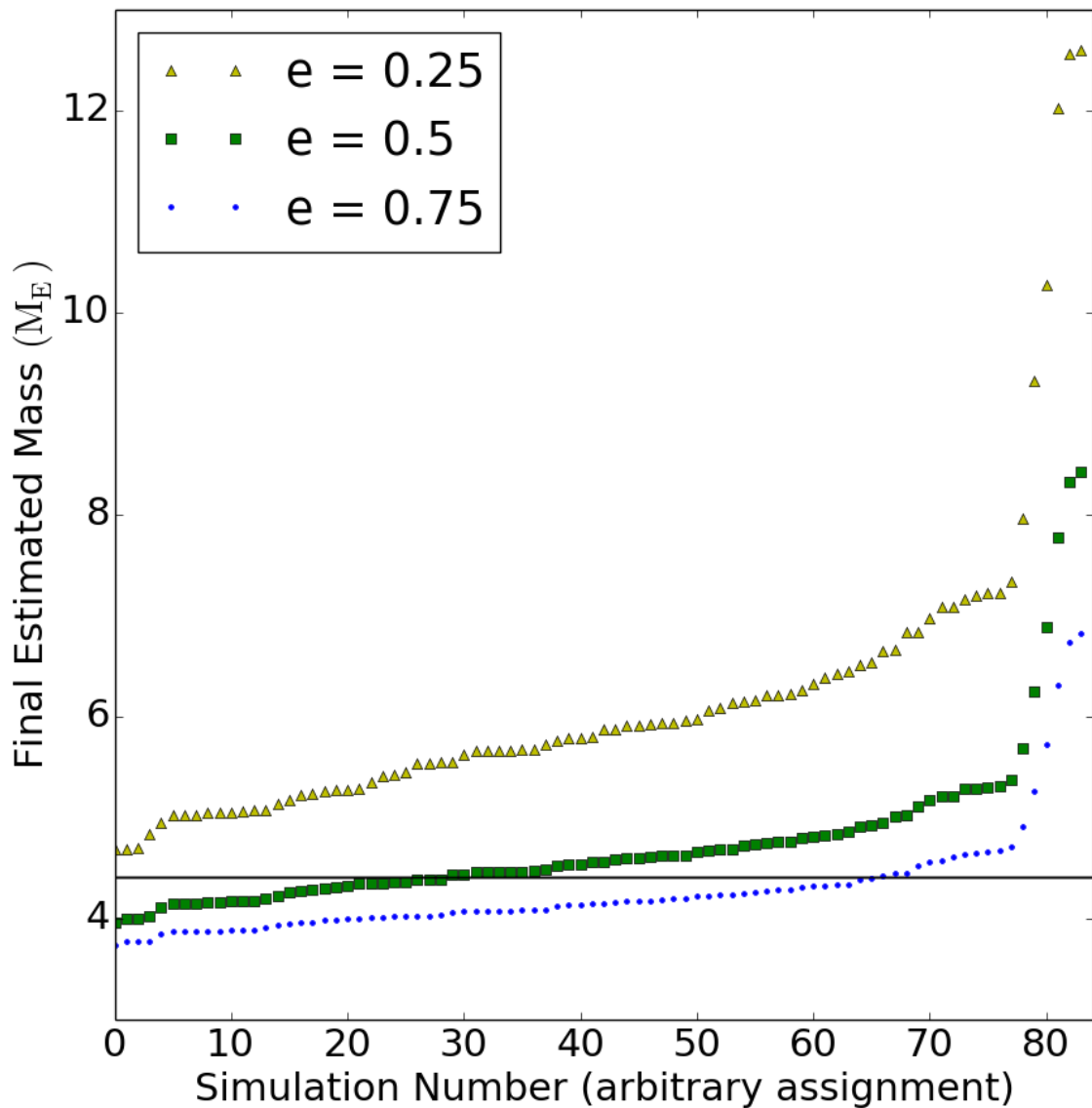


Figure 2.8: Final estimated mass, using three different assumptions for  $e_i$ , for each simulation that ended in or near the 7:6 MMR. The solid black line indicates Kepler 36b's current observed mass.

planets to end in the 7:6 MMR and for the simulated Kepler 36b to accrete sufficient mass to end at or near its current observed mass. Naturally, simulations with fewer collisions tended to end with less accreted mass on the inner body.

In Table 2.3, we show ‘hot spots’ - clusters of parameter values that are similar to one another - within the parameter space of simulations that ended with the bodies in the 7:6 MMR. Forty two simulations are included. Rather than a few large clusters, we found many small ones, indicating that capture into the 7:6 resonance did not depend strongly upon the strength of the disk interactions with the planets or upon number of collisions. The most successful cluster used  $k_{a,1} = 5 \times 10^{-8} \text{ yr}^{-1}$ ,  $\frac{k_{e,2}}{k_{a,2}} = 300$ , and eight collisions. That combination of values yielded four integrations that terminated in the 7:6 MMR, corresponding to  $\frac{k_{e,1}}{k_{a,1}} = 1, 3, 10, \text{ and } 30$ . However, apart from that cluster and a few others, there were few obvious patterns in the parameter space.

In Table 2.4, we show the disk parameters for all simulations that ended in a stable 7:6 MMR but were not in a ‘hot spot’; coincidentally, there are again forty two (or perhaps not coincidentally – see [36]). Perhaps the most notable difference between the simulations in Tables 2.3 and 2.4 is the collision sets. A majority of the simulations in Table 2.3 featured eight, nine, or eleven collisions, whereas those in Table 2.4 were more evenly distributed in this parameter. However, with that exception, there are few differences of obvious statistical significance between the two Tables. This reinforces the idea that disk parameters may not play a decisive role in determining entry or exit into the 7:6; a series of reasonably ‘fortunate’ collisions is clearly necessary and may also be sufficient.

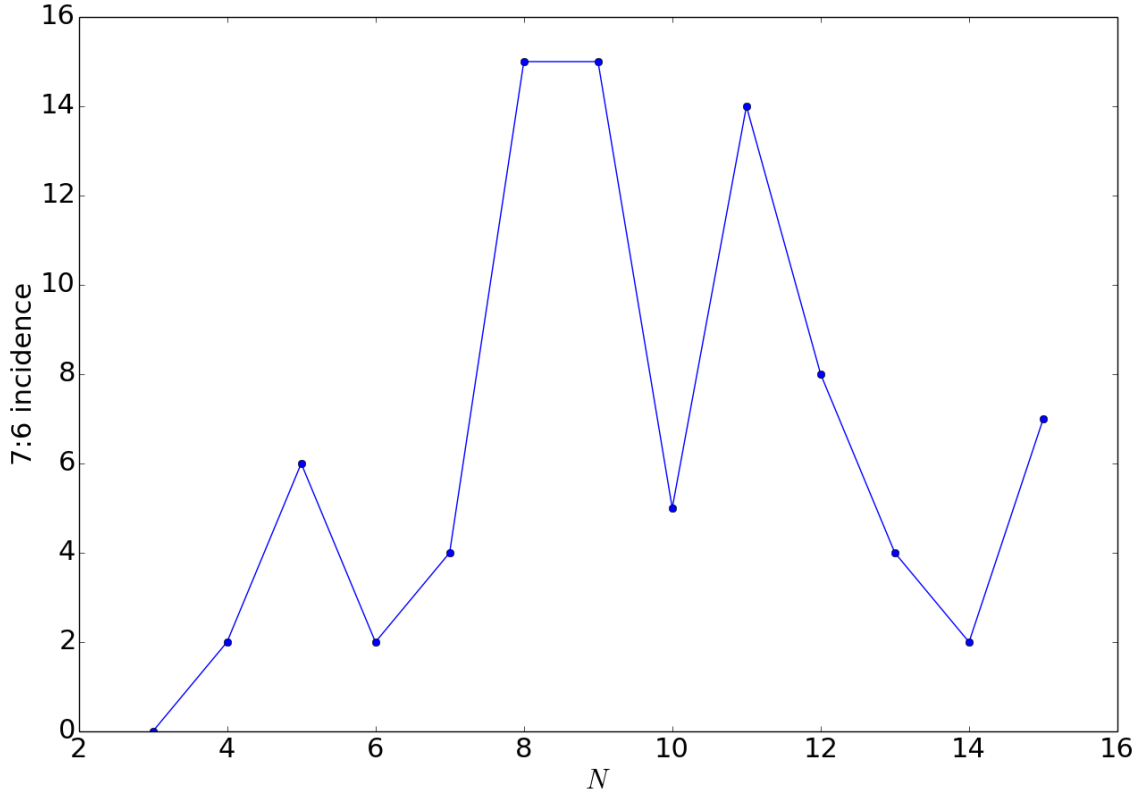


Figure 2.9: Number of simulations that ended in or near the 7:6 MMR for each number of collisions  $N$ . Little more than the broad outlines of a pattern can be seen.

Finally, in Fig. 2.9, we show how the number of simulations ending in the 7:6 MMR varies with  $N$ . Unfortunately, we cannot draw many firm conclusions here. While the curve somewhat resembles a Gaussian centered around  $N = 8$  or  $9$ , the points at  $N = 6, 7, 10$ , and  $15$  all significantly depart from their expected values. To quantify how meaningful these departures are, we used the Shapiro-Wilk test, which tests the null hypothesis that a data sample comes from a normal distribution. This yielded a  $p$  value of 0.052, providing further evidence that the similarity of these data to a Gaussian sits right at the edge of statistical significance.

$k_{a,1}$ ( $\times 10^{-7}$ yr $^{-1}$ )	$\frac{k_{e,1}}{k_{a,1}}$	$\frac{k_{e,2}}{k_{a,2}}$	Collision Set
0.5	30, 100	30	5a
0.5	300	3, 10	5b
1	30	1, 3	8a
1	30, 100, 300	300	8b
1	100	3, 300	8b
1, 0.5	30	300	8b
0.5	1, 3, 10, 30	300	8b
0.5	3, 10	100	8b
2	30	1, 3	9a
1	3, 100	300	9a
1, 0.5	300	100	9a
1	300	3, 300	9b
0.5	100, 300	3	9c
2	1, 10, 30	300	11a
2	10, 30	30	11b
1	10, 30, 300	300	11c
1	1	30	12a, 12b
1	1, 10	30	12b
0.5	300	10	12a, 12c
0.5	300	300	15a, 15b
0.5	300	30, 300	15b

Table 2.3: Selected disk parameter sets that produced simulations ending in the 7:6 MMR. Every set is identical to at least one other set except for a single condition, denoted by multiple values separated by commas; there are forty two such unique sets. Recall that for every number of collisions, we used five different sets of collision strengths. In the Collision Set column, we specify the number of collisions and differentiate between different sets with the letters a-e; e.g., the sets 8a and 8b both have eight collisions but with different collision strengths, while the sets 5a and 8a are unrelated. In addition,  $k_{a,2} = 4 \times 10^{-7}$  yr $^{-1}$  for every simulation.

$k_{a,1}$ ( $\times 10^{-7}$ yr $^{-1}$ )	$\frac{k_{e,1}}{k_{a,1}}$	$\frac{k_{e,2}}{k_{a,2}}$	Collision Set
0.5	1	30	4a
1	30	1	4a
0.5	100	100	5b
1	3	30	5b
0.5	100	3	6a
1	30	10	6a
1	3	100	7a
1	30	3	7a
1	100	10	7a
2	10	1	7a
0.5	100	30	8b
1	1	100	8a
1	3	30	8c
0.5	1	30	9a
0.5	30	10	9a
0.5	30	300	9b
1	100	100	9b
2	30	30	9b
0.5	1	30	10a
1	30	10	10a
1	100	3	10b
2	1	10	10b
2	10	1	10b
0.5	3	30	11a
0.5	10	100	11a
1	3	300	11b
1	30	3	11d
2	100	10	11c
2	300	3	11a
0.5	1	100	12a
0.5	1	300	12b
1	300	30	12a
0.5	300	1	13a
1	30	300	13b
1	300	3	13a
2	1	30	13b
0.5	1	30	14a
1	1	3	14a
0.5	100	10	15a
0.5	100	30	15b
1	30	300	15a
2	1	30	15a

Table 2.4: Selected disk parameter sets that produced simulations ending in the 7:6 MMR. Every set differs from every other set by at least two parameters; there are again forty two such sets. In every simulation,  $k_{a,2} = 4 \times 10^{-7}$  yr $^{-1}$ .

## 2.4 Comparison to Observations

We mined our dataset of 7,020 simulations for statistics on resonant populations using a custom python script. The script first determines which outputs, if any, must be checked for resonance by calculating  $\frac{a_2}{a_1}$  for each. The first output is always checked. If the planets have exchanged positions, i.e.  $\frac{a_2}{a_1} < 1$ , the output is marked as such. In general,  $\frac{a_2}{a_1}$  should monotonically decrease in the absence of resonance, so the vast majority of simulations in which the planets exchanged positions ended with the newly inner body spiraling into the star.<sup>2</sup> Otherwise, an output is flagged as potentially in resonance if:

- a) the previous output is in a recognized resonance, but the current output is no longer sufficiently nearby,
- b) the previous output is in an unrecognized resonance, or
- c) the previous output is not in resonance, and its  $a$  ratio is smaller than that of the current output.

If the previous output is in a recognized resonance and the current output is sufficiently close to it, it is marked as being in that resonance; if the previous output is not in resonance and its  $a$  ratio is larger than that of the current output, the current output is marked as not being in resonance.

After determining which outputs must be checked for resonance, the script evaluates each by studying test sequences of twenty consecutive  $a$  ratios, beginning

---

<sup>2</sup>We manually examined simulations in which the bodies exchanged positions but ended with a  $\frac{a_2}{a_1}$  value on the order of unity and found none that ended in the 7:6 resonance.

with the  $a$  ratio corresponding to the output being checked. We use two criteria to test for resonance. For each test sequence, the script compares the average of the first four elements to the average of the last four elements. The averages must be sufficiently close, i.e.,  $\frac{a_2}{a_1}$  must be sufficiently flat, for the sequence to satisfy the first criterion. In addition, the script counts the number of times  $\frac{a_2}{a_1}$  increases from one output to the next within the test sequence. The second criterion is satisfied if the number of  $\frac{a_2}{a_1}$  increases is sufficiently high, indicating the oscillatory behavior characteristic of resonance. This approach takes advantage of our unique conditions in which  $\frac{a_2}{a_1}$  monotonically decreases in the absence of resonance due to our migration forces. If the sequence satisfies both criteria, the output corresponding to the first  $a$  ratio of the sequence is marked as in resonance. The specific resonance is determined by checking if the  $\frac{a_2}{a_1}$  value is within 0.5 per cent of the  $\frac{a_2}{a_1}$  value of the 2:1, 3:2, 4:3, 5:4, 6:5, 7:6, 8:7, 9:8, 5:3, 7:5, 9:7, 11:9, 7:4, 8:5, 10:7, 11:8, 13:10, 14:11, 9:5, or 11:7 MMR. If none of these proves a match, the output is labeled as being in some other resonance.

In Fig. 2.10, we report the incidences of resonances in which each simulation ended and compare them to those observed in nature. Pairs are considered to be sufficiently close to a  $j + k : j$  MMR if they satisfy the condition:

$$\epsilon = \left| 1 - \frac{(j+1)n_2}{jn_1} \right| < 0.01\xi^{k-1}, \quad (2.2)$$

where  $\xi$  is a tuneable parameter that allows us to account for the narrower widths of higher-order resonances. Using this criterion, all pairs within one per cent of

a first-order MMR location are included regardless of  $\xi$ , but weaker, higher-order resonances are increasingly excluded for smaller  $\xi$ .

The plots in Fig. 2.10 show some agreement in the overall trend – in both cases, resonant incidence peaks at the 3:2, and in general, the lower the order of the resonance, the greater its incidence relative to nearby higher-order ones. While we consider this encouraging, there are also significant differences that require explanation, particularly for the  $\xi = 1$  case, in which all pairs are considered resonant if they are within one per cent of a resonance location regardless of order. First, relative lower-order resonant incidence is much greater in reality than in our simulations; second, overall resonant incidence is much higher in our simulations than in reality.

In our model, all evolution ceases after  $10^7$  yr under the assumption that the protoplanetary disk has expired; the planetesimal swarm is depleted of high-mass objects and the planets no longer migrate. However, this is not true in reality; we expect that typically, collisions with the potential to knock bodies out of resonance would continue well after the protoplanetary disk phase. After the planets ceased to migrate, re-entry into a resonance would be very difficult if a collision knocked them out of it. Consequently, whenever the swarm still had high-mass bodies remaining subsequent to the protoplanetary disk phase, we would expect many of the planets in resonances to be kicked out. Our neglect of this process could explain why our simulations report resonances to be more common than they actually are. However, if most natural resonances are relics from their systems' gas disk phases, the relative resonance incidences from both simulations and reality should resemble each other.

Furthermore, in our simulations, resonant incidence was placed in a clear hier-

archy depending on the order of the resonance – lower-order resonances had greater incidence. This trend is far less noticeable – though not entirely absent – in the actual exoplanet data. We believe that this again may be a result of our simplified disk model; a true disk would smoothly transition from rapid migration to no migration as the density asymptotically approached zero. Therefore, as the disk waned and migration slowed, lower-order resonances would have much greater chances of capture. Unfortunately, due to the low population numbers of observed resonances (i.e. 7:6, 8:9, etc.), performing more rigorous statistical comparison between the two models is difficult. In future work, we could test these ideas by refining our disk model and simulating a period of collisions without convergent migration.

Finally, in Fig. 2.10, we compare our resonance statistics to those of most observed resonant pairs regardless of their masses. However, we designed our simulations with the Kepler 36 system in mind and did not attempt to model, e.g., the evolution of gas giants. Higher-mass planets might open a gap in the gas disk and therefore experience Type II migration. They would also be more difficult to eject from resonance and thus would be more likely than lower-mass planets to occupy not only more distant resonances, but weaker ones as well. This may explain why our simulations report a relative dearth of resonances between the 3:2 and 2:1 compared to observations.

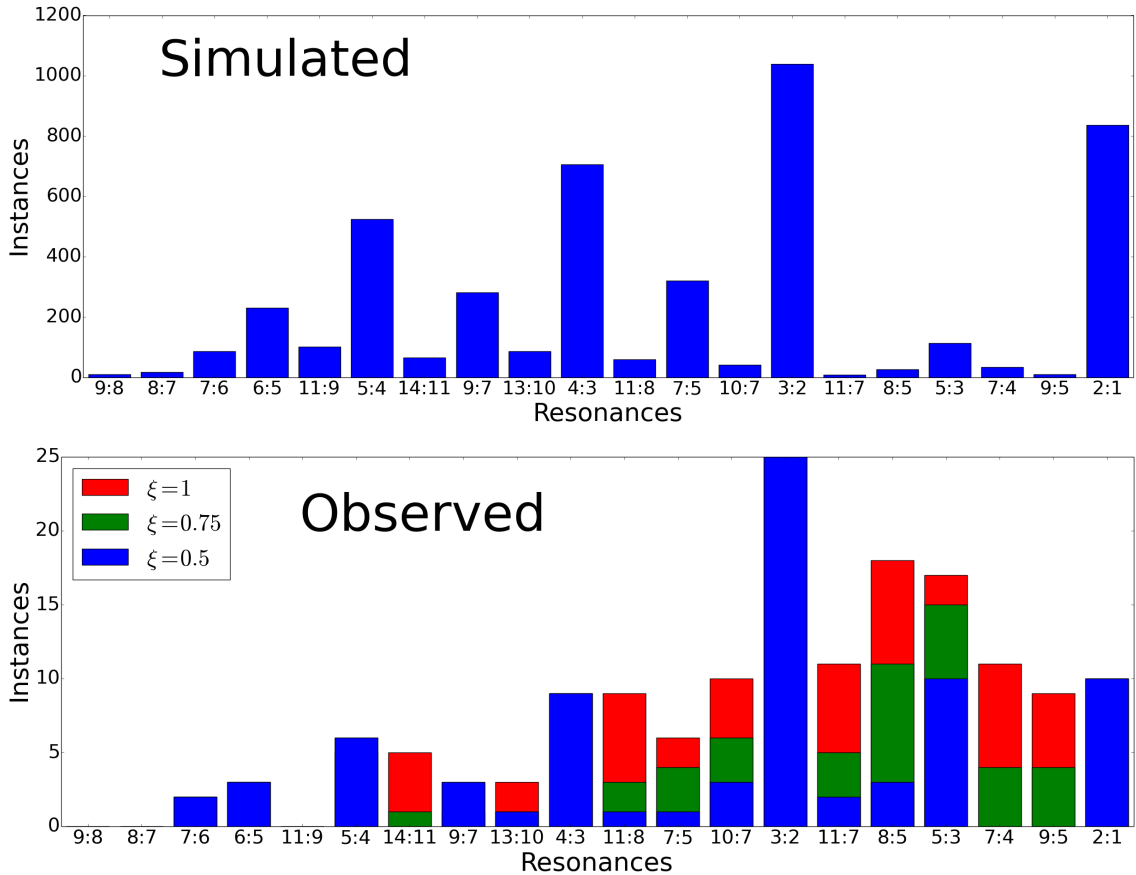


Figure 2.10: Simulated (top) versus observed (bottom) resonance incidence for selected MMRs. In the simulated plot, we refer to the resonance in which each simulation ended; we have excluded simulations that ended with swapped planetary positions (1,923 of 7,020 total), did not end in resonance (172), or ended in an unidentified resonance (327). Observed data is taken from exoplanet.eu and is current as of 18 May 2020; we only include confirmed, radially adjacent planets with period errors known to be less than one per cent. Results for  $\xi = 1$ , 0.75, and 0.5 are shown overlaid upon each other (see text). As  $\xi$  decreases, the observed data increasingly resembles the simulated data, most notably for  $\xi = 0.5$  (blue).

## 2.5 DISCUSSION

### 2.5.1 Broader Implications

We have demonstrated a possible mechanism to keep convergently migrating planets from getting too close to each other (Fig. 2.7). Once the distance  $\delta a_r$  between resonances is comparable to the typical  $\delta a_i$  from an impact, collisions no longer preferentially move planets together and instead have a roughly even chance of moving the planets into a closer or farther resonance. This condition is satisfied when resonances are “bunched up” together. We quantify this statement by noting that  $\frac{\delta v}{v} \approx \sqrt{j\mu e_{eq}}$  (Sec. 2.3.2). Substituting  $\frac{\delta a_i}{2a} \approx \frac{\delta v}{v}$  gives

$$\frac{\delta a_i}{a} \approx 2\sqrt{j\mu e_{eq}}. \quad (2.3)$$

Via eq. (8.203) from [5], the distance  $\frac{\delta a_r}{a}$  between a  $j+1 : j$  MMR and a  $j+2 : j+1$  MMR is

$$\frac{\delta a_r}{a} = \left(\frac{j+1}{j+2}\right)^{\frac{2}{3}} - \left(\frac{j}{j+1}\right)^{\frac{2}{3}} \approx \frac{2}{3j^2}. \quad (2.4)$$

Setting  $\delta a_r \approx \delta a_i$  and solving for  $j$  gives

$$j_{cr} \approx (9\mu e_{eq})^{-\frac{1}{5}}. \quad (2.5)$$

For the case of  $\mu = 10^{-5}$  and  $e_{eq} = 0.05$  (Figs. (2.5) and (2.6)), this gives  $j_{cr} \approx 12$ ,<sup>3</sup>

---

<sup>3</sup>If we use the exact equation for  $\frac{\delta a_r}{a}$  and numerically solve for  $j_{cr}$ , we get  $j_{cr} \approx 11$ .

i.e., predicts that at the 13:12 MMR, impacts are equally likely to move the planets into a closer or farther resonance. Given the dearth of both simulated and observed first-order MMRs beyond the 7:6, we might have expected  $j_{\text{cr}} \approx 7$ , but we think that the difference can again be explained by the different damping force assumptions we used versus [33]. Indeed, comparing between Figs. 2.5, 2.6, and 2.7, the equilibrium eccentricity varies substantially even for the same resonances. This is due to our choice of testing many different values of  $\frac{\dot{e}}{a}$ , whereas [33] considered a single model for gas forces.

We can also calculate the chaotic overlap criterion value  $j_{\text{ch}}$  given by [37]:

$$j_{\text{ch}} \approx 0.5\mu^{-\frac{2}{7}}, \quad (2.6)$$

defined such that all  $j+1 : j$  MMRs with  $j > j_{\text{ch}}$  overlap. Plugging in  $\mu = 10^{-5}$  gives  $j_{\text{ch}} \approx 13$ , which is consistent with our simulations; the first-order MMRs appear to be well defined in our data. Ideally, we could also compare  $j_{\text{ch}}$  with  $j_{\text{cr}}$ ; however, the unreliability of our  $j_{\text{cr}}$  estimate renders this comparison rather unhelpful.

## 2.5.2 Limitations

As noted in Sec. 2.2.2, we neglected to update the inner planet’s mass each time it was hit with an impulse. As Fig. 2.8 shows, this was not a trivial omission; in many cases, the inner body’s mass would have doubled or even tripled. Bodies with more mass are, of course, more resistant to perturbation, so had we updated the masses, the simulated planets may have not been kicked out of resonance as

easily. This choice therefore may have skewed our statistics towards closer-together resonances.

In addition, we ended the simulations after  $10^7$  years, assuming that the gas disk, and hence disk forces, would no longer exist after then. In particular, we ignored post-disk collisions and other sources of migration. As our result, most of our simulated planets ended in resonance – the opposite of what is observed in reality. We suspect that collisions occurring after the disk has dissipated would significantly lower resonant populations. In addition, [38] study the effects of the rebound of the magnetospheric cavity in the gas disk dispersal phase. They find that a pair of super-Earths in an MMR with a more massive outer planet can experience divergent migration, breaking them out of resonance. [39] produce another such mechanism; they show that tidal dissipation can cause planets in or near an MMR to repel each other.

## 2.6 CONCLUSIONS

We have shown that planets migrating inward in a gas disk can successfully reproduce many features of the Kepler 36 planetary system, including both its unusually close 7:6 MMR as well as its observed masses. By construction, the model is also capable of modeling density contrast. Furthermore, these results are possible in a variety of disks, including both disks that strongly affect the planets'  $a$  and  $e$  as well as disks with a much lighter touch, as our successful simulations are relatively insensitive to these disk parameters (Table 2.3). Since the Kepler 36 system appears

to be unique, with no other known comparable pairs of planets inhabiting the 7:6 MMR, our success rate of around 1.2 per cent is low but not necessarily worrisome and may in fact be required. Indeed, the relative 7:6 MMR incidence of our simulations is qualitatively similar to that observed in reality. Although the small number of known planets within tightly packed systems prevents us from performing rigorous statistical analysis, our modeled rate is consistent with the observed rate. We again caution, however, that this modeled rate may have substantially decreased had we updated the inner planet's mass each time it was kicked. As more planets in tightly packed MMRs are discovered and we are able to estimate the true 7:6 incidence with greater precision, this disparity may need to be revisited and our work revised.

Furthermore, we accomplished this goal without invoking planet position swapping and mantle stripping, as required by [24], or high-energy radiation models with the planets forming in situ, as required by [1]. While our model also required assumptions, e.g., of impactor mass and the planets' initial conditions and masses, we argue that these assumptions are at least as reasonable as those made by these other approaches. [1] assume favorable initial conditions; in particular, they choose an initial core mass for Kepler 36b that equals its current mass, so the problem reduces to simply burning off the inner planet's envelope while leaving that of the outer one intact. This ignores the problems of how such a high-mass core could form in the first place along with how the two planets could be found so close together with such different properties and small semimajor axes. While we undoubtedly assume a convenient starting mass for the outer planet, this choice (i.e., placing a

gaseous sub-Neptune at 5 AU) is more consistent with standard planetary formation theory. Furthermore, as we noted in Section 2.1.1, we think that lower-mass bodies are likely to migrate slower, not faster, than higher-mass ones. Thus, we sidestep the problematic assumption in [24] that Mars-mass embryos initialized far away from the star would catch up and collide with the two closer planets. This assumption is crucial for the success of their model, which relies on these collisions to move the planets closer together.

## Chapter 3: Perturbed Orbital Elements

In the previous Chapter, we saw that as the two planets got very close to each other (e.g., at the ends of the simulations presented in Figs. 2.5, 2.6, and 2.7), the orbital elements – especially  $e$  – got “fuzzier.” When the planets were far apart, each was essentially a two-body system with Kepler 36. When they got closer, they perturbed the other from its two-body state, and the elements were no longer static. Such fuzziness in the elements is typically not a problem, since perturbations are usually quite weak. In some cases, however, notably when studying ring orbits, the fuzziness becomes a major complication, and we desire an orbit parameterization whose elements do not oscillate as much. We investigate that problem here.

### 3.1 Introduction

#### 3.1.1 The Two-Body Problem

The solution to the two-body problem – that is, determining the motion of two point particles interacting solely via gravity – has been known for centuries. The particles follow static, confocal ellipses, and the common focus lies at their center of mass (e.g., [5]). Their positions and velocities are known at all times. While the true

Universe contains rather more than two point particles, this result is nevertheless useful for predicting the motion of particles in systems dominated by a single body.

Describing a particle’s orbit in the three-dimensional two-body problem requires six linearly independent values; its position and velocity vectors are necessary and sufficient. These values are usually converted into parameters more useful for describing the shape and orientation of the traced ellipse; such parameters are called the orbital elements. Table 3.1 notes some common choices along with their usual symbols, which we shall use for the rest of the chapter.

Orbital Element	Symbol
semimajor axis	$a$
periapse distance	$q$
eccentricity	$e$
inclination	$i$
longitude of ascending node	$\Omega$
argument (longitude) of periapse	$\omega$ ( $\varpi$ )
true (mean) anomaly	$\nu$ ( $M$ )
mean motion	$n$

Table 3.1: Common orbital elements and the symbols we use for them in this chapter.

In the pure two-body problem, all orbital elements (other than the anomaly) are constant; the orbit is static. In reality, however, any perturbations to the two-body approximation likewise perturb the two-body solution. The particles’ orbits – and hence, their orbital elements – then may vary with time. The pure two-body conversions from state vectors to orbital elements produce “osculating” elements: those one would get if the perturbation(s) vanished immediately upon their calculation. The ellipse they describe lies tangent to the true orbit.

In most cases, these elements describe the particle’s orbit well enough that no

further thought need be given to them. However, in some circumstances – such as the cases of a ring particle very near an oblate host, or two planets that perturb each other – the osculating elements vary enough that their utility is diminished. We desire an alternative that minimizes this variance, typically known as “geometric” elements. As noted by [40], the differences between the osculating and geometric elements can be considerable.

### 3.1.2 Epicyclic Elements

[41] considered the case of a ring particle orbiting an oblate planet and derived a fully three-dimensional set of elements, termed the “epicyclic” elements due to their use of the three epicyclic frequencies that describe motion in an oblate potential. They then showed that their epicyclic elements could serve as the sought-after geometric elements for this type of perturbation. However, the epicyclic elements have what appears to be a serious flaw: they do not converge to the two-body solution in the limit that oblateness is turned off, but rather to an expansion of the two-body solution accurate to  $\mathcal{O}(e^2, i^2)$ . This is not an error, but the reason is fairly subtle.

At the heart of the epicyclic element derivation is an expansion in small quantities around a circular, equatorial orbit in a potential corrected for oblateness. [41] derive the first-, second-, and third-order corrections to particle position and velocity in terms of the gravitational spherical harmonic constants  $J_2$ ,  $J_4$ , and  $J_6$  along with the epicyclic  $e$  and  $i$ . The planetary oblateness is accounted for in the zeroth

order solution and is not, therefore, a perturbation. Since the expansion is around circular, equatorial motion, the sources of “perturbation” are actually  $e$  and  $i$ . Since the epicyclic elements are not expansions around the two-body solution, they do not reduce to the two-body solution when the oblateness terms are set to zero.

This choice of expansion is quite natural for studying ring orbits, which are typically very close to circular and equatorial but are heavily perturbed by the host body’s oblateness. However, once  $e$  and/or  $i$  (in radians) grow to be comparable to  $J_2$ , the epicyclic elements are no longer appropriate, and a new set of geometric elements is necessary. To that end, we have produced two sets of alternative elements, which we describe in Section 3.2 below. To simplify our task, we consider only equatorial orbits. We then compare these new sets of elements against the epicyclic elements in Section 3.3 and discuss our results in Section 3.4.

## 3.2 Alternative Choices of Elements

### 3.2.1 Analytic

#### 3.2.1.1 State Vectors to Elements

In this section, we derive analytic corrections to the orbital elements such that the corrected elements reduce to the osculating elements in the absence of any perturbation. We begin with semimajor axis.

The energy  $C$  per unit mass of a particle’s orbit is defined as:

$$C = \frac{1}{2}v^2 + V(r) \quad (3.1)$$

for velocity  $v$ , potential  $V$ , and position  $r$ . Our goal is to get an expression for  $C$  in terms of orbital elements accurate to  $\mathcal{O}(J_2^3, J_2J_4, J_6, J_2e^2)$ , following [41], and use it to derive the various corrections to  $a$ . However, analytically getting  $v^2$  of an elliptical orbit around an oblate planet is difficult, perhaps impossible. Therefore, our strategy is to average Eq. (3.1); the left hand side (LHS) remains unchanged, but the right hand side (RHS) is replaced with averaged quantities:

$$C = \frac{1}{2}\langle v^2 \rangle + \langle V \rangle. \quad (3.2)$$

To  $\mathcal{O}(J_6)$ , the equatorial potential around an oblate planet (via [5]) is:

$$V(r) = -\frac{\mu}{r} \left[ 1 + \frac{1}{2}J_2 \left( \frac{R_p}{r} \right)^2 - \frac{3}{8}J_4 \left( \frac{R_p}{r} \right)^4 + \frac{5}{16}J_6 \left( \frac{R_p}{r} \right)^6 \right] \quad (3.3)$$

Averaging, we get:

$$\langle V \rangle = -\mu \left[ \left\langle \frac{1}{r} \right\rangle + \frac{1}{2}J_2R_p^2 \left\langle \frac{1}{r^3} \right\rangle - \frac{3}{8}J_4R_p^4 \left\langle \frac{1}{r^5} \right\rangle + \frac{5}{16}J_6R_p^6 \left\langle \frac{1}{r^7} \right\rangle \right]. \quad (3.4)$$

We now must derive expressions for each of the four averaged quantities on the RHS of Eq. (3.4). Note that each requires accuracy to a different order in small quantities:  $\langle \frac{1}{r} \rangle$  to third order,  $\langle \frac{1}{r^3} \rangle$  to second order (because it is already being multiplied by  $J_2$ ), etc. Using the expansion for  $r$  to third order in  $e$  in terms of

mean anomaly  $M$  [5]:

$$r = a \left[ 1 - e \cos(M) + \frac{e^2}{2}(1 - \cos(2M)) + \frac{3e^3}{8}(\cos(M) - \cos(3M)) \right], \quad (3.5)$$

and averaging from 0 to  $2\pi$  gives  $\langle \frac{1}{r} \rangle = \frac{1}{a}$ ,  $\langle \frac{1}{r^3} \rangle = \frac{1}{a^3} (1 + \frac{3}{2}e^2)$ ,  $\langle \frac{1}{r^5} \rangle = \frac{1}{a^5}$ , and  $\langle \frac{1}{r^7} \rangle = \frac{1}{a^7}$  to the requisite orders. Substituting into Eq. (3.4) gives:

$$\langle V \rangle = -\frac{\mu}{a} \left[ 1 + \frac{1}{2}J_2 \left( \frac{R_p}{a} \right)^2 \left( 1 + \frac{3}{2}e^2 \right) - \frac{3}{8}J_4 \left( \frac{R_p}{a} \right)^4 + \frac{5}{16}J_6 \left( \frac{R_p}{a} \right)^6 \right]. \quad (3.6)$$

Next, the averaged, squared orbital speed of an object is:

$$\langle v^2 \rangle = \langle \dot{r}^2 \rangle + \langle (r\dot{\nu})^2 \rangle, \quad (3.7)$$

by definition. Differentiating and squaring Eq. (3.5) gives:

$$\dot{r}^2 = (ane)^2 [\sin^2(M) + 2e \sin(M) \sin(2M)] \quad (3.8)$$

to third order in  $e$ , where  $n = \dot{M}$ . Averaging gives:

$$\langle \dot{r}^2 \rangle = \frac{1}{2}(ane)^2. \quad (3.9)$$

Via [5], the expansion for  $\dot{\nu}$  in  $M$  to third order in  $e$  is:

$$\dot{\nu} = n \left[ 1 + 2e \cos(M) + \frac{5}{2}e^2(\cos(2M)) + \frac{e^3}{4}(13 \cos(3M) - \cos(M)) \right]. \quad (3.10)$$

where again  $n = \dot{M}$ . Multiplying Eqs. (3.5) and (3.10), squaring, and averaging, we get:

$$\langle (r\dot{v})^2 \rangle = (an)^2 \left( 1 - \frac{1}{2}e^2 \right). \quad (3.11)$$

Adding Eqs. (3.9) and (3.11) now gives:

$$\langle v^2 \rangle = (an)^2 = \frac{\mu}{a} \left[ 1 + \frac{3}{2}J_2 \left( \frac{R_p}{a} \right)^2 (1 + 4e^2) - \frac{15}{8}J_4 \left( \frac{R_p}{a} \right)^4 + \frac{35}{16}J_6 \left( \frac{R_p}{a} \right)^6 \right] \quad (3.12)$$

where we have used Eq. (A10) from [41] for  $n^2$ . Finally, substituting Eqs. (3.12) and (3.6) into Eq. (3.2) gives:

$$C = -\frac{\mu}{2a} \left[ 1 - \frac{1}{2}J_2 \left( \frac{R_p}{a} \right)^2 + \frac{9}{8}J_4 \left( \frac{R_p}{a} \right)^4 - \frac{25}{16}J_6 \left( \frac{R_p}{a} \right)^6 - \frac{9}{2}J_2 e^2 \left( \frac{R_p}{a} \right)^2 \right], \quad (3.13)$$

We can now derive first-, second-, and third-order corrections to  $a$ . First, by plugging Eqs. (3.3) and (3.13) into Eq. (3.1) and multiplying through by  $-\frac{2}{\mu}$ , we get:

$$\begin{aligned} & -\frac{v^2}{\mu} + \frac{2}{r} + \frac{J_2 R_p^2}{r^3} - \frac{3}{4}J_4 \left( \frac{R_p^4}{r^5} \right) + \frac{5}{8}J_6 \left( \frac{R_p^6}{r^7} \right) \\ & = \frac{1}{a} - \frac{1}{2} \frac{J_2 R_p^2}{a^3} + \frac{9}{8} \frac{J_4 R_p^4}{a^5} - \frac{25}{16} \frac{J_6 R_p^6}{a^7} - \frac{9}{2} \frac{J_2 e^2 R_p^2}{a^3}, \end{aligned} \quad (3.14)$$

Now we expand  $a$  in the small quantity  $\delta$ :

$$a = a_0 \left( 1 + \delta \frac{a_1}{a_0} + \delta^2 \frac{a_2}{a_0} + \delta^3 \frac{a_3}{a_0} \right), \quad (3.15)$$

where  $a_0$  is the osculating  $a$ . Then, we Taylor expand  $\frac{1}{a}$ ,  $\frac{1}{a^3}$ ,  $\frac{1}{a^5}$ , and  $\frac{1}{a^7}$  to the requisite orders:

$$\frac{1}{a} = \frac{1}{a_0} \left[ 1 - \delta \frac{a_1}{a_0} + \delta^2 \left( \left( \frac{a_1}{a_0} \right)^2 - \frac{a_2}{a_0} \right) - \delta^3 \left( \left( \frac{a_1}{a_0} \right)^3 - \frac{2a_1 a_2}{a_0^2} + \frac{a_3}{a_0} \right) \right], \quad (3.16)$$

$$\frac{1}{a^3} = \frac{1}{a_0^3} \left[ 1 - 3\delta \frac{a_1}{a_0} + 3\delta^2 \left( 2 \left( \frac{a_1}{a_0} \right)^2 - \frac{a_2}{a_0} \right) \right], \quad (3.17)$$

$$\frac{1}{a^5} = \frac{1}{a_0^5} \left( 1 - 5\delta \frac{a_1}{a_0} \right), \quad (3.18)$$

and

$$\frac{1}{a^7} = \frac{1}{a_0^7}. \quad (3.19)$$

Using Eqs. (3.15), (3.16), (3.17), (3.18) and (3.19), we can split Eq. (3.14) into four separate equations to determine the zeroth-, first-, second-, and third-order terms:

$$-\frac{v^2}{\mu} + \frac{2}{r} = \frac{1}{a_0} \quad (3.20)$$

$$\frac{J_2 R_p^2}{r^3} = -\delta \frac{a_1}{a_0^2} - \frac{J_2 R_p^2}{2a_0^3} \quad (3.21)$$

$$-\frac{3}{4} J_4 \left( \frac{R_p^4}{r^5} \right) = \delta^2 \left( \frac{a_1^2}{a_0^3} - \frac{a_2}{a_0^2} \right) + \frac{3a_1 \delta J_2 R_p^2}{2a_0^4} + \frac{9}{8} \frac{J_4 R_p^4}{a_0^5} \quad (3.22)$$

$$\begin{aligned} \frac{5}{8} J_6 \left( \frac{R_p^6}{r^7} \right) = & -\delta^3 \left( \frac{a_1^3}{a_0^4} - 2 \frac{a_1 a_2}{a_0^3} + \frac{a_3}{a_0^2} \right) - \frac{3\delta^2 J_2 R_p^2}{2a_0^3} \left( 2 \left( \frac{a_1}{a_0} \right)^2 - \frac{a_2}{a_0} \right) \\ & - \frac{45a_1 \delta J_4 R_p^4}{8a_0^6} - \frac{25}{16} \frac{J_6 R_p^6}{a_0^7} - \frac{9}{2} \frac{J_2 e^2 R_p^2}{a_0^3} \end{aligned} \quad (3.23)$$

Note that summing Eqs. (3.20) through (3.23) recovers Eq. (3.14) and that Eq. (3.20) is the equation for the unperturbed osculating semimajor axis, as expected. Letting  $\alpha_i = J_i \left( \frac{R_p}{a_0} \right)^i$  and  $\beta = \frac{a_0}{r}$  and solving Eq. (3.21) for  $\delta a_1$  gives:

$$\delta \frac{a_1}{a_0} = -\alpha_2 \left( \frac{1}{2} + \beta^3 \right), \quad (3.24)$$

and substituting Eq. (3.24) into Eq. (3.22) and solving for  $\delta^2 a_2$  gives:

$$\delta^2 \frac{a_2}{a_0} = -\frac{1}{2} \alpha_2^2 (1 + \beta^3 - 2\beta^6) + \alpha_4 \left( \frac{9}{8} + \frac{3}{4} \beta^5 \right) \quad (3.25)$$

Finally, plugging Eqs. (3.24) and (3.25) into Eq. (3.23) gives:

$$\begin{aligned} \delta^3 \frac{a_3}{a_0} = & -\alpha_2^3 \left( \frac{7}{8} + \frac{3}{2} \beta^3 + \beta^9 \right) - \alpha_2 \alpha_4 \left( \frac{9}{4} + \frac{63}{8} \beta^3 - \frac{3}{8} \beta^5 + \frac{3}{2} \beta^8 \right) \\ & - \alpha_6 \left( \frac{25}{16} + \frac{5}{8} \beta^7 \right) - \frac{9}{2} \alpha_2 e^2 \end{aligned} \quad (3.26)$$

Plugging Eqs. (3.24), (3.25), and (3.26) into Eq. (3.15), we can now explicitly describe  $a$  to third order:

$$\begin{aligned}
a = a_0 \left[ 1 - \alpha_2 \left( \frac{1}{2} + \beta^3 \right) - \frac{1}{2} \alpha_2^2 (1 + \beta^3 - 2\beta^6) + \alpha_4 \left( \frac{9}{8} + \frac{3}{4} \beta^5 \right) - \alpha_2^3 \left( \frac{7}{8} + \frac{3}{2} \beta^3 + \beta^9 \right) \right. \\
\left. - \alpha_2 \alpha_4 \left( \frac{9}{4} + \frac{63}{8} \beta^3 - \frac{3}{8} \beta^5 + \frac{3}{2} \beta^8 \right) - \alpha_6 \left( \frac{25}{16} + \frac{5}{8} \beta^7 \right) - \frac{9}{2} \alpha_2 e^2 \right]
\end{aligned} \tag{3.27}$$

To get  $e$ , we use the eccentricity vector corrected to  $\mathcal{O}(J_2, J_4, J_6)$  and zeroth order in  $e$ :

$$\mathbf{e} = \frac{1}{k} \mathbf{v} \times \mathbf{h} - \hat{\mathbf{r}}, \tag{3.28}$$

where  $k$  is defined via  $\mathbf{f}(r) = -\frac{k}{r^2} \hat{\mathbf{r}}$  for force per unit mass  $\mathbf{f}$ ,  $\mathbf{v}$  is the velocity vector,  $\mathbf{h}$  is the angular momentum vector, and  $\hat{\mathbf{r}}$  is the position unit vector. Note that if we multiply both sides of Eq. (3.28) by  $k$ , the LHS will remain the same because we are ignoring corrections  $\propto e$ . This gives:

$$\mathbf{e} = \frac{1}{\mu} \mathbf{v} \times \mathbf{h} - \hat{\mathbf{r}} \left[ 1 + \frac{3}{2} J_2 \left( \frac{R_p}{r} \right)^2 - \frac{15}{8} J_4 \left( \frac{R_p}{r} \right)^4 + \frac{35}{16} J_6 \left( \frac{R_p}{r} \right)^6 \right], \tag{3.29}$$

where  $r$  is constant to zeroth order in  $e$ . We now have  $e = \sqrt{e_x^2 + e_y^2 + e_z^2}$  where  $\mathbf{e} = (e_x, e_y, e_z)$ . The eccentricity vector points from apoapse to periapse, so for a two-dimensional orbit,  $\omega$  is now simply given as:

$$\omega = \tan^{-1} \left( \frac{e_y}{e_x} \right) \tag{3.30}$$

To get  $\nu$ , we use the true latitude  $u = \tan^{-1} \left( \frac{y}{x} \right) = \nu + \omega$ :

$$\nu = \tan^{-1} \left( \frac{y}{x} \right) - \omega \quad (3.31)$$

This completes our orbital element set for a two-dimensional orbit.

### 3.2.1.2 Elements to State Vectors

To convert back from geometric elements to state vectors, we first convert to osculating elements, which we will denote with the subscript “0” (i.e.,  $a_0$ ,  $e_0$ , etc.).

First, we calculate  $r$  using geometric elements:

$$r = \frac{a(1 - e^2)}{1 + e \cos \nu} \quad (3.32)$$

Since our geometric elements are approximate,  $r$  will necessarily be approximate as well. However, the equation itself is valid provided we assume the particle follows an ellipse – an assumption without which this entire effort is nonsense anyway.

To get the osculating semimajor axis given  $a$ ,  $e$ , and  $r$ , we numerically solve Eq. (3.27) for  $a_0$ . Starting with the initial guess that  $a_0 = a$ , we calculate the correction to  $a$  (i.e., the bracketed expression on the RHS of Eq. (3.27)), calculate  $a_{0,\text{new}} = \frac{a}{\text{correction}}$ , and then compare  $a_0$  to  $a_{0,\text{new}}$ . If their difference is within an acceptable tolerance (we use  $10^{-14}$ ), we are finished; otherwise, we set  $a_0 = a_{0,\text{new}}$  and repeat the procedure.

To get  $e_0$ , we subtract the osculating eccentricity vector  $\mathbf{e}_0 = \frac{1}{\mu} \mathbf{v} \times \mathbf{h} - \hat{\mathbf{r}}$  from both sides of Eq. (3.29):

$$\mathbf{e} - \mathbf{e}_0 = -\hat{\mathbf{r}}\phi, \quad (3.33)$$

where  $\phi = \frac{3}{2}J_2\left(\frac{R_p}{r}\right)^2 - \frac{15}{8}J_4\left(\frac{R_p}{r}\right)^4 + \frac{35}{16}J_6\left(\frac{R_p}{r}\right)^6$ . For a two-dimensional orbit, this yields two equations:

$$e_x - e_{x,0} = -\frac{x}{r}\phi \quad (3.34)$$

and

$$e_y - e_{y,0} = -\frac{y}{r}\phi \quad (3.35)$$

By definition, we have  $\frac{x}{r} = \cos u$  and  $\frac{y}{r} = \sin u$  for true latitude  $u = \omega + \nu$ . In addition, we have  $e_x = e \cos \omega$  and  $e_y = e \sin \omega$ . Substituting these expressions into Eqs. (3.34) and (3.35) gives:

$$e_{x,0} = e \cos \omega + \phi \cos(u) \quad (3.36)$$

and

$$e_{y,0} = e \sin \omega + \phi \sin(u) \quad (3.37)$$

We can now use Eqs. (3.36) and (3.37) to get  $e_0$  and  $\omega_0$  via:

$$e_0 = \sqrt{e_{x,0}^2 + e_{y,0}^2}, \quad (3.38)$$

$$\omega_0 = \tan^{-1} \left( \frac{e_{y,0}}{e_{x,0}} \right), \quad (3.39)$$

and

$$\nu_0 = u - \omega_0. \quad (3.40)$$

Note that Eq. (3.40) implies that  $u = \omega_0 + \nu_0 = \omega + \nu$ . This is justified since we do not distinguish between an osculating and geometric  $u$ : both are defined via  $u = \tan^{-1} \left( \frac{y}{x} \right)$  (see Eq. (3.31)).

This inverse conversion to osculating elements from geometric ones is not perfect because it relies on an approximate value of  $r$ . Nevertheless, we can now get state vectors from osculating elements using standard conversions found in, e.g., [5].

### 3.2.2 Numerical

In this section, we get the orbital elements numerically. We use a least-squares routine to fit sets of  $N$  positions to a rotated, off-center ellipse. Note that given  $M$  independent positions, we will only obtain  $M - N$  orbital element sets, and the time assignment to each will be ambiguous: an unavoidable weakness of this approach.

The normalized equation <sup>1</sup> of a rotated, off-center ellipse with semimajor axis  $a$  and center point  $(x_0, y_0)$  is :

---

<sup>1</sup>This is one of infinitely many, equally valid normalizations.

$$Ax^2 + Bxy + Cy^2 + Dx + Ey = 1, \quad (3.41)$$

where  $A$ ,  $B$ ,  $C$ ,  $D$ , and  $E$  are independent parameters. For this choice of normalization,  $a^2$ ,  $x_0$ , and  $y_0$  are given by:

$$a^2 = 2 \frac{AE^2 + CD^2 - BDE - B^2 + 4AC}{(B^2 - 4AC)^2} \left( A + C + \sqrt{(A - C)^2 + B^2} \right) \quad (3.42)$$

$$x_0 = \frac{2CD - BE}{B^2 - 4AC} \quad (3.43)$$

$$y_0 = \frac{2AE - BD}{B^2 - 4AC} \quad (3.44)$$

We can use these to write down expressions for  $e$  and  $\omega$ . Note that the vector  $\mathbf{c} = x_0 \hat{\mathbf{x}} + y_0 \hat{\mathbf{y}}$  points from periapse to apoapse (given barycentric state vectors) and has magnitude  $ae$ . Thus, we have:

$$e^2 = \frac{x_0^2 + y_0^2}{a^2} \quad (3.45)$$

$$\omega = \tan^{-1} \left( \frac{-y_0}{-x_0} \right) \quad (3.46)$$

We can also calculate true latitude  $u = \omega + \nu$  and hence  $\nu$ :

$$u = \tan^{-1} \left( \frac{y'(t_c)}{x'(t_c)} \right) \quad (3.47)$$

$$\nu = u - \omega \quad (3.48)$$

Unfortunately, the choice of  $t_c$  here is ambiguous; given  $N$  positions uniformly distributed between times  $t_0$  and  $t_f$ , we typically choose  $t_c = \frac{t_0+t_f}{2}$ , i.e., the “middle” time. (Note that choosing  $N$  odd guarantees that  $t_c$  will always correspond to a printed time for a fixed output interval, and vice versa for  $N$  even.) Nevertheless,  $a$ ,  $e$ ,  $\omega$ , and  $\nu$  produce the desired orbital element set.

How many points should we use per fit? This turns out to be a rather complex question. To keep  $M - N$  high, we would like  $N$  to be as low as possible, all else being equal. However, we might expect that with greater  $N$  comes lower fit errors; our task is thus to balance these competing motives. To find such an  $N$  empirically, we generated  $(x, y)$  data sets for several 2D rotating ellipses of constant  $a$  and  $e$ , used our fitting algorithm to produce orbital element sets of these data, and calculated the mean errors of the fitted  $a$  and  $e$ . Using these “fake” orbits over simulated orbits guaranteed that we knew precisely what the true orbital elements were at all times, greatly simplifying the task of evaluating how successful the fits were. Unfortunately, the errors on  $a$  and  $e$  are complicated functions of  $N$ ,  $\dot{\omega}$ ,  $e$ , and the number of number of points printed per orbit  $\gamma$ . We show a typical example of these errors in Fig. (3.1).

A few patterns are apparent in Fig. (3.1). First, the error for both  $a$  and  $e$

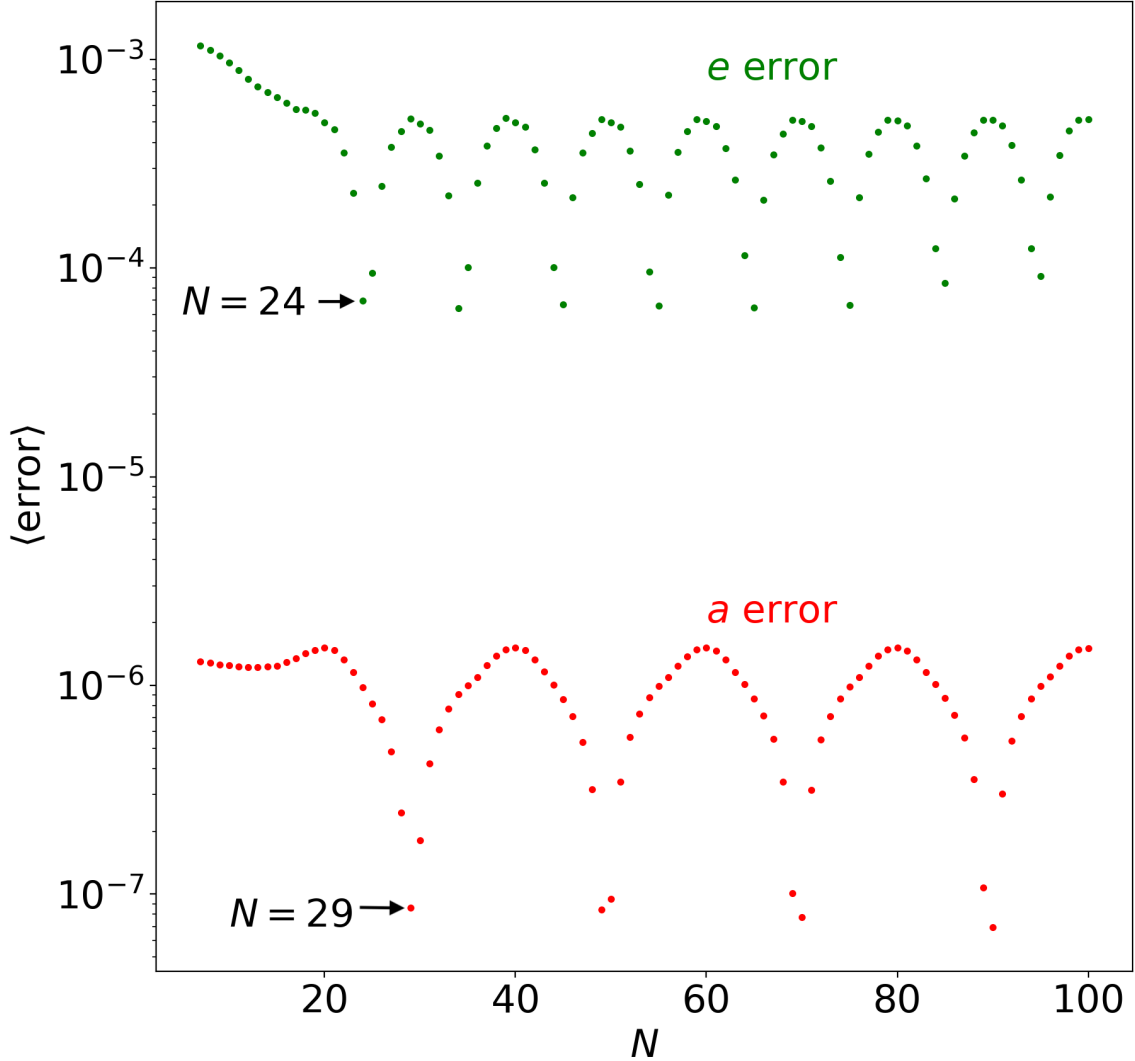


Figure 3.1: Typical average eccentricity  $e$  error (green) and semimajor axis  $a$  error (red) versus number of points  $N$  from our numerical fit using  $\gamma = 20$ , i.e., in which we print twenty times per orbit. We have normalized the error by the true quantity; that is, we define the error in a quantity  $x$  as  $\frac{|x_{\text{true}} - x_{\text{calc}}|}{x_{\text{calc}}}$ , where  $x_{\text{true}}$  is the true value of  $x$  and  $x_{\text{calc}}$  is the calculated value. Ellipse parameters were  $a = 1$  and  $e = 0.001$ ; we rotated the periapse point 0.01 radians counter-clockwise each output. We have marked the  $N$  corresponding to the first dip for both sets of errors.

always stays high until  $N \approx \gamma$ , at which point they oscillate over roughly a factor of ten around a constant value. Unfortunately, the errors on  $a$  and  $e$  often have notably different periods, and even when they are similar, they are often out of phase. This means there is usually not one single  $N$  that minimizes the errors for all elements.

We have marked the optimal  $N$  for minimizing both  $e$  and  $a$  errors. In the case of the generated rotating ellipses, the errors are quite small, even for very low  $N$ , but the differences in fits from different  $N$ s can be considerable when fitting data simulated with a more sophisticated integrator.

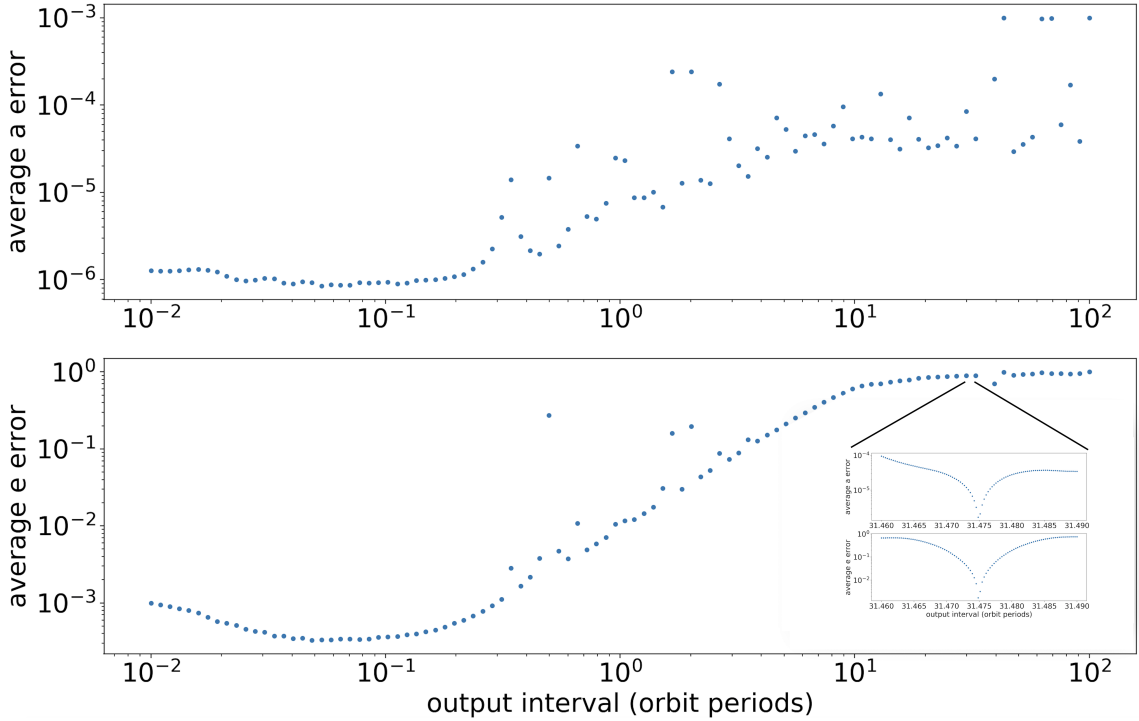


Figure 3.2: Doubly averaged errors on  $a$  and  $e$  versus output interval (i.e.,  $\frac{1}{\gamma}$ ). Whereas in Fig. (3.1), each plotted point was the average error over a simulation, here the point at output interval =  $\frac{1}{20} = 0.05$  in the top panel is the average of all red points from  $N = 30$  to  $70$  in Fig. (3.1); likewise for the bottom panel and green points. The other points in each panel are similar averages for different choices of output interval. All simulations were again performed using  $a = 1$  and  $e = 0.001$  with periaapse rotation of  $0.01$  rad per output. The inset in the bottom panel zooms in on the output interval from  $31.46$  to  $31.49$ , showing the large dip in errors there; this is discussed further in the text.

In Fig. (3.1), we print every “time step”. To obtain similarly low errors for real simulations, one would have to modify how their simulation printed; instead of printing a single state vector per output, one would have to print roughly a full orbit’s worth, increasing the size of their output file by a factor of  $\gamma$ . In general,

there is no avoiding this. Even absent any secular changes to  $a$  or  $e$ , if the orbit nontrivially precesses between each output, the printed positions will be randomly distributed between the periapse and apoapse distances in time; fitting them to an ellipse will simply produce a circle of radius  $\sim a$ . We show this in Fig. (3.2).

Interestingly, there *are* certain output intervals for which the error dips by several orders of magnitude, as we have showed in the inset in the bottom panel of Fig. (3.2). Such intervals are integer multiples of the precession period; at these intervals, the ellipse has precessed exactly  $2\pi$  radians and returned to its original orientation, so all printed points effectively lie on the same ellipse. Of course, printing at these intervals requires very precise knowledge of the precession frequency, ruins the  $\omega$  and  $\nu$  calculations, and is in any case invalid for non-periodic changes to the elements. This is therefore more a mathematical curiosity than a reliable method of ensuring low errors for long output intervals.

### 3.3 Comparisons

In this section, we compare our two schemes to the epicyclic elements of [41] by simulating orbits around Earth, Uranus, and Saturn (see Table 3.2). In all cases, we integrate a test particle ( $m = 10^{-20}$  host masses) for ten equatorial orbits using the symplectic integrator option of HNBODY [14]. We print state vectors twenty times per orbit; for our numerical elements, we always use  $N = 29$ . To maximize the perturbations, we set the geometric periapse distance equal to the host radius. All integrations begin at  $\mathbf{r} = (1, 0, 0)$  and  $\mathbf{v} = (0, v_{\text{circ}} + \delta v, 0)$  for circular speed  $v_{\text{circ}}$

and small speed  $\delta v$ . We tested  $e \approx 10J_2$ ,  $e \approx J_2$ , and  $e \approx 0.1J_2$  for each planet and empirically determined which values of  $\delta v$  corresponded to the desired eccentricities.

Planet	$J_2 (\times 10^{-7})$	$J_4 (\times 10^{-7})$	$J_6 (\times 10^{-7})$
Earth	10826.35854	-16.19331205	5.396484906
Uranus	33412.9	-310	0
Saturn	162905.73	-9353.1	863.4

Table 3.2: Estimates of  $J_2$ ,  $J_4$ , and  $J_6$  for Earth, Uranus, and Saturn. Earth values taken from [42] and Saturn values taken from [43]. Uranus  $J_2$  value taken from [44]; we estimate its  $J_4$  value using  $-\frac{J_4}{J_2} = 0.0092$  (see their Table 2). We were unable to find a  $J_6$  estimate for Uranus and have set it to 0.

We evaluate our elements based on how tightly they librate around  $q = 1$ . Of course, none of our schemes calculates  $q$  directly, so  $a$  and  $e$  could both be wrong but produce the correct  $q$  by chance. We therefore cannot be truly certain which set of elements is “best” except in the case of a circle. We guard against this degeneracy simply by checking that the elements from each algorithm all cluster near each other; since they are independent calculations, they are unlikely to all have same wrong values. We show one example of a Saturn orbit in Fig. (3.3) with  $J_2 \gg e$ , characteristic of close-in ring orbits.

All three sets have low  $a$  amplitude, although the  $a$  averages differ. By contrast, the  $e$  averages are quite similar, although the epicyclic and analytic elements have a higher amplitude. As a result, the numerical elements have the lowest  $q$  amplitude, and their average  $q$  error is closest to 0. We therefore consider the fitted elements to have performed the best in this case. While the analytic and epicyclic  $e$  curves are quite similar, the greater analytic  $a$  brings its average  $q$  error closer to 0 with a comparable libration amplitude to the epicyclic elements; we therefore deem

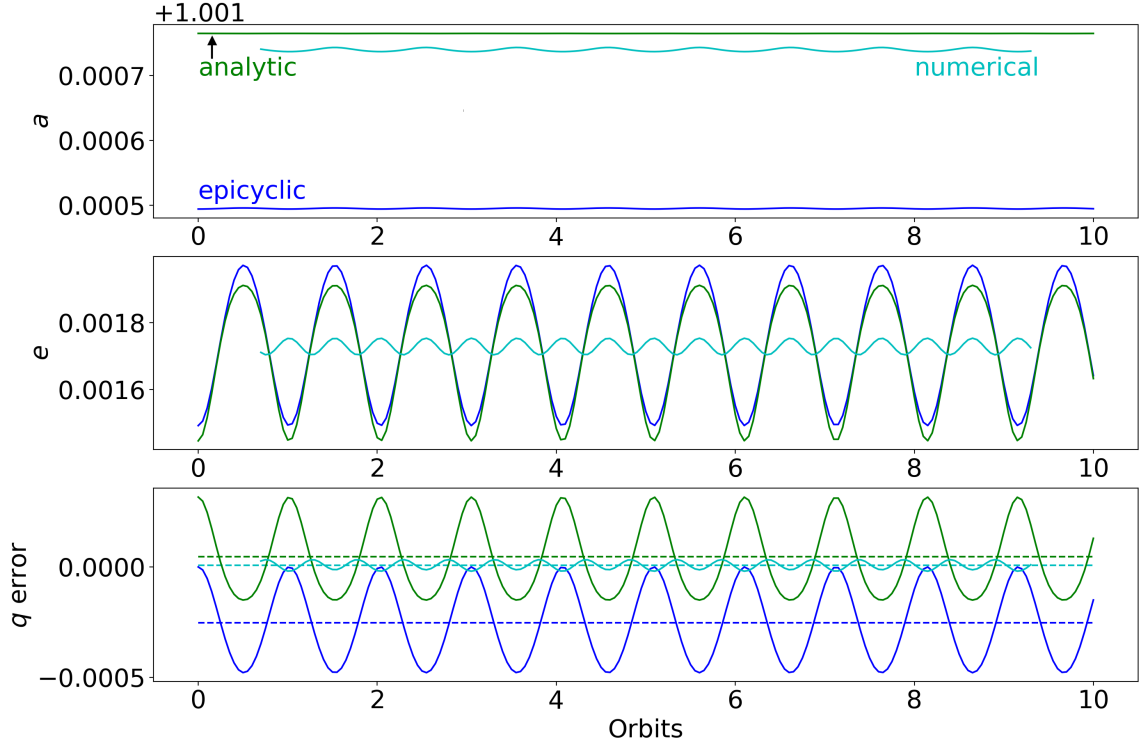


Figure 3.3: The geometric  $a$  (top) and  $e$  (middle), and  $q$  error (bottom) for ten orbits of a test particle around Saturn. The dark blue curve is the epicyclic elements, the cyan curve is the fitted numerical elements, and the green curve is the analytic elements. The dotted lines in the bottom plot are the average  $q$  error values. The numerical elements appear to perform best; their average  $q$  error is closest to 0, and the libration amplitude for both  $q$  error and  $e$  is lower than that of the other two sets.

the analytic elements to be “second best.”

We repeated this exercise for our three  $e$  regimes at each planet and summarize our results in Fig. (3.4).

A few patterns are apparent. First, errors are roughly proportional to the strength of the perturbation, as expected. The perturbation strength appears to affect the numerical elements considerably more than the others; a factor of ten increase in  $J_2$  increases the errors in the epicyclic and analytic elements by about a factor of  $\sim 10$  to 100, whereas the errors in the numerical elements increase by a factor of  $\sim 1,000$  to 10,000 depending on  $e$ . However, the numerical elements

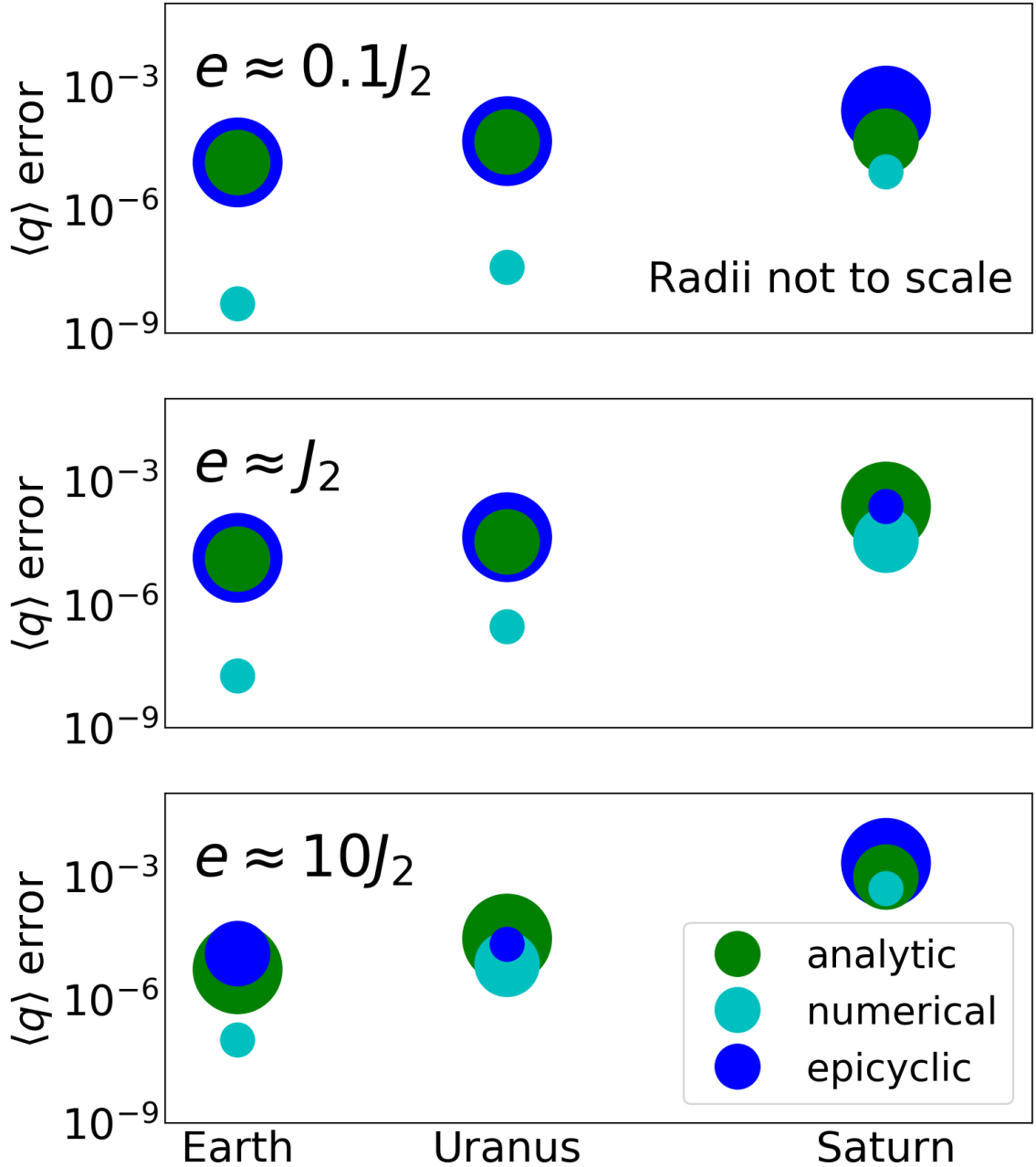


Figure 3.4: Average  $q$  error of analytic (green), numerical/fitted (cyan), and epicyclic (blue) elements. The sizes of the circles signify the relative  $q$  amplitudes but are NOT to scale. We show results for  $e \approx 0.1J_2$  (top panel),  $e \approx J_2$  (middle panel), and  $e \approx 10J_2$  (bottom panel). Results for Earth, Uranus, and Saturn are displayed in the left, middle, and right columns, respectively. The simulation from Fig. (3.3) is summarized in the top panel’s Saturn column. We logarithmically space the columns according to the planetary  $J_2$ . The fitted elements always have the lowest error and have the lowest amplitude in every case except at Uranus with  $e \approx 10J_2$  and at Saturn with  $e \approx J_2$ .

always have a lower error than the others and usually have a lower amplitude as well, particularly when  $e \approx 0.1J_2$ . In addition, the analytic and epicyclic elements typically have similar errors; the most notable difference is shown in Fig. (3.3).

## 3.4 Conclusions

### 3.4.1 Summary

We have debuted two new sets of geometric orbital elements for two-dimensional orbits alongside the epicyclic elements of [41]. The first is analytic, in which we derive corrections to the osculating elements from first principles using a corrected potential. The second is numerical, in which we simply fit sets of points to an ellipse. The epicyclic elements account for three-dimensional orbits, whereas the other two sets do not. However, by design, the epicyclic elements do not smoothly reduce to the osculating solution in the limit of a spherical host, and our testing shows that they often do not perform as well as the other elements for two-dimensional orbits.

The analytic elements are the opposite – they do not account for three-dimensional orbits, but do correctly reduce to the osculating solution and appear to be about as accurate as the epicyclic elements. Finally, the numerical elements appear to be more accurate than either of the other two sets for two-dimensional orbits and can also be easily adapted to a general perturbation, rather than just those from host oblateness. However, by design they always produce fewer elements sets than the number of state vectors and require modifying how the simulation prints data; instead of a single state vector per output, the numerical elements require

tens.

### 3.4.2 Future Work

We have only considered equatorial orbits here; this is a clear problem. For three-dimensional orbits around an oblate host, the potential varies azimuthally and so the force is not conservative. This means we would have to rethink our analytic approach, which relied on conservation of energy and of the magnitude of the eccentricity vector. For the numerical approach, we could start by simply calculating the osculating  $i$  and  $\Omega$  and rotating all points into a single plane, but this would by definition destroy any three-dimensional information. There is no obvious path forward for either approach.

One alternative method of calculating the elements (Matt Tiscareno, private communication) could be to determine the periaipse and apoapse distances  $q$  and  $Q$  numerically by interpolating between the farthest and closest points within a defined time interval, which would yield  $a$  and  $e$ , then calculate the other elements analytically using the corrected ellipse shape. For two-dimensional orbits, such a hybrid approach could work well; in the case of an ellipse whose  $a$  and  $e$  do not change secularly, one could simply pick the two points with the greatest and least  $|\mathbf{r}|$  out of all printed positions. For  $N$  points uniformly distributed in time on a circular orbit, we expect the average angular distance from one point to the next to be  $\frac{2\pi}{N}$ . The maximum angular error between  $\mathbf{r}_{\mathbf{q},\text{est}}$  and the true periaipse vector  $\mathbf{r}_{\mathbf{q},\text{true}}$  is then  $\epsilon = \frac{\pi}{N}$ . Thus, to first order in  $e$ , we have:

$$\frac{|\mathbf{r}_{\mathbf{q},\text{est}}|}{|\mathbf{r}_{\mathbf{q},\text{true}}|} = \frac{1 - e \cos(\epsilon)}{1 - e} \approx 1 + \frac{1}{2}e\epsilon^2, \quad (3.49)$$

The maximum error on  $q$  is therefore  $\mathcal{O}(e\epsilon^2)$ ; one can perform a similar analysis for  $Q$ . For large  $N$ , this could be a very computationally inexpensive way of getting  $a$  and  $e$  with tolerably low error. Furthermore, this would also work for three-dimensional orbits, although there is still no obvious path to getting  $i$  and  $\Omega$  without angular momentum conservation.

## Chapter 4: Self-Confining Narrow Eccentric Rings

The three outermost planets, as well as several small bodies, host very narrow, eccentric rings that are expected to spread on near-human timescales. Unless we are observing at an extraordinarily coincidental time, some mechanism must confine them, but the leading confinement theory can only explain one, possibly two, of the dozens of known cases. We present our own theory and test it with a specialized N-body integrator designed for ring simulations that uses the epicyclic elements from the previous Chapter.

### 4.1 Introduction

#### 4.1.1 Observations of Narrow Rings

Narrow ringlets are plentiful in the Solar System, encircling Saturn, Uranus, Neptune, and even some small bodies. Important parameters for specific ringlets are given in Table 4.1. Saturn's rings, of course, have been known to exist at least since the time of Galileo. Modern exploration has included four spacecraft: Pioneer 11, Voyager 1 and 2, and most recently, Cassini. At Saturn, Pioneer 11 discovered Saturn's F ring in 1979 [45], while Voyager 2 observed variable ringlet structures

Host Planet	Name	$e \times 10^{-4}$	Width (km)	Radius (km)	Radius ( $R_p$ )	$a \frac{de}{da}$
Neptune	Adams	$4.7 \pm 0.2$	15-50	62,932	2.5559	–
Uranus	$\epsilon$	79.4	19.8-96.3	51,188	2.0182	0.65
Uranus	$\alpha$	7.8	4.9-10.1	44,758	1.7648	0.27
Uranus	$\beta$	4.3	5.0-10.6	45,701	1.8019	0.45
Saturn	Titan	2.6	13-37	77,871	1.3373	0.44
Saturn	Maxwell	3.4	40-88	87,491	1.5025	0.46

Table 4.1: Eccentricity  $e$ , width, and radius, and eccentricity gradient  $a \frac{de}{da}$  for selected ringlets. All data for Uranian and Saturnian ringlets taken from [5] via [51]. Data for Adams ringlet taken from [52] (width), [53] (width), and [54] (eccentricity). Eccentricity gradients taken from [3].

[46]; [47] suggested that Saturn’s magnetic field could be partially responsible for the formation of the inner ringlets. There are also narrow, eccentric rings in gaps in the C ring as well as the Cassini division [48]. Observations by the Cassini spacecraft have yielded hundreds of papers since its arrival at Saturn in 2004.<sup>3</sup> [49] and [50] provide a large survey of observations made of the edge of Saturn’s B ring as well as the C ring.

The rings of Uranus and Neptune, which have only been visited by the Voyager 2 spacecraft, have a much briefer observing history; most of them were discovered via stellar occultation. With this method, the observer sees the light from a background star briefly fade when the planet is close to (but not precisely aligned with) the line of sight to the star and deduces that a ring is the likely culprit. Occasionally, however, a moon can also be responsible [52].

The first detection of rings orbiting Uranus was made by [55], who discovered the  $\alpha$ - $\epsilon$  rings around Uranus via stellar occultation measurements. Further observations were made by [56] and [57], who discovered four more rings, again via

<sup>3</sup> See <http://saturn.jpl.nasa.gov/science/index.cfm?Science\PageID=86> for a list of papers produced by members of the Cassini team.

occultation. [58] and [59] reported on further occultation measurements, and [60] provided updated profiles on all nine known rings. Voyager 2 directly imaged the Uranian rings for the first time in 1986 and discovered two more [61]. [62] finally discovered the last two currently known rings, along with two additional moons, with deep Hubble Space Telescope exposures.

The rings of Neptune were harder to detect; [63], [64], [65], and [66] all did not find evidence for them. It was not until [67] and [68] that they were discovered via occultation. [67] noticed that the structure they discovered was not a complete ring and described it as an “arc” instead; Neptune is currently the only known body to host such prominent arcs. [69] reported on their stellar occultation observations of Neptune’s rings from 1983 - 1989 and compared their observations to those made by Voyager 2, particularly regarding observations made of the so-called Liberty, Equality, and Fraternity arcs. [70] reported further observations of Neptune’s ring arcs along with the satellite Galatea and showed that Galatea was unlikely to be solely responsible for their confinement.

Narrow rings have more recently been discovered around Centaurs, small bodies orbiting the Sun between Jupiter and Neptune. In particular, both 10199 Chariklo [71] and 2060 Chiron [72] are suspected to host ringlets. In addition, [73] determined that the trans-Neptunian dwarf planet Haumea also hosts narrow rings. The ability of these ubiquitous structures to exist around such a huge range of bodies – Chariklo has an equivalent radius of  $124 \pm 9$  km [71] – poses a unique challenge to attempts to model their evolution and origins.

Due to the high surface mass densities of narrow ringlets, simple estimates

predict radial spreading on very rapid timescales – tens to thousands of years – due to internal collisions that transfer angular momentum but dissipate energy [74]. Their mere existence, however, argues that they either formed very recently (implying we are observing at a privileged time) or spread on far slower timescales than expected. As the former option is highly unlikely, serious attempts have been made to explain why these ringlets have not spread as quickly as one might initially expect.

#### 4.1.2 Shepherd Satellites

Most models attempt to prevent or slow ringlet spreading by increasing the system’s energy via the presence of nearby “shepherding satellites” [75, 76, 77, 78, 79, 80, 81, 82]. Eccentric rings should precess differentially due to the oblateness of the host planet; the inner parts of the ring feel a stronger force from the planet’s equatorial bulge and therefore precess faster than the outer parts. However, if the ring is sufficiently massive, self-gravity can maintain rigid precession, in which the entire ring precesses at the same rate [75]. At periaapse, where ringlets are observed to be narrowest and self-gravity is thus strongest, inner material pulling on outer material can generate differential precession offsetting that due to the planet’s oblateness. Such “cancellation” of these two effects is required for a ring to stay in a stable equilibrium [3], which features approximate periaapse alignment throughout – this is equivalent to rigid precession. However, differential rotation between inner and outer parts of the ring still leads to particle collisions and hence energy dissipation [81].

In the shepherd satellite scenario, energy lost to collisions is restored to the system by gravitational interaction with satellites, allowing a long-term steady state to develop that keeps the ring confined. As long as the shepherds remain in place, the energy of the ring remains constant, equilibrium is maintained, and the ring survives over timescales comparable to the age of the satellites. This theory had two early successes: Uranus'  $\epsilon$  ring, thought to be shepherded by the nearby moons Cordelia and Ophelia, and Saturn's F ring alongside the moons Prometheus and Pandora (although this latter view has recently been questioned [83]). Less promising, however, are the many additional narrow ringlets without observed attendant satellites. A Cassini search of eleven gaps in Saturn's rings for sufficiently large shepherding moons found none; the likelihood of this happening by chance was  $\sim 0.002\%$  [84]. The suggestion that there must be dozens of unseen tiny moonlets therefore strains credibility enough to justify seeking an alternative explanation.

### 4.1.3 Our Model - An Internal Energy Source

We suggest rings can self-confine by tapping an internal energy source to balance the dissipation of energy. As with any two bodies, when ring particles collide, energy is lost as heat due to friction, internal cracking, etc. However, angular momentum is still conserved because there is no external torque on the ring. Energy dissipation determines the amount of spreading: how much fractional energy loss  $\frac{dE}{E}$  is necessary to spread a ring of mass  $m_r$  and semimajor axis  $a$  by a width  $2\Delta a$  in the circular case? If the initial width is 0, then the initial energy  $E_0$  is the standard:

$$E_0 = -\frac{GMm_r}{2a}, \quad (4.1)$$

where  $M$  is the mass of the host. In the limit that all of the ring mass is evenly distributed at the edges as it spreads (effectively splitting the ring in two), the energy of a ring of width  $2\Delta a$  is:

$$E_f = -\frac{GMm_r}{4} \left( \frac{1}{a + \Delta a} + \frac{1}{a - \Delta a} \right) \quad (4.2)$$

This gives:

$$\frac{dE}{E} = \frac{E_f - E_0}{E_0} \approx -\left(\frac{\Delta a}{a}\right)^2 \quad (4.3)$$

for semimajor axis  $a$  and energy  $E$ . For  $2\Delta a = 2$  km and  $a = 50,000$  km (a typical semimajor axis for a narrow ringlet; see Table 4.1) this gives  $\frac{dE}{E} \approx -4 \times 10^{-10}$ . Even losing a small fraction of energy can cause a circular ring to spread 2 km, leading to a very short spreading timescale.

A width change for an eccentric ring gives a similar expression. Typical ringlet eccentricities are very small (see Table 4.1), and in the limit that  $e$  goes to 0, the expression for energy dissipation in the eccentric case reduces to that for the circular case by continuity. However, when the ring's eccentricity is not held constant, this argument no longer holds. As we discuss below, permitting eccentricity to change significantly affects energy dissipation.

For an eccentric ringlet of eccentricity  $e$ , the angular momentum  $L$  is:

$$L^2 = GMm_r a (1 - e^2). \quad (4.4)$$

If the ring can arrange itself such that  $a$  and  $e$  simultaneously decrease, then the angular momentum can be preserved while energy dissipates. This is possible only for the eccentric case because of the extra degree of freedom afforded by the  $(1 - e^2)$  term in Eq. (4.4).

For this confinement scheme to be plausible, we must address two questions. First, how might a ring arrange itself in this manner? Second, assuming that such an arrangement is possible, how would it affect the spreading timescale? We address the second question first.

For an eccentric ring, we can calculate the energy loss due to a decrease in eccentricity. Combining Eqs. (4.1) and (4.4) gives:

$$\begin{aligned} E &= -\frac{GMm_r}{2 \left[ \frac{L^2}{GMm_r(1-e^2)} \right]^{1/2}} = -\frac{(GMm_r)^{3/2}}{2L} (1 - e^2)^{1/2} \\ &\approx -\frac{(GMm_r)^{3/2}}{2L} \left( 1 - \frac{e^2}{2} \right) \end{aligned} \quad (4.5)$$

From Eq. (4.5), we see that  $E$  increases roughly by  $e^2$ , so for a ring with  $e \sim 0.01$ ,  $\frac{dE}{E} \sim 10^{-4}$ . The energy loss associated with circularization therefore dominates that associated with spreading. Such an eccentric ring can live  $\sim 100,000$  times as long as a circular ring. Thus, assuming that some mechanism can confine rings, this model naturally explains their longevity. Given this promising development, we now

return to the first question posed above and seek a means to prevent spreading.

#### 4.1.4 Self-Confinement

For a ring to stay confined, it must satisfy three criteria: the periapses of its particles' orbits must stay aligned, the eccentricity must decrease slowly in unison, and  $\frac{da}{dt}$  must also be constant with distance across the ring. We address the first two criteria by invoking the concept of a secular mode. For a physical ring, a secular mode is a particle arrangement such that the orbits of particles precess together at a constant rate, their eccentricities keep a fixed ratio, and their apses are either perfectly aligned or anti-aligned [85]. [85] additionally report that planetary systems (which are fully analogous to our ring systems) preferentially settle into such a mode when dissipation is active. Thus, a ring in an aligned secular mode already satisfies the first two criteria above.

To ensure that  $\frac{da}{dt}$  does not change throughout the ring, we invoke collisions that remove energy from the innermost section of the ringlet, moving it inward and creating a gap between it and the rest of the ring (see top left and top right frames in Fig. 4.1). This section now differentially precesses (bottom right frame), “twisting” the ring (bottom left frame – the periapse of the innermost section is noticeably unaligned with the rest of the ring). While the ring is twisted, there is a new point of closest approach between the innermost section and the rest of the ring. This provides the internal energy source — at this point, the main ring particles are moving faster than those in the innermost section. As a result of this unusual

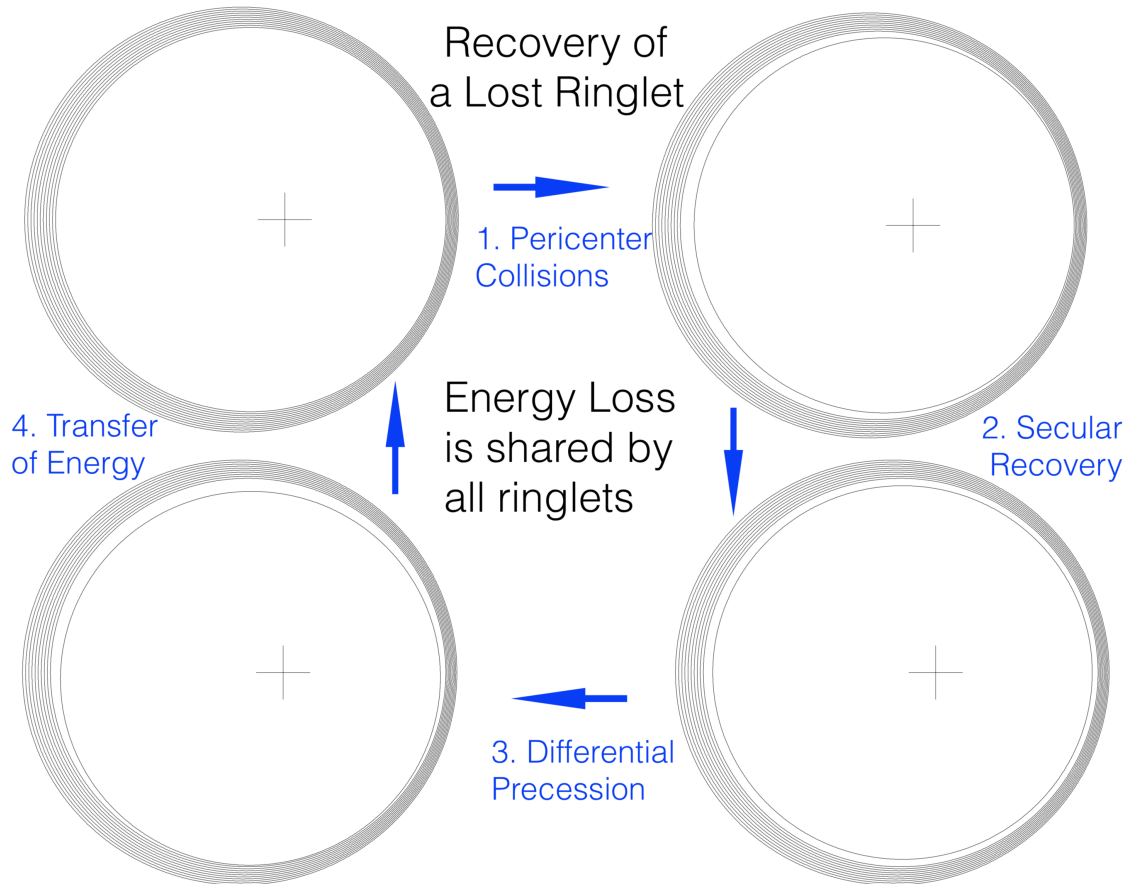


Figure 4.1: Schematic showing the energy cycle of a non-spreading ringlet. In the top left diagram (1), pericenter collisions kick the innermost ringlet further inwards. In (2) and (3), this ringlet then begins to circularize and differentially precess until the point of closest approach between the ringlet and the rest of the ring is close enough to begin transferring energy in (4). This leads the ring back to its initial configuration with a slightly lower eccentricity.

orientation, energy gets transferred from the main ring, which moves very slightly inwards but does not spread, and the innermost section returns to its nearly original configuration. Thus,  $\frac{da}{dt}$  is constant everywhere averaged over long timescales, and our model can explain both the confinement and the long lifespan of narrow eccentric rings.

[76] and [3] also discuss the effects of a twist, which they call an “apsidal shift.”

They define a parameter  $q$  such that:

$$q^2 = \left( a \frac{de}{da} \right)^2 + \left( ae \frac{d\Delta}{da} \right)^2, \quad (4.6)$$

where  $a$  is the semimajor axis,  $e$  is the eccentricity, and  $\Delta$  is the pericenter phase lag, assuming the ring follows a Keplerian ellipse. In Eq. (4.6),  $a \frac{de}{da}$  is referred to as the “eccentricity gradient” of the ring, and  $\frac{d\Delta}{da}$  is the twist. For a nearly circular ring, the first term dominates, but for a moderately eccentric ring with a large twist, the second term can be significant. For  $q \geq q_{crit} \equiv \frac{\sqrt{3}}{2}$ , the ring can stay confined [76]. In Table 4.1, we have included  $a \frac{de}{da}$  values for selected ringlets orbiting Uranus and Saturn.

## 4.2 Ring Integration with epi\_int

To test our model, we used epi\_int, an N-body leapfrog integrator with several features more commonly associated with hydrodynamic codes [4]. Epi\_int uses epicyclic elements (see Chapter 2) rather than the more familiar Keplerian elements to update the particle positions during the drift step. The key difference between

the two is that epicyclic elements account for the effects of planetary oblateness whereas Keplerian elements do not. The distinction is important for this problem because we are interested in the effects of weak, secular forces, but these effects are dominated by oblateness and would be difficult to observe using Keplerian elements, which are designed for the pure two-body problem. The choice of epicyclic elements sidesteps this problem; rather than treat the effects of oblateness as a separate force in the kick step, they are neatly accounted for instead in the drift step, preventing the weak but important secular effects from getting “washed out.”

`Epi_int` simulates a ring by dividing it into  $N$  streamlines of  $M$  particles each; the user sets  $N$  and  $M$  [4]. This is a common abstraction [3, 76], meaning that `epi_int` can be easily compared to theoretical results. Vertical forces are not considered – since rings are highly equatorial, simulations in all three spatial dimensions would likely produce very similar results at the expense of considerably more computational time. The user can control a number of forces, both internal and external. Both self-gravity and viscosity are present in and important to the evolution of narrow rings, so we briefly describe their implementations here.

#### 4.2.1 Self-Gravity

Ring simulation is difficult in general – there are often far too many particles to attempt a standard N-body integration. One solution is to simplify the problem by studying only a small patch of a ring (e.g., [86]), but this strategy is unsuitable for studying ring confinement. `Epi_int` approximates ring self-gravity by considering

two sources of internal gravitational acceleration – that from nearby sections of other streamlines, and that from particles within the same streamline.

To calculate the acceleration on a single particle from other streamlines, the code approximates them as infinitely long, straight wires. Each streamline is assigned a linear density  $\lambda \sim \frac{M}{2\pi a}$ , where  $M$  is the streamline mass and  $a$  is its semi-major axis, assuming eccentricity  $e \ll 1$ . The gravitational acceleration  $a_g$  of the streamline on the particle is then given as [4]:

$$a_g = \frac{2G\lambda}{\Delta}, \quad (4.7)$$

where  $\Delta$  is the distance to the nearest part of the streamline. To approximate  $\Delta$  to a perturbing streamline, `epi.int` identifies its three closest particles and fits a parabola to them. This parabola is then used to extrapolate  $\Delta$ .

To calculate the net acceleration on the perturbed particle from those in the same streamline, `epi.int` approximates this particle as sitting in a gap that extends midway to its neighbors, which dominate the net gravitational force. Since the streamline is very close to a straight line near the particle of interest, `epi.int` approximates this force by treating the ring as an infinite line of density  $\lambda$  and removing a segment of length  $d = \frac{\Delta_+}{2} + \frac{\Delta_-}{2}$ , where  $\Delta_+$  and  $\Delta_-$  are the distances to the nearest neighbors in the leading (+) and trailing (−) directions. The net gravitational acceleration from nearby particles within the same streamline is then given as:

$$A_g = a_+ + a_- = 2G\lambda \left( \frac{1}{\Delta_+} - \frac{1}{\Delta_-} \right), \quad (4.8)$$

where  $a_+$  ( $a_-$ ) is the leading (trailing) acceleration [4]. This can be derived by considering the integral  $\int_{\frac{\Delta_+}{2}}^{\infty} \frac{GdM}{r^2}$ , where  $dM = \lambda dr$ . This integral evaluates to  $\frac{2G\lambda}{\Delta_+}$ ; the integral for  $a_-$  likewise equals  $-\frac{2G\lambda}{\Delta_-}$ , where the negative sign is due to integrating from  $-\Delta_-$  to  $-\infty$ .

## 4.2.2 Viscosity

There are two types of viscosity — shear and bulk. Shear viscosity is the inter-streamline friction and is responsible for a radial flux of angular momentum, and bulk viscosity friction acts to retard the relative motions of particles converging towards or diverging away from each other, producing an additional momentum flux. The user provides parameters for the strengths of each type of viscosity; in our work, the two are set equal to each other. This follows the approach of [4], who note that [87] find shear and bulk viscosity equal in Saturn’s A ring. The equations for acceleration due to ring viscosity are given in Section 2.3.4 in [4] (Eqs. 26 through 29); see also Appendices A and B in [4]. To calculate the radial and tangential accelerations due to viscosity, `epi_int` must calculate the radial gradients in the angular and radial velocities in adjacent streamlines [4]. By analogy with the ring gravity algorithm, the code again uses parabolic fits to determine these velocities. When calculating the radial gradients, `epi_int` approximates the infinitesimal differentials as finite differences, discretizing them for simplicity.

### 4.2.3 Numerical Error

As noted above, in `epi_int`'s drift step, particles move on an orbit corrected for Saturn's oblateness via the epicyclic elements of [41]. Recall from Chapter 2 that these elements, while improvements to the osculating elements, are still truncated in eccentricity and inclination and not reversible. Thus, each drift step introduces small but nonzero errors of  $\mathcal{O}(e^3)$  to the system's total energy and angular momentum. We show the growth in angular momentum error in Fig. 4.2.

We are thus afforded a limited number of steps before numerical errors grow too large. Although `epi_int` is an imperfect code for simulating rings for hundreds of millions of years – we discuss this further in Section 4.4 – it is still quite suitable for the shorter proof-of-concept simulations we attempt here. We can also delay the onset of numerical instability by taking extremely large steps and simulating rings of very low eccentricities. In most N-body simulations, timesteps are expected to be  $\sim 0.05$  orbit periods to ensure accuracy. However, as we are solely integrating rings here, the orbital timescale is much less important, since rings do not meaningfully change that quickly. Instead, we care about the far longer *secular* timescale; provided our timesteps are small compared to this timescale, we can still accurately capture the long-period changes in which we are interested. In practice, this allows us to take timesteps of  $\sim 30$  orbit periods, dramatically increasing the number of orbits we can simulate before numerical errors overwhelm us.

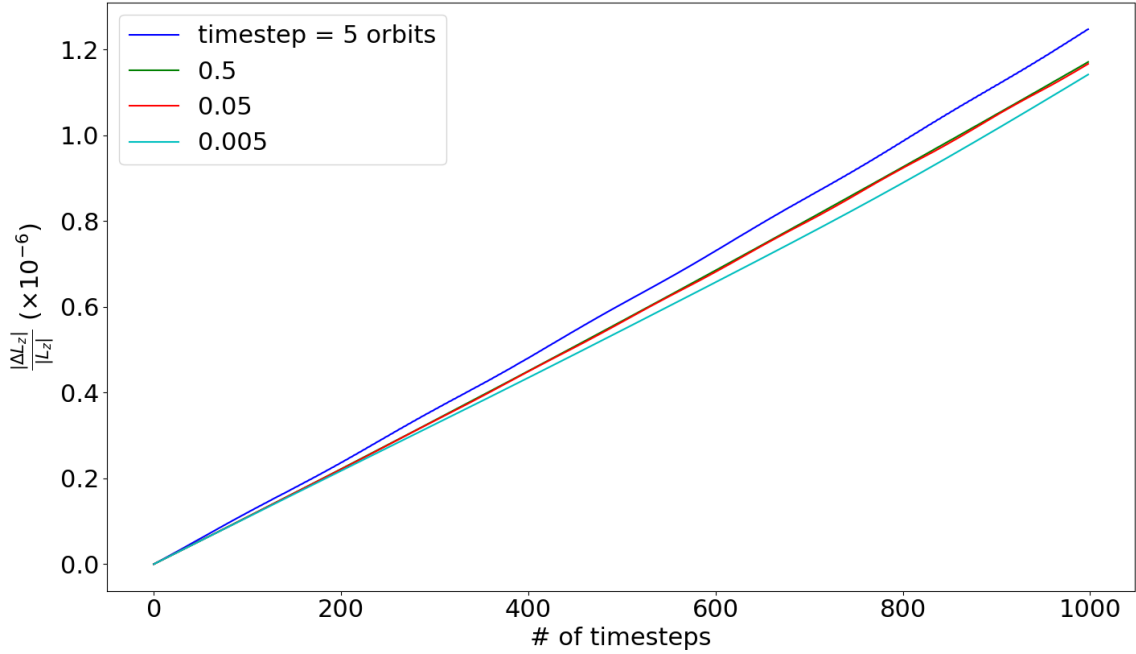


Figure 4.2: Display of the fractional  $z$  component of angular momentum  $\frac{|\Delta L_z|}{|L_z|}$  for four two-dimensional ring simulations that differ only in their timesteps. The rings have eccentricity  $e = 0.005$  and density  $\sigma = 10^{-6}$  in units of  $M_{\text{Saturn}} = 5.6846 \times 10^{29}$  g and  $r_{\text{ring}} = 1.178145 \times 10^{10}$  cm. For ease of comparison to theory, we use two streamlines, each with 250 particles. The initial semimajor axes of the two streamlines are  $1.0005 r_{\text{ring}}$  and  $0.9995 r_{\text{ring}}$ . The initial  $\Delta e$  is  $10^{-5}$ . There is no viscosity. The timestep for the simulation corresponding to the dark blue line is five orbits, while the timestep for the simulation represented by the green line is 0.5 orbits, etc. The green and red lines nearly lie atop each other. Note the linear growth in angular momentum error as the number of timesteps increases, regardless of the actual timestep value. Even varying the timestep over several orders of magnitude does little to change the rate of growth.

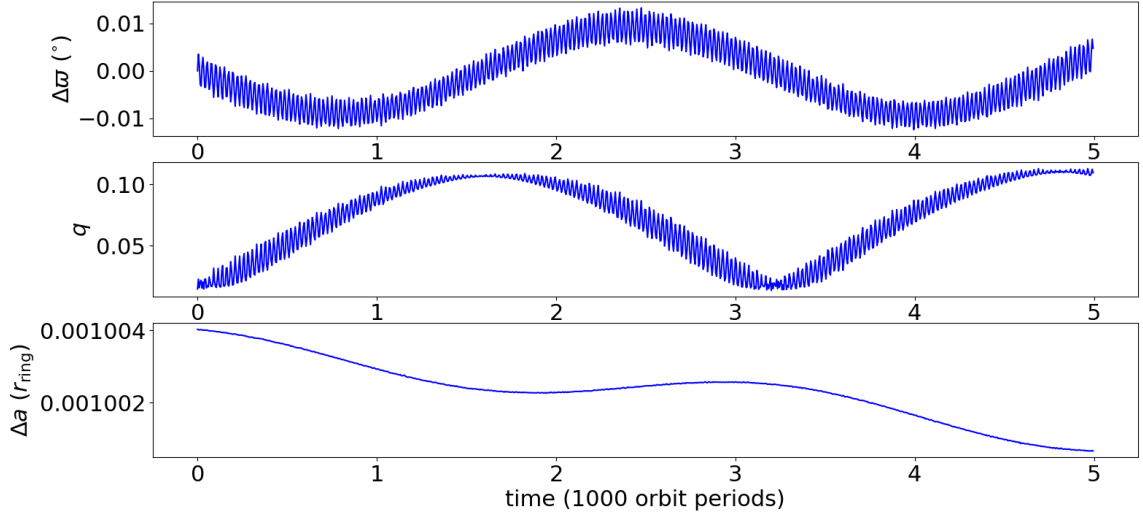


Figure 4.3: Three plots displaying the evolution of a ring that has been slightly perturbed from its equilibrium. The simulated libration time agrees very well with that predicted by [3] (see text). Initial conditions are identical to those in Fig. 4.2 – the only forces active are the ring’s self-gravity and the gravity from the oblate host planet. Our timestep was five orbital periods. From top to bottom, the panels feature the difference between outer and inner longitudes of periapse, the  $q$  parameter, and the difference  $\Delta a$  between the center of the ring and its edge, equal to half the width of the ring.

## 4.3 Results

### 4.3.1 Ring Equilibra

To test our internal energy source confinement mechanism, we first found a set of parameters that defined a ring in equilibrium, i.e., a ring whose streamline periapses were all in alignment that underwent rigid precession where the only important simulated forces were the ring’s self-gravity and the gravity of an oblate central planet. In Fig. 4.3, we have simulated a 2-streamline ring that has been slightly perturbed from its equilibrium and is consequently librating.

[3] give the libration frequency as:

$$\Omega = \frac{m_r}{\pi M} \left( \frac{a}{\Delta a} \right)^2 n H(q^2), \quad (4.9)$$

where  $n$  is the ring's mean motion and  $H(q^2)$  is given by:

$$H(q^2) = \frac{1 - (1 - q^2)^{\frac{1}{2}}}{q^2 (1 - q^2)^{\frac{1}{2}}}. \quad (4.10)$$

For  $q \lesssim 0.2$ ,  $H \approx \frac{1}{2}$ . The libration time is then  $\frac{2\pi}{\Omega}$ . We calculate a theoretical libration time of 3,141.6 orbit periods, very close to the simulated value of 3142.2. However, we also note that the theoretical result assumes a constant  $q$ , which in turn requires a ring of sufficient mass, and the simulated libration time for a ring of mass below  $\sim 3 \times 10^{-9}$  planetary masses will noticeably diverge from the theoretical libration time (Joe Hahn, private communication). The simulated ring mass in Fig. 4.3 is  $\sim 1.26 \times 10^{-8}$  planetary masses.

We simulated several ringlets using various timesteps in order to test the consistency of the libration time across different stepsizes and show our results in Fig. 4.4. Despite a factor of 40 between the shortest and longest timesteps, which varied from 0.016 to 0.63 orbital periods, we found reasonable agreement of libration time for all integrations. As expected, however, the shorter the timestep, the quicker the simulation crashed due to the unphysical exponential amplitude growth present in all simulations but most prevalent in those with the shortest timesteps.

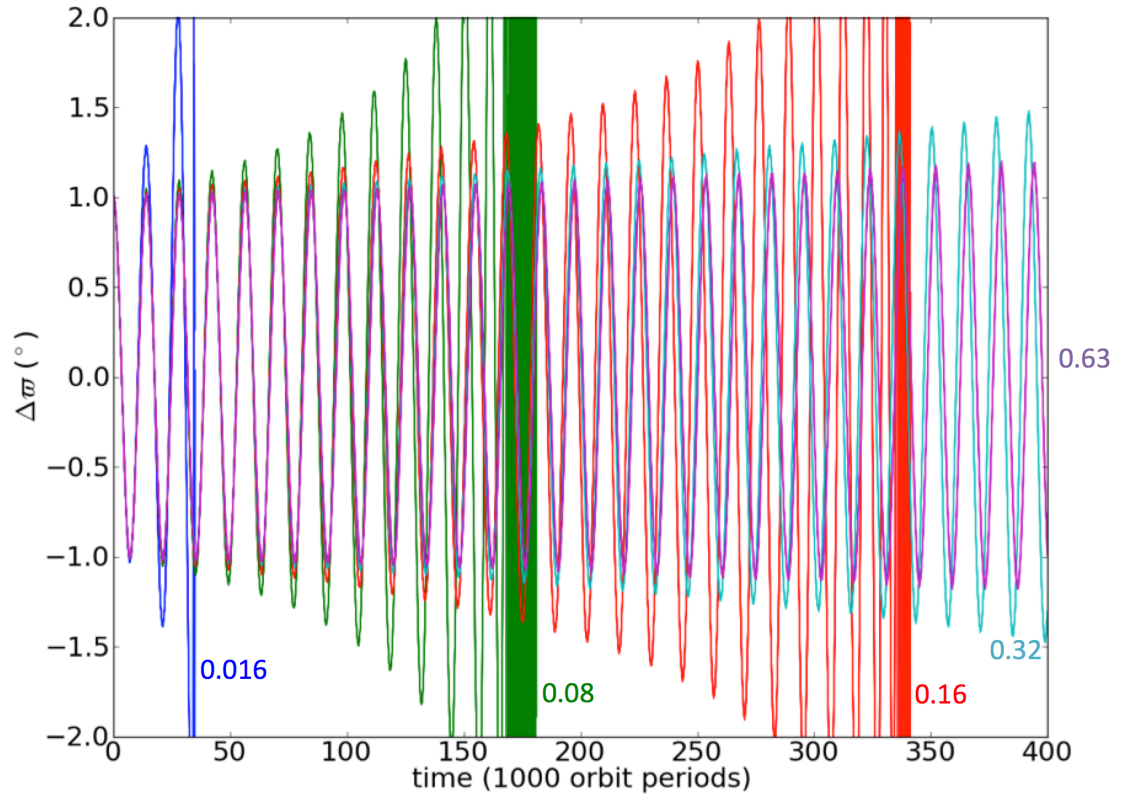


Figure 4.4: Five simulations of librating ringlets identical except for timestep. Only the differences in longitudes of periapse have been plotted. The blue curve has a timestep of 0.016 orbital periods, green has 0.08 orbital periods, red has 0.16, cyan 0.32, and magenta 0.63. Despite the wide range of stepsizes, all curves maintain very similar libration periods.

### 4.3.2 Addition of Viscosity

We modified the initial conditions from the simulations in Fig. 4.2 to include viscosity. The results are plotted in Fig. 4.5; we will refer to the top panel as panel 1, the next panel down as panel 2, etc.

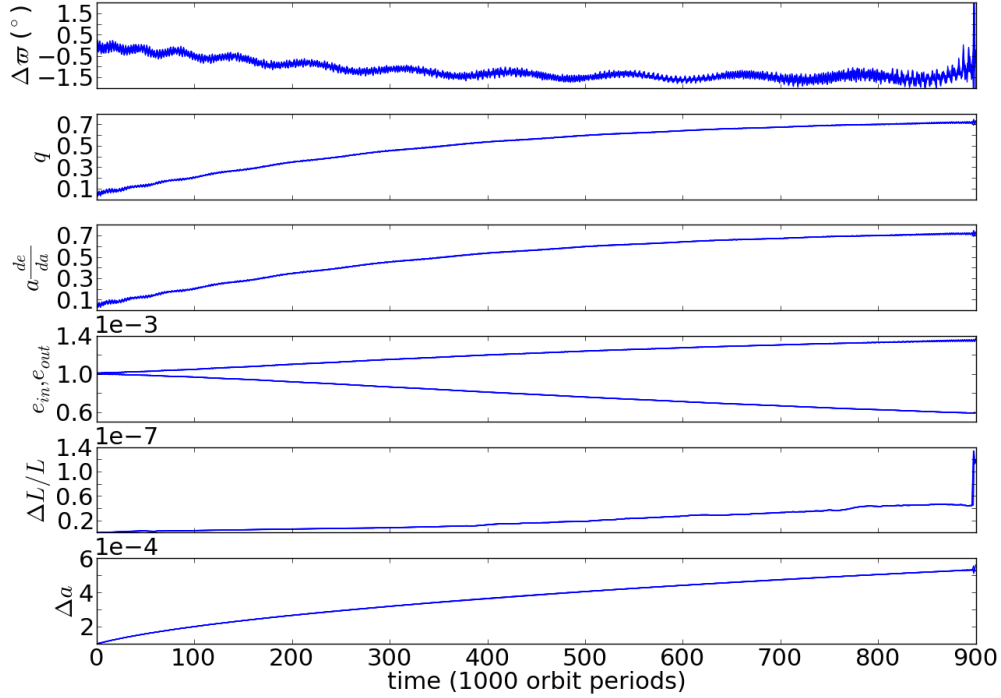


Figure 4.5: Several plots describing the evolution of a viscous, self-gravitating, narrow eccentric ringlet of two streamlines with sixteen particles per streamline. The ring is initialized with  $\Delta a = 10^{-4} r_{\text{ring}}$ ,  $e = 10^{-3}$ ,  $\Delta e = 10^{-5}$ , and  $\text{sigma} = 4.4 \times 10^{-8}$  in the units of Fig. 4.2. Both shear and bulk viscosity equaled  $2114 \text{ cm}^2 \text{ s}^{-1}$ . While these viscosity values are about an order of magnitude greater than is typical [4], they permitted us to greatly speed up the simulation while retaining a similar, if accelerated, evolution. The top panel features the difference between outer and inner longitudes of periapse. The second and third, and fourth panels from the top feature the  $q$  parameter, the eccentricity gradient term  $a \frac{de}{da}$ , and the inner and outer eccentricities  $e_{in}$  and  $e_{out}$ , respectively. The fifth panel shows  $\frac{\Delta L}{L}$ , which is consistently  $< 10^{-7}$  until the spike at the end indicating the onset of numerical instability. The bottom panel shows the difference  $\Delta a$  between the center of the ring and its edge, equal to half the width of the ring.

A ring with self-gravity but no viscosity in perfect equilibrium should have perfect periapse alignment, i.e.,  $\Delta\varpi$  (panel 1) should stay constant at 0, so this ring starts out reasonably close to its equilibrium point. However, the center around which  $\Delta\varpi$  librates drifts downwards approximately  $1^\circ$ . This indicates that the ring has developed a “twist,” but since panels 2 and 3 are nearly identical, i.e., since  $a \frac{de}{da} \approx q$  (recalling Eq. 4.6), the twist is unimportant in this case. We also see in the second panel that the eccentricity gradient begins at  $\sim 0.05$  but steadily grows to  $\sim 0.71$  by the conclusion of the simulation, indicating that the eccentricities began very close to each other and slowly diverged over time, as is supported by panel 3. The spike at the very end of the  $\Delta\varpi$  and  $\frac{\Delta L}{L}$  panels indicates the onset of numerical instability, which is why we chose to end the simulation after 900,000 orbits. Finally, panel 6 shows that this is an example of a spreading ring, as predicted by energy losses from viscosity. The width increases by the square root of time, in excellent agreement with theory [88].

### 4.3.3 Titan Ringlet

We modified our initial conditions to simulate the Titan ringlet around Saturn; our results are plotted in Figs. 4.6 and 4.7.

In Fig. 4.6, the ring is moving into its equilibrium; when the twist is small (between 0 and 110,000 orbits), it spreads, but when it is large (between 110,000 and 150,000 orbits), it contracts. Furthermore, before the ring reaches its equilibrium, the eccentricities of the inner and outer streamlines diverge. Once the equilibrium

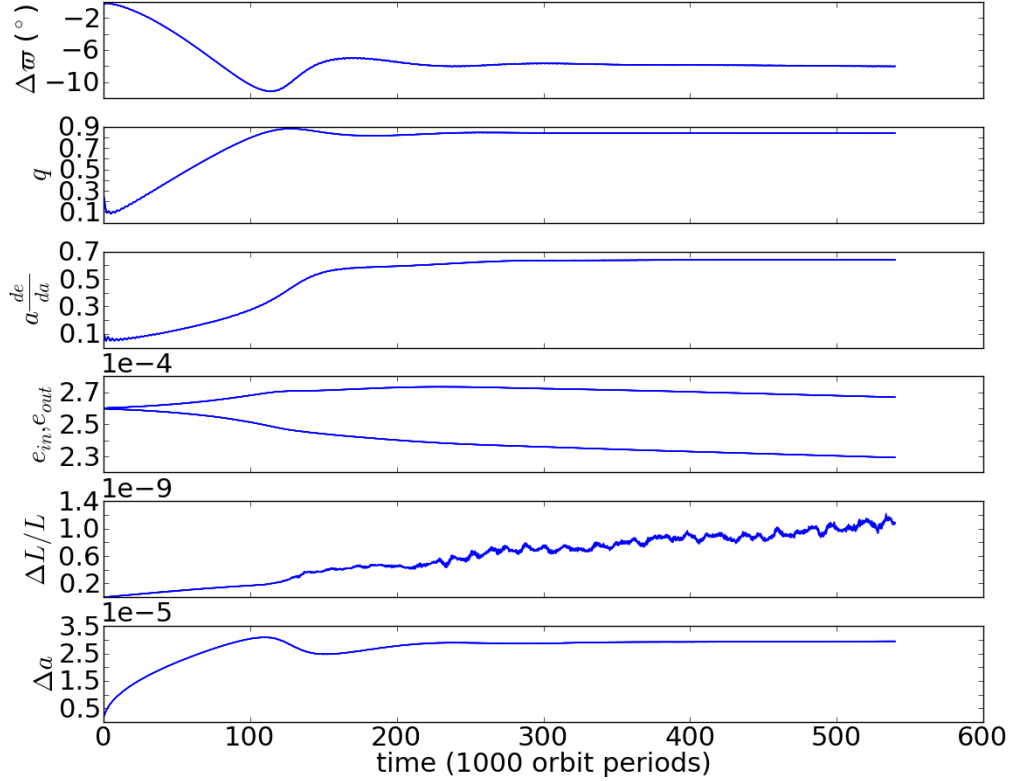


Figure 4.6: Several plots describing a possible evolutionary path of the Titan ringlet. In this two-dimensional simulation, the ring spreads until  $t \sim 110$ , but then contracts until  $t \sim 150$ . The reason for such contraction is easiest to see via panel 1 – the ring “overshoots” the equilibrium twist value and starts to compensate. After briefly spreading again, it reaches its equilibrium at  $t \sim 300$  and remains confined. All parameters of the host planet (e.g., mass, radius, etc.) are again equal to those of Saturn. The initial inner and outer semimajor axes are  $1 - 1.6 \times 10^{-6}$  and  $1 + 1.6 \times 10^{-6}$  respectively, using a length unit of  $7.7871 \times 10^9$  cm (see Table 4.1). The initial eccentricity of the inner streamline is 0.00026, while the initial  $\Delta e$  is 0. The ring begins with a very small pericenter twist of  $-0.062^\circ$ . Both shear and bulk viscosity parameters are  $63.4 \text{ cm}^2 \text{ s}^{-1}$ . Density is  $8.93 \text{ g cm}^{-2}$ . The ring is in equilibrium from  $t \sim 300$  to the end of the integration.

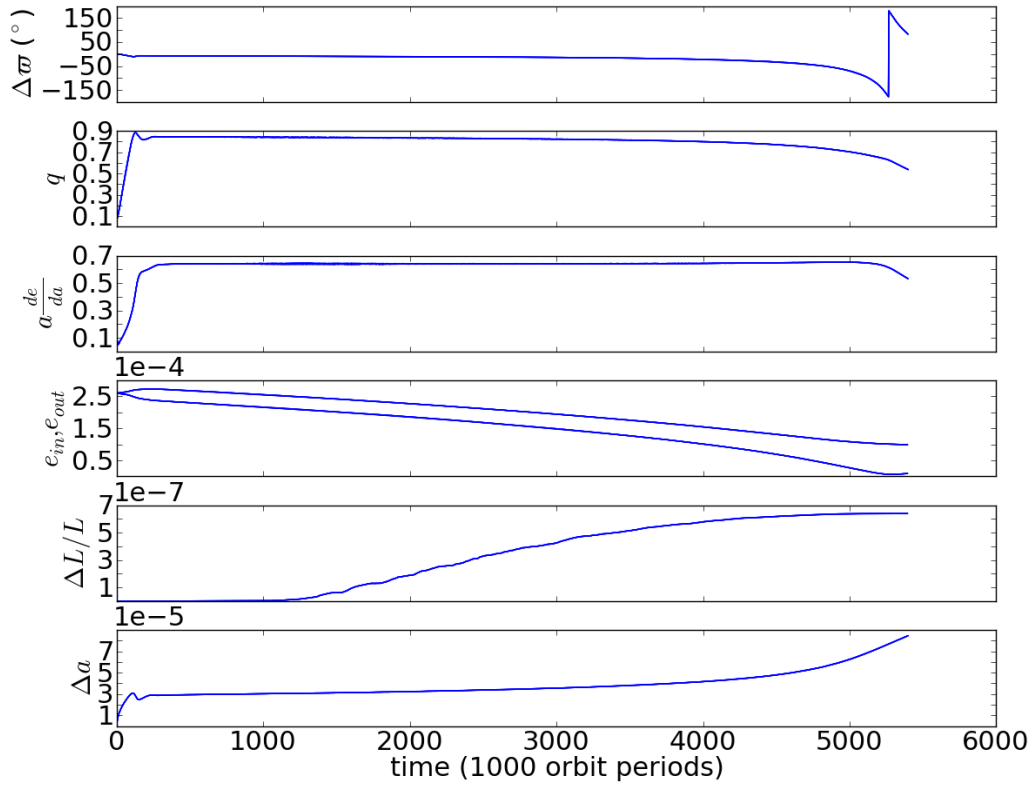


Figure 4.7: Identical to Fig. 4.6 except run for ten times longer. While the ring is in equilibrium and the eccentricity is above  $e_{crit}$ , i.e., from  $t \sim 300 - 1300$ , the ring spreads quite slowly, although once it is sufficiently circular, the spreading timescale shortens considerably.

is reached, however, the width and twist remain stable and the inner and outer eccentricities begin slowly decaying together. In Fig. 4.7, we see that the ring spreads on very long timescales while its inner eccentricity is above  $e_{crit}$ , but once it gets too low, the equilibrium is lost, and the spreading timescale gets much shorter. This is in qualitative agreement with our model’s prediction in Section 4.1.3 that the ring would spread if and only if its eccentricity was sufficiently high; we argued that the ring would preferentially circularize rather than spread. In addition, the simulated  $q$  stabilizes very close to  $q_{crit}$  while the ring remains confined, in excellent agreement with the predictions of [76]. We also note that the ring develops a sizeable twist soon after the integration starts. Our model correctly predicts that when the twist is too small, the ring spreads (from  $t \sim 0 - 115$ ); when it is too large, the ring shrinks (from  $t \sim 110 - 150$ ); and when it stabilizes, the ring’s width stays constant (from  $t \sim 300 - 1300$ ).

## 4.4 Discussion

### 4.4.1 Continued Model Testing

We have shown that rings in equilibrium can confine themselves even in the absence of any perturbing satellite. Our results in Figs. 4.6 and 4.7 qualitatively agree with several predictions of our model, including the slow circularization, the spreading and contracting in response to displacement from equilibrium, and the ring confinement. Nevertheless, there remains disagreement with observations. In particular, the confinement begins at  $a \frac{de}{da} \sim 0.64$ , but [3] note that the Titan ringlet’s

observed  $a \frac{de}{da}$  equals 0.44. Furthermore, the simulation depicted in Figs. 4.6 and 4.7 was initialized with the Titan ringlet’s current observed eccentricity, taken from [3] (see Table 4.1). However, the real ringlet’s initial eccentricity was likely higher than it is now if our model’s predictions are accurate, so we can investigate how a higher simulated initial eccentricity affects the integration results. We can also explore simulating other ringlets around other bodies to evaluate our model’s success in reproducing other observations.

## 4.4.2 Different Integrator

### 4.4.2.1 epi\_int\_lite

In order to simulate ring evolution for hundreds of millions of years, we must use a different integrator. Joe Hahn (private communication) has written `epi_int_lite`, a new version of `epi_int`; there are two main differences between the two codes. First, the oblateness force is now in the kick step. Second, while `epi_int_lite` still corrects the orbital elements for oblateness, the correction algorithm now features a perfect inverse; one can transform from state vectors to elements to state vectors again with no error. Although the new algorithm does not correct the elements to  $\mathcal{O}(e^2)$ , as did the original epicyclic elements, the perfect inverse function rids `epi_int_lite` of the energy and angular momentum errors that plagued its original. The new code also features self-gravity and viscosity forces that work identically to their `epi_int` counterparts, so it can also simulate self-confining rings (Joe Hahn, private communication).

#### 4.4.2.2 HNBody

The symplectic integrator HNBody [14] is well suited as a substitute for epi\_int, as it already possesses much of that integrator’s functionality. We are currently upgrading HNBody to simulate self-gravitating, viscous rings approximated as streamlines traced by a single particle [89]. Unlike in epi\_int, HNBody uses the standard osculating orbital elements, and the additional force due to planetary oblateness is accounted for in the kick step, as in epi\_int\_lite.

We use the same force law to determine the gravity felt between streamlines as per Eq. (4.7). However, because we only use a single tracer particle, we cannot use the same means of getting the streamline distances as epi\_int. Instead, given a point on one streamline (designated with subscript  $j$ ), we first estimate the closest point on another streamline (subscript  $i$ ) to occur at the (osculating) true anomaly  $\nu_i = \nu_j - \Delta\omega - \Delta\Omega$ , where  $\Delta\omega = \omega_i - \omega_j$ , etc. We then define two points to either side of  $\nu_i$  at true anomalies  $\nu_{i-} = \nu_i + \epsilon$  and  $\nu_{i+} = \nu_i + \epsilon$ ; we typically use  $\epsilon = 0.01$  radians. After calculating the three distances  $l_i$ ,  $l_{i+}$ , and  $l_{i-}$  between the point at  $\nu_j$  and the three points at  $\nu_i$ ,  $\nu_{i-}$ , and  $\nu_{i+}$ , respectively, we then fit a parabola to these three “points” in  $\nu - l$  space. These points have no physical meaning; we are *not* fitting the streamline itself. The minimum ( $\nu_{\min}, l_{\min}$ ) point of the parabola provides us a new guess for the true anomaly corresponding to the point of closest approach (i.e.,  $\nu_{\min}$ ), along with the distance  $l_{\min}$  at that point. We then iterate this process twice more; further iterations typically do not meaningfully improve the solution.

We have not yet implemented a viscosity force, but the upgraded HNBody

already compares favorably to `epi_int`. Most importantly, the secular errors in angular momentum and energy no longer appear. Furthermore, `HNBody` permits full three-dimensional ring simulations, which are not possible in `epi_int`. Finally, `HNBody` is over one hundred times faster than `epi_int` due to the choice of language for each – C for `HNBody`, IDL for `epi_int`. Preliminary tests are encouraging – `HNBody` can simulate ringlets in equilibrium and reproduces the correct libration frequency. The most significant disadvantage is that, as it cannot yet simulate a viscous force, `HNBody` cannot currently simulate self-confining rings. In addition, the use of only a single tracer particle per streamline prevents `HNBody` from simulating multiple-lobed rings, as are observed in nature.

## Chapter 5: Titan’s Unstable Origins

In the last Chapter, we examined the Titan ringlet while largely ignoring Titan itself. The moon is fascinating in its own right, however; its mass dominates that of every other body in Saturn’s satellite system, and its orbit is unusually eccentric and inclined. The leading theories of satellite formation do not satisfactorily explain all of Titan’s properties; we think we offer a more compelling model.

### 5.1 Introduction

#### 5.1.1 Background

Saturn’s largest moon is odd. The origins and evolution of Titan, with its enormous mass of  $M_T = 2.3670 \times 10^{-4} M_p$  for Saturn mass  $M_p$  [90] and relatively large eccentricity and inclination of 0.0288 and  $0.28^\circ$ , respectively, defy conventional explanation. Its mass, 97% of all mass in orbit around Saturn [91], largely immunizes it from perturbations due to other moons, and we would expect tidal forces (see Section 5.2.2) to circularize and un-incline its orbit relative to Saturn’s equatorial plane. It also occupies a somewhat “lonely” region of Saturn’s satellite system; only tiny Hyperion is nearby, sitting in a 4:3 mean-motion resonance with its huge

neighbor. Finally, Titan’s mass, as a percentage of its host planet Saturn, roughly equals the combined masses of the large moons of Jupiter and Uranus as percentages of their respective host planets within a factor of a few [92]. No self-consistent explanation for all of these features yet exists.

All modern approaches to satellite formation around gas giants assume a limited resemblance to planet formation around stars (e.g., [93]). The analogy is a reasonable first approximation since both cases concern the formation of nearly spherical bodies in a gas disk around a far more massive (and luminous, via [94] and [95]) body whose gravity dominates that of all others. Closer inspection, of course, reveals differences. Most importantly, gas and planetesimal inflows from the solar nebula to the circum-planetary (gas) disk (CPD) are fundamental to satellite formation, whereas the interstellar medium plays a less critical role to planetary formation.

Several works (e.g., [96], [97], [98], [99], [100], via [91]) have addressed this issue with the “gas-starved” model of satellite evolution. In this scenario, Saturn hosted several generations of satellites during its CPD phase, in which the disk was “fed” gas and dust from the solar nebula. All but the last spiraled into Saturn due to gas forces that robbed them of energy and shrunk their orbits on timescales much shorter than the lifetime of the CPD. The final generation survived because gas inflow ceased, the CPD thinned, and migration halted. While this model has many appealing aspects and can explain the origins of the *physical* properties of Saturn’s satellites, e.g. their masses and densities, we think more investigation is needed to explain Titan’s *orbital* properties, i.e. its eccentricity and inclination.

Furthermore, [101] have recently challenged the gas-starved model, which assumes that satellitesimals (which are to satellites as planetesimals are to planets) can form purely from dust agglomeration. Via [102], they argue that rapid inward drift of dust particles makes this highly unlikely. [101] also contend that once the host planet gets large enough to open a gap in the protoplanetary disk, dust inflow will drop by approximately an order of magnitude (see references therein), and there simply will not be enough to form the moons we see today. Instead, following the approach of [103], [101] invoke the capture and ablation of planetesimals into the CPD to explain how satellite seeds can form.

Finally, [104] suggest that Titan might have agglomerated out of a very massive set of rings but then estimate its tidal age to be  $\sim 10$  Gyr, concluding that this formation mechanism is unlikely. In addition, Titan is probably not a captured object (as is likely true for, e.g., Triton [105]). First, the chance that Titan would happen to capture in its current prograde, low-inclination orbit is  $\sim 0.5\%$  - quite low, given that any inclination between  $0$  and  $45^\circ$  would be equally likely. Furthermore, in this scenario, Titan's orbit would be very elliptical upon capture. This would imply that Hyperion formed after Titan's arrival because otherwise, it would have been ejected almost immediately following any gravitational interaction with the much more massive moon.

### 5.1.2 Orbital Evolution After Formation

The details of satellite formation within the CPD thus remain hotly debated. This chapter, however, is agnostic towards any specific model. We assume only that after the CPD is gone, a group of large satellites in a 1:2:4 mean-motion resonance remain, analogous to Io, Europa, and Ganymede at Jupiter. They might form in these resonances [101], or enter them later due to tidal migration in a process similar to that seen in Chapter 2. We think these moons then merge into a single massive body, i.e., Titan, following a dynamical instability.

This model can naturally explain all of Titan’s unusual features. First, both its “loneliness” and its unusually large mass are due to the agglomeration or accretion of all nearby moons during its formation. In addition, the merging bodies would likely undergo repeated close approaches that would drive up their eccentricities prior to the instability, and the final merged body would thus have an anomalously high eccentricity as well, although it would damp away over time due to tidal forces (see Section 5.2.2).

The inclination argument is less intuitive – how can a merger of largely equatorial satellites yield a non-equatorial body? The answer lies in each satellite’s Laplace plane, the reference plane about whose axis the satellite’s orbit precesses and to which the satellite is typically inclined; [106] note that, e.g., Iapetus is inclined  $7.5^\circ$  to its Laplace plane. This plane can be thought of as a weighted average of the planet’s equatorial plane and the plane in which the planet orbits the Sun. The former dominates near Saturn and the latter dominates far therefrom. Mergers

of satellites inclined from their Laplace planes can thus result in a body inclined from the planet’s equator due to the Sun’s influence.

Finally, this model can account for Hyperion’s origin as well. Collisions between Titan-sized objects would throw up considerable debris, most of which would re-accrete onto the merged body. However, a small fraction would escape, pile up at a nearby resonance, and eventually agglomerate into a single body. This would explain both the 3:4 Titan-Hyperion mean-motion resonance as well as Hyperion’s unusual, sponge-like appearance – low merger speeds would yield a likewise low-density object. However, we do not simulate this process here.

To our knowledge, this idea was first raised in [107], although they were more interested in the formation of Saturn’s mid-sized moons than of Titan. Likewise, [101] briefly discuss a chain instability, but only study the formation of the resonant satellites, not their post-gas disk evolution. We investigate such evolution here, with the goal of understanding the circumstances under which satellites can undergo dynamical instabilities and the physical processes responsible for them. We do not yet study post-instability evolution. In particular, we examine the effects that satellite mass distribution and migration speed have on instability likelihood.

## 5.2 Integration Setup

### 5.2.1 Initial Conditions

We use the symplectic integrator option within the N-body integrator HNBODY [14] to simulate the motion of Saturn plus three satellites, whose initial orbits we

include in Table 5.1. We account for Saturn’s oblateness by including the zonal harmonic coefficients  $J_2 = 16290.573 \times 10^{-6}$ ,  $J_4 = -935.314 \times 10^{-6}$ , and  $J_6 = 86.340 \times 10^{-6}$  in its gravitational potential, using a reference radius  $R_p = 6.0330 \times 10^7$  m [43]. We also approximate the presence of tidal bulges by assigning all bodies a  $\frac{k_2}{Q}$  value for Love number  $k_2$  and tidal dissipation parameter  $Q$ . As we shall shortly see, this ratio governs the tidally induced secular changes to the satellites’ semimajor axes and eccentricities.

Both Saturn’s and Titan’s Love numbers are known to much greater precision than their  $Q$  parameters – we assume our simulated satellites mirror Titan itself and therefore adopt its  $k_2$  and  $Q$  values for them. The  $k_2$  values for Titan and Saturn are respectively estimated at  $k_{2s} = 0.6 \pm 0.2$  [108] and  $k_{2p} = 0.390 \pm 0.024$  [109]. [5] estimate  $Q_s \sim 100$  for Titan to the nearest order of magnitude, while [110] and [111] predict  $\frac{k_{2s}}{Q_s}$  of the mid-sized moons Dione and Enceladus to be of order  $10^{-4}$ , largely due to a much smaller  $k_2$  value. We thus test both  $\frac{k_{2s}}{Q_s} = 6 \times 10^{-3}$  and  $6 \times 10^{-4}$  for each satellite. Estimates of  $Q_p$  at Saturn, meanwhile, span multiple orders of magnitude, from the traditional lower bound of  $\sim 18,000$  [112] to the more modern, somewhat controversial values of  $\sim 1,700$  [109] and even  $\sim 100$  [113]. [114] have also suggested that Saturn’s  $Q$  may have been larger in the past, reinforcing its already considerable uncertainty. To account for this, we test  $\frac{k_{2p}}{Q_p} = 10^{-3}$ ,  $10^{-4}$ , and  $10^{-5}$  for Saturn.

The resultant migration rates are too slow for convenient integration, so we speed up our simulations by multiplying  $k_{2p}$  and  $k_{2s}$  by a speed-up factor  $C$  equal

to either  $\left(\frac{k_{2p}}{Q_p}\right)^{-1}$  or  $\frac{1}{10}\left(\frac{k_{2p}}{Q_p}\right)^{-1}$ . Simulations using  $C = \left(\frac{k_{2p}}{Q_p}\right)^{-1}$  go for 10 Myr (equivalent to 10 Gyr), while those using  $C = \frac{1}{10}\left(\frac{k_{2p}}{Q_p}\right)^{-1}$  go for 40 Myr (equivalent to 4 Gyr). This practice is quite common; in justifying their own similar use of such a factor, [115] point out that [116], [117], [111], and [110] have all used one as well. The drawback is that moving too quickly can force the satellites past weak second- and third-order resonances in which they would otherwise have been captured. Such resonances would excite our satellites' eccentricities and/or inclinations, making them more prone to dynamical instability. We thus may err on the side of generating too few instabilities with this approach.

We use two different algorithms to get our mass distributions and require that the total combined satellite mass equal  $M_T$  in both. Whereas the first algorithm is designed to produce more evenly distributed masses in most cases, the second concentrates the satellites' mass in the innermost body. For the first, we vary the mass ratios  $\psi_{13} = \frac{m_1}{m_3}$  (inner mass to outer mass) and  $\psi_{23} = \frac{m_2}{m_3}$  (middle mass to outer mass), independently assigning each a value of 4,  $2\sqrt{2}$ , 2,  $\sqrt{2}$ , 1,  $\frac{1}{\sqrt{2}}$ ,  $\frac{1}{2}$ ,  $\frac{1}{2\sqrt{2}}$ , or  $\frac{1}{4}$  for eighty one possible combinations. Using this scheme, the three masses are  $m_1 = \psi_{13}m_3$ ,  $m_2 = \psi_{23}m_3$ , and  $m_3 = \frac{M_T}{1+\psi_{13}+\psi_{23}}$ . For the second algorithm, we vary the mass ratios  $\psi_{21} = \frac{m_2}{m_1}$  (middle mass to inner mass) and  $\psi_{31} = \frac{m_3}{m_1}$  (outer mass to inner mass) between  $\frac{1}{\sqrt{2}}$ ,  $\frac{1}{2}$ ,  $\frac{1}{2\sqrt{2}}$ ,  $\frac{1}{4}$ ,  $\frac{1}{4\sqrt{2}}$ ,  $\frac{1}{8}$ ,  $\frac{1}{8\sqrt{2}}$ , and  $\frac{1}{16}$ . The second algorithm yields thirty eight new possible combinations<sup>1</sup> – we thus test 119 mass distributions total. We test all distributions for each choice of  $\frac{k_{2p}}{Q_p}$  and  $\frac{k_{2s}}{Q_s}$  as well as both speed-up factors, yielding 1,428 simulations total.

---

<sup>1</sup>The remaining twenty six are duplicates of combinations from the first algorithm.

#	$a (R_p)$	$e$	$i (^\circ)$	$\Omega (^\circ)$	$\varpi (^\circ)$	$\lambda (^\circ)$
1	6.0	0.01	0.001	0	0	0
2	9.6	0.01	0.001	0	0	0
3	15.0	0.01	0.001	0	0	0

Table 5.1: Initial semimajor axis  $a$ , eccentricity  $e$ , inclination  $i$ , longitude of ascending node  $\Omega$ , longitude of periapse  $\varpi$ , and mean longitude  $\lambda$  for each of our simulated satellites in every integration. We designate the inner body as 1, the middle body as 2, and the outer body as 3.

## 5.2.2 Tidal Forces

We exclusively study post-disk evolution of our satellites and so ignore gas forces. However, the mutual tides that Saturn and the satellites raise in each other<sup>2</sup> produce important effects that we lose by modeling all bodies as point particles. In particular, tidal bulges force secular changes to the satellites' semimajor axes  $a$  and eccentricities  $e$ ; tides raised in the planet increase  $a$  and  $e$ , while those raised in the satellite decrease them [5]. In units of  $M_p$ ,  $R_p$ , and Keplerian circular velocity  $v_K = na$ , and ignoring terms of  $\mathcal{O}(e^2)$ , the tides raised in the planet produce the following [118]:

$$\frac{1}{a} \frac{da}{dt} \equiv \tau_{ap}^{-1} = 3 \frac{k_{2p}}{Q_p} ma^{-6} \quad (5.1)$$

and

$$\frac{1}{e} \frac{de}{dt} \equiv \tau_{ep}^{-1} = \frac{57}{8} \frac{k_{2p}}{Q_p} ma^{-6} \quad (5.2)$$

while via [119] the tides raised in a tidally locked satellite yield:

---

<sup>2</sup>We ignore satellite-satellite tides, which are both much more complex and much weaker.

$$-\frac{1}{a} \frac{da}{dt} \equiv \tau_{as}^{-1} = 21 \frac{k_{2s}}{Q_s} m^{-1} R_s^5 a^{-6} e^2 \quad (5.3)$$

and

$$-\frac{1}{e} \frac{de}{dt} \equiv \tau_{es}^{-1} = \frac{21}{2} \frac{k_{2s}}{Q_s} m^{-1} R_s^5 a^{-6} \quad (5.4)$$

for satellite mass and radius  $m$  and  $R_s$ , respectively, where  $\tau$  is the timescale of the change. We can determine which dominates by taking the ratios  $\frac{\tau_{ap}}{\tau_{as}}$  and  $\frac{\tau_{ep}}{\tau_{es}}$ :

$$\frac{\tau_{ap}}{\tau_{as}} = 7 \frac{k_{2s}}{Q_s} \left( \frac{k_{2p}}{Q_p} \right)^{-1} m^{-2} R_s^5 e^2 = 7 \frac{k_{2s}}{Q_s} \left( \frac{k_{2p}}{Q_p} \right)^{-1} \left( \frac{4\pi}{3} \rho_s \right)^{-\frac{5}{3}} m^{-\frac{1}{3}} e^2 \quad (5.5)$$

and

$$\frac{\tau_{ep}}{\tau_{es}} = \frac{28}{19} \frac{k_{2s}}{Q_s} \left( \frac{k_{2p}}{Q_p} \right)^{-1} m^{-2} R_s^5 = \frac{28}{19} \frac{k_{2s}}{Q_s} \left( \frac{k_{2p}}{Q_p} \right)^{-1} \left( \frac{4\pi}{3} \rho_s \right)^{-\frac{5}{3}} m^{-\frac{1}{3}}, \quad (5.6)$$

where  $\rho_s = 0.7263$  is the density (equal to Titan's current density in units of  $M_p R_p^{-3}$ ) that we assign to all simulated satellites [90]. The lowest possible  $\frac{\tau_{ep}}{\tau_{es}}$  across all tested  $m$ ,  $\frac{k_{2p}}{Q_p}$ , and  $\frac{k_{2s}}{Q_s}$  values is  $\sim 2$ ; we thus ignore the  $+\frac{de}{dt}$  from Eq. (5.2) due to the tide raised in the planet. However,  $\frac{\tau_{ap}}{\tau_{as}}$  ranges from  $\sim 10e^2$  to  $\sim 3 \times 10^4 e^2$ ; outward migration is only guaranteed for  $e \ll 0.01$  in the latter cases.

In practice, therefore, we can approximate the relative timescales of the  $\frac{da}{dt}$

and  $\frac{de}{dt}$  by comparing Eqs. (5.1) and (5.4). This gives:

$$\frac{\tau_{a\text{p}}}{\tau_{e\text{s}}} = \frac{7 k_{2\text{s}}}{2 Q_{\text{s}}} \left( \frac{k_{2\text{p}}}{Q_{\text{p}}} \right)^{-1} \left( \frac{4\pi}{3} \rho_{\text{s}} \right)^{-\frac{5}{3}} m^{-\frac{1}{3}}. \quad (5.7)$$

The  $\frac{de}{dt}$  thus ranges from  $\sim 6$  to  $\sim 1500$  times faster than the  $\frac{da}{dt}$ . As we shall see, this ratio plays a crucial role in determining the likelihood of instabilities.

Following [115], we include these effects via additional forces per unit mass in the directions  $\hat{\mathbf{B}} = (\hat{\mathbf{r}} \times \hat{\mathbf{v}}) \times \hat{\mathbf{r}}$  and  $\hat{\mathbf{r}}$  for satellite position and velocity vectors  $\mathbf{r} = r\hat{\mathbf{r}}$  and  $\mathbf{v} = v\hat{\mathbf{v}}$ , respectively [6]:

$$\mathbf{f}_{\text{B}} = \frac{3k_{2\text{p}}}{2Q_{\text{p}}} mr^{-6} v^2 \hat{\mathbf{B}} \quad (5.8)$$

and

$$\mathbf{f}_{\text{r}} = -\frac{21k_{2\text{s}}}{2Q_{\text{s}}} m^{-1} R_{\text{s}}^5 r^{-6} v \dot{r} \hat{\mathbf{r}} \quad (5.9)$$

again working in units of  $M_{\text{p}}$ ,  $R_{\text{p}}$ , and  $v_{\text{K}}$ . The force  $\mathbf{f}_{\text{B}}$  is responsible for the  $+\frac{da}{dt}$  in Eq. (5.1), while  $\mathbf{f}_{\text{r}}$  yields the  $-\frac{da}{dt}$  and  $-\frac{de}{dt}$  from Eqs. (5.3) and (5.4) [115] (see also [34] and [120]).

$\log_2 \left( \frac{m_2}{m_1} \right)$	$\log_2 \left( \frac{m_3}{m_1} \right)$	$C$
-2	-0.5	100
-2	1	100
-3	-0.5	1000
-3	-1	1000
-3.5	-0.5	1000
-3.5	-1	1000
-3.5	-1.5	1000
-3.5	-2	1000
-3.5	-2.5	100
-4	-0.5	1000
<b>-4</b>	<b>-1</b>	<b>1000</b>
<b>-4</b>	<b>-1.5</b>	<b>1000</b>
-4	-2	1000
-4	-2.5	1000
-4	-2.5	100
-4	-3	1000
-4	-3	100
-4	-3.5	1000
-4	-3.5	100

Table 5.2: Unique parameters of all simulations in which two or more bodies’ orbits crossed for at least 1 Myr. In the simulations whose parameter sets are bolded, one or more satellites was ejected from the system entirely. We include the middle to inner satellite and outer to inner satellite mass ratio  $\frac{m_2}{m_1}$  and  $\frac{m_3}{m_1}$ , respectively as well as the speed-up factor  $C$ . Every simulation used  $\frac{k_{2p}}{Q_p} = 10^{-3}$  and  $\frac{k_{2s}}{Q_s} = 6 \times 10^{-4}$ .

## 5.3 Results

### 5.3.1 Overview

We find limited instances of dynamical instability; the overwhelming majority of the parameter space yielded simulations in which the three satellites migrated outward with very low eccentricities and did not interact with each other. We give the parameters of each simulation in which two or more bodies’ orbits crossed for at least 1 Myr in Table 5.2.

Using Table 5.2, we can identify three important criteria that are normally satisfied before the satellites go unstable. First, we require that  $\tau_a \sim \tau_e$ , which in turn requires that  $\frac{k_{2p}}{Q_p} \sim \frac{k_{2s}}{Q_s}$ . This criterion lies at the very edge of our parameter space, in which we set  $\frac{k_{2p}}{Q_p} = 10^{-3}$  (for  $Q_p = 100$ ) and  $\frac{k_{2s}}{Q_s} = 6 \times 10^{-4}$  (for  $Q_s = 1000$ ). Every simulation that featured crossing orbits used these values.

Second, the middle satellite’s mass typically comprises roughly 5-10% of the total satellite mass. This satellite is usually the one to trigger the instability because it can be trapped in two eccentricity resonances instead of just one; its eccentricity can grow rapidly in this case. It needs a sufficiently low mass such that these resonances can quickly grow its eccentricity but a sufficiently high mass to meaningfully disturb the other satellites upon repeated close approaches.

Third, the inner body’s mass is always greater than those of the other two, and particularly larger than that of the middle one. This, coupled with a large  $\frac{k_{2p}}{Q_p}$ , permits very rapid migration while the satellites are still close to Saturn; this can help destabilize the system early. In all of the simulations featuring crossing orbits, the orbits began crossing almost immediately, when the satellites were close together and the inner body’s influence was maximized.

### 5.3.2 Individual Simulations

In this section, we present two of our most noteworthy simulations. In the simulation shown in Fig. 5.1, the middle body has a very low mass and is quickly perturbed by its two dominant neighbors. All eccentricity resonances are active (see

Fig. 5.2), so both the middle and outer bodies' orbits quickly become very eccentric and cross each other. This does not immediately lead to dynamical instability, however; the simulation continues for another  $\sim 140$  Myr (scaled to our speed-up factor  $C = 1000$ ) before the middle body is ultimately ejected. There is no obvious trigger for the instability itself; the system appears to be highly chaotic.

In Fig. 5.3, we show a similar system, in which orbits cross very quickly, that does not go unstable. The reason is likely due to the outer body, whose eccentricity remains low at the beginning of the integration, preventing crossing orbits between satellites 2 and 3. The mass distribution between the satellites is similar to that of the simulation from Fig. 5.1, and via Fig. 5.4, we see that  $\varphi_{32,o}$  is librating at the beginning of the simulation as before. The relatively sedate initial nature of the outer body compared to Fig. 5.1 is thus somewhat puzzling. Nevertheless, this illustrates that even under favorable conditions, instability is possible but not guaranteed.

## 5.4 Discussion

### 5.4.1 Review

We have shown that when  $\tau_a \sim \tau_e$ , a system of three satellites in which the inner mass is largest and the middle is smallest can quickly go unstable while the satellites are close together. This could have significant implications for the evolution of Titan – we argue that Titan was formed via such an instability among a resonant chain of satellites similar to the Galilean moons at Jupiter. To get such an instability

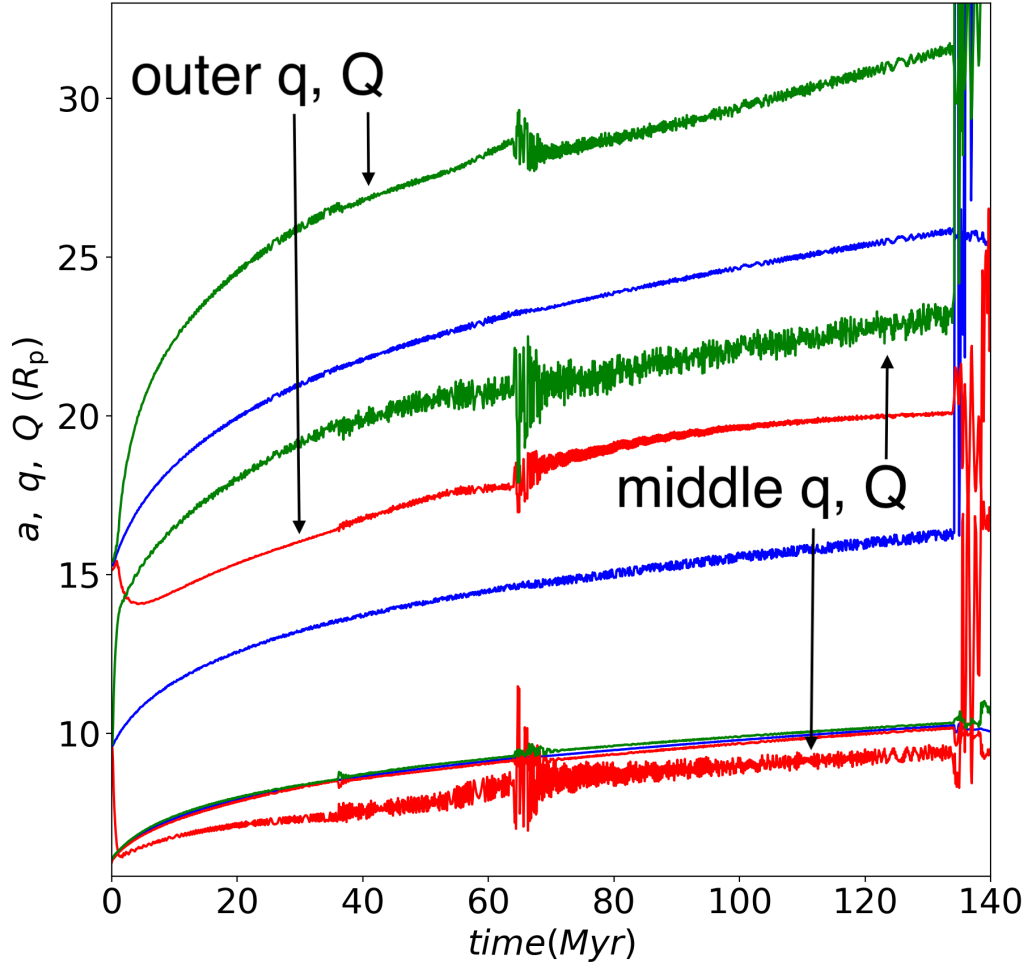


Figure 5.1: Dynamical instability among an initially resonant chain of satellites. We plot semimajor axis  $a$  (blue), periape distance  $q$  (red), and apoapse distance  $Q$  (green) for all three bodies. We used  $\frac{k_{2p}}{Q_p} = 10^{-3}$  and  $\frac{k_{2s}}{Q_s} = 6 \times 10^{-4}$  with a mass distribution of  $\log_2\left(\frac{m_2}{m_1}\right) = -4$  and  $\log_2\left(\frac{m_3}{m_1}\right) = -1.5$  and a speed-up factor  $C$  of 1000. The middle satellite's orbit almost immediately crosses both of its neighbors', and it is ejected at  $\sim 140$  Myr. We have scaled the time axis accordingly with our speed-up factor.

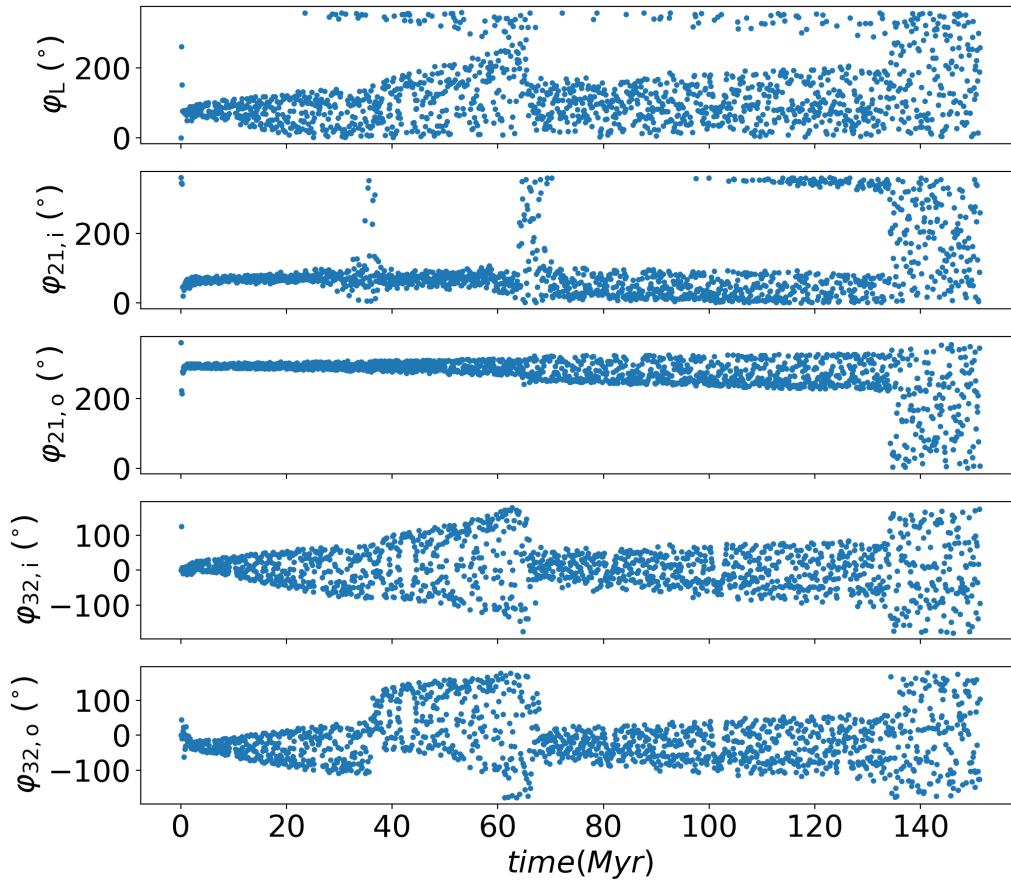


Figure 5.2: Five notable resonant arguments for the simulation in Fig. 5.1. From top down: the Laplace resonance argument  $\varphi_L$ , the inner and outer eccentricity resonance arguments  $\varphi_{21,i}$  and  $\varphi_{21,o}$ , respectively, between bodies 1 and 2, and the inner and outer eccentricity resonance arguments  $\varphi_{32,i}$  and  $\varphi_{32,o}$ , respectively, between bodies 2 and 3. All resonances are active for most of the simulation, as denoted by the libration of their arguments around fixed values. In particular, both the outer eccentricity resonance between bodies 1 and 2 and the inner eccentricity resonance between bodies 2 and 3 are active, rapidly forcing up the eccentricity of the middle satellite.

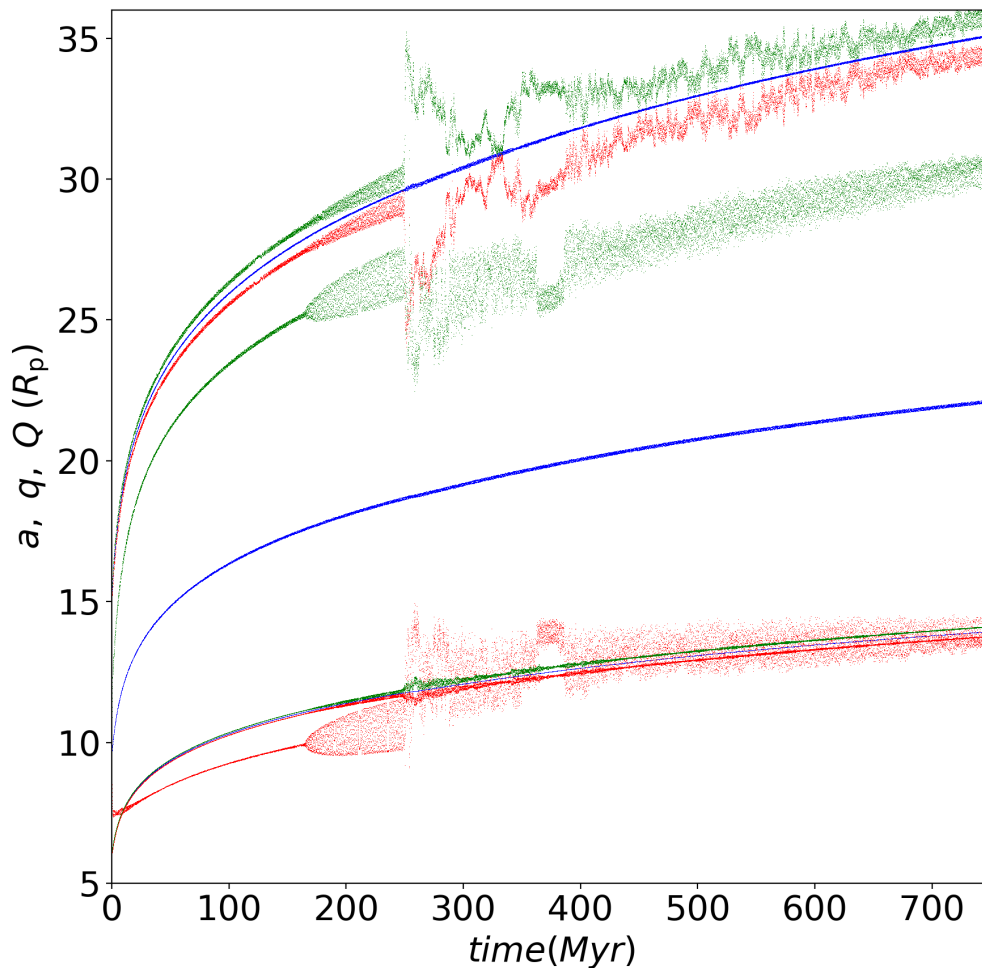


Figure 5.3: Crossing orbits, but no dynamical instability, between an initially resonant chain of satellites (compare with Fig. 5.1). We again used  $\frac{k_{2p}}{Q_p} = 10^{-3}$  and  $\frac{k_{2s}}{Q_s} = 6 \times 10^{-4}$  but with a mass distribution of  $\log_2\left(\frac{m_2}{m_1}\right) = -4$  and  $\log_2\left(\frac{m_3}{m_1}\right) = -2.5$  and a speed-up factor  $C$  of 100. The middle satellite's orbit almost immediately crosses that of the inner body, but not the outer body, and the system does not go unstable. Again scaling our time accounting for the speed-up factor, we integrated for 4 Gyr. We show only the time up to 700 Myr to highlight the interesting behavior at the beginning of the integration.

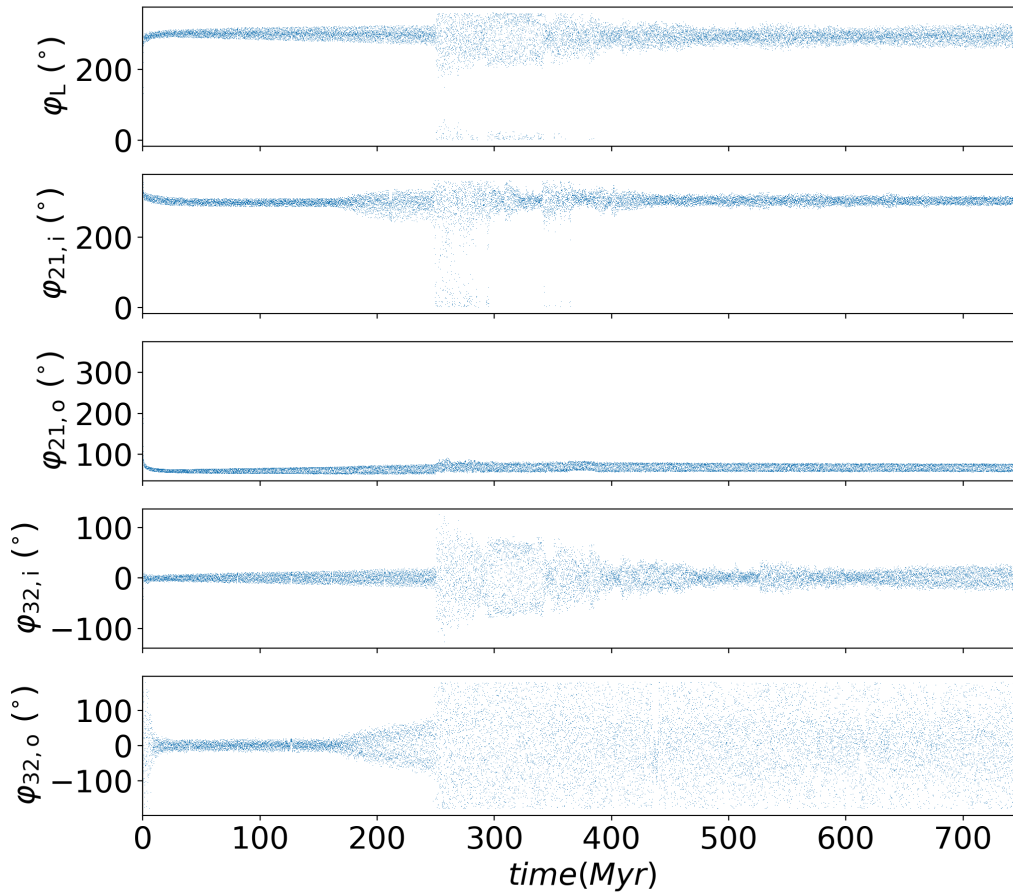


Figure 5.4: The same resonant arguments as plotted in Fig. 5.2, now for the simulation presented in Fig. 5.3. All resonances are initially active, but following a significant perturbation at  $\sim 250$  Myr,  $\varphi_{32,o}$  permanently ceases libration even as the others eventually recover.

with only three satellites, we require somewhat exotic values for both Saturn’s and Titan’s  $Q$  parameter; we only observed instabilities for  $Q_p = 100$  and  $Q_s = 1000$ . [113] has argued that such a value for  $Q_p$  could be possible, although it is over a hundred times smaller than the commonly accepted value. Titan’s  $Q$  has been estimated to be 100 [5]; we are unaware of any claim it could be as high as 1000. However, these values are ill-determined even for the contemporary bodies; there is far greater uncertainty regarding what they may have been several Gyr ago.

One might ask how the Galilean chain has remained stable if dynamical instabilities are possible. We can answer this via our criteria from Section 5.3.1. We find that instability requires a large inner mass and very small middle one, but the largest Galilean moon, Ganymede, is the outermost of the chain, and the middle moon, Europa, is a third of Ganymede’s mass (Io is half). This mass distribution is thus ill-suited for instability. Furthermore, Jupiter’s  $\frac{k_2}{Q}$  is estimated to be  $\sim 10^{-5}$  [121], which is likely too small to produce the rapid migration we argue is necessary for instability.

## 5.4.2 Future Work

Here we only study systems of three satellites; perhaps adding a fourth or fifth could lead to greater likelihood of instability. In particular, we envision a system in which the inner mass is comparatively large while the two middle masses are comparatively small; this is similar to the configuration that yielded instabilities in this work, where the middle mass was subjected to two eccentricity resonances.

Furthermore, we must show that the mergers from dynamical instabilities can produce a body that then evolves into Titan, i.e., reproduces Titan's observed eccentricity, inclination, etc. This will require several sets of integrations: the initial set to produce the instability, a new set that starts using the final conditions of the previous set with a newly merged body and explores pathways to Titan's modern orbit, and finally, start-to-finish simulations that begin with a resonant chain of satellites and end with Titan.

In addition, future work can study Hyperion's origin. This model predicts that Hyperion was formed from agglomeration of material kicked up during a merger that did not re-settle onto the new body but instead escaped into orbit around Saturn and piled up at a nearby resonance. With a suitable upgrade, HNBody will be able to simulate this process.

## Chapter 6: Conclusions

### 6.1 Summary of Results

This thesis studied the role that resonances play in the origin and evolution of rings, moons, and planets. Unsurprisingly, their role is a major one. We found the 7:6 MMR occupied by the Kepler 36 planets to be a crucial clue to its origins, which we have studied extensively in Chapter 2. We find that a model in which the two planets migrate inward through a swarm of lower-mass bodies while in resonance can reproduce the two most puzzling features of the system; the planets' close radial spacing and their massive density contrast.

Next, in Chapter 3, we offered a new set of geometric orbital elements that attempt to correct for perturbations due to oblateness, as parameterized by the  $J_2$ ,  $J_4$ , and  $J_6$  zonal harmonic coefficients. Unlike the standard epicyclic elements, our elements correctly reduce to the osculating solution in the limit that the  $J_i$  are all 0. We compare both sets of elements to a simple numerical fit and find that our analytic elements can perform at least as well as the epicyclic ones, depending on the relative values of  $J_2$  and eccentricity  $e$ .

In Chapter 4, we turn to the confinement of narrow, eccentric rings, which are known to orbit Saturn, Uranus, Neptune, and at least three small bodies. The

standard “shepherd satellite” confinement theory cannot actually explain the confinement of many known narrow rings that are believed to be shepherdless. Instead, we argue that these structures can confine themselves in the absence of any perturbing satellite by arranging themselves such that they circularize rather than spread upon losing energy due to internal collisions. We support our theory with numerical simulations of Saturn’s Titan ringlet, which we show can confine itself so long as its eccentricity remains above some critical value.

Turning from the Titan ringlet to Titan itself in Chapter 5, we investigate whether dynamical instability amongst a resonant chain of ancient satellites at Saturn could be responsible for its unusual modern-day features, i.e., its aberrantly large eccentricity, inclination, and mass. We find that such instabilities are possible, but unlikely for typically assumed values of  $\frac{k_2}{Q}$  for both Saturn and Titan.

## 6.2 Future Directions

While the Kepler 36 project initially aimed only to explain the origins of a single system of planets, we could broaden the scope to attempt to explain the overall distribution of resonances found in exoplanet systems, a problem that has attracted attention for years. Furthermore, the elements we calculate in Chapter 3 only apply to two-dimensional systems; extension to three dimensions is a clear next step. We also calculate eccentricity to zeroth order in  $e$ , which seems somewhat paradoxical; a better approach could yield a more mathematically sound – and accurate – expression for  $e$ .

Most of the remaining work, however, lies in the rings and Titan projects. To properly simulate narrow eccentric rings for hundreds of millions of years, we will need to complete our HNBody upgrade to include a viscosity force for streamlines and then verify that it can simulate self-confining ringlets as could `epi_int`. Even after the upgrade is complete, this will require a good deal of testing to ensure that HNBody agrees with theoretical results.

We discussed the remaining work for the Titan project at the end of the previous chapter and briefly repeat it here for completeness. We can broaden our parameter space to include simulations of four, possibly five satellites; we can perform start-to-finish simulations that begin with a resonant chain of satellites and finishes with the modern Titan; and we can upgrade HNBody to simulate the origins of Hyperion.

There is clearly no shortage of further work to be done. I can only hope that this is a good start.

### 6.3 Facilities and Software used in this Thesis

1. HNDrag, Chapters 2, 3, and 5 [14]
2. `epi_int`, Chapter 4 [4]
3. `exoplanet.eu` catalog, Chapter 2
4. `Deepthought2`, the UMD High Performance Computing Cluster, Chapters 2 and 5

## Bibliography

- [1] Eric D. Lopez and Jonathan J. Fortney. The Role of Core Mass in Controlling Evaporation: The Kepler Radius Distribution and the Kepler-36 Density Dichotomy. *ApJ*, 776(1):2, Oct 2013.
- [2] M. Gruberbauer, D. B. Guenther, K. MacLeod, and T. Kallinger. Bayesian asteroseismology of 23 solar-like Kepler targets. *MNRAS*, 435(1):242–254, October 2013.
- [3] N. Borderies, P. Goldreich, and S. Tremaine. The dynamics of elliptical rings. *AJ*, 88:1560–1568, October 1983.
- [4] Joseph M. Hahn and Joseph N. Spitale. An N-body Integrator for Gravitating Planetary Rings, and the Outer Edge of Saturn’s B Ring. *ApJ*, 772(2):122, August 2013.
- [5] C. D. Murray and S. F. Dermott. *Solar system dynamics*. Cambridge University Pres, 1999.
- [6] John M. A. Danby. *Fundamentals of celestial mechanics*. Willmann-Bell, Inc., 1992.
- [7] Delambre, J. Memoires de l’academie royale des sciences (turin). volume T.5=1790-1791 (1793), page 143. 1790. <https://www.biodiversitylibrary.org/bibliography/7823> — Formerly: Melanges de la Philosophie et de Mathematique de la Société Royale de Turin — Continued as: Memorie della (Reale) Accademia delle Scienze di Torino.
- [8] Brett Gladman, Martin Duncan, and Jeff Candy. Symplectic integrators for long-term integrations in celestial mechanics. *Celestial Mechanics and Dynamical Astronomy*, 52(3):221–240, September 1991.
- [9] J. M. San-Serna and M. P. Calvo. *Numerical Hamiltonian Problems*. Chapman and Hall, 1994.

- [10] R. D. Ruth. A Canonical Integration Technique. *IEEE Transactions on Nuclear Science*, 30(4):2669, August 1983.
- [11] Etienne Forest and Ronald D. Ruth. Fourth-order symplectic integration. *Physica D Nonlinear Phenomena*, 43(1):105–117, May 1990.
- [12] Haruo Yoshida. Construction of higher order symplectic integrators. *Physics Letters A*, 150(5-7):262–268, November 1990.
- [13] J. A. Burns. Elementary derivation of the perturbation equations of celestial mechanics. *American Journal of Physics*, 44(10):944–949, October 1976.
- [14] K. P. Rauch and D. P. Hamilton. The HNBODY Package for Symplectic Integration of Nearly-Keplerian Systems. In *AAS/Division of Dynamical Astronomy Meeting #33*, volume 33 of *AAS/Division of Dynamical Astronomy Meeting*, page 08.02, Sep 2002.
- [15] S. J. Peale. Orbital resonance in the solar system. *Annu. Rev. Astron. Astr.*, 14:215–246, January 1976.
- [16] R. Greenberg. Orbit - orbit resonances in the solar system: Varieties and similarities. *Vistas in Astronomy*, 21(3):209–239, January 1977.
- [17] S. J. Peale. *Orbital resonances, unusual configurations and exotic rotation states among planetary satellites*, pages 159–223. 1986.
- [18] Renu Malhotra. *Some Aspects of the Dynamics of Orbit Orbit Resonances in the Uranian Satellite System*. PhD thesis, Cornell Univ., Ithaca, NY., January 1988.
- [19] Joshua A. Carter, Eric Agol, William J. Chaplin, Sarbani Basu, Timothy R. Bedding, Lars A. Buchhave, Jørgen Christensen-Dalsgaard, Katherine M. Deck, Yvonne Elsworth, Daniel C. Fabrycky, Eric B. Ford, Jonathan J. Fortney, Steven J. Hale, Rasmus Handberg, Saskia Hekker, Matthew J. Holman, Daniel Huber, Christopher Karoff, Steven D. Kawaler, Hans Kjeldsen, Jack J. Lissauer, Eric D. Lopez, Mikkel N. Lund, Mia Lundkvist, Travis S. Metcalfe, Andrea Miglio, Leslie A. Rogers, Dennis Stello, William J. Borucki, Steve Bryson, Jessie L. Christiansen, William D. Cochran, John C. Geary, Ronald L. Gilliland, Michael R. Haas, Jennifer Hall, Andrew W. Howard, Jon M. Jenkins, Todd Klaus, David G. Koch, David W. Latham, Phillip J. MacQueen, Dimitar Sasselov, Jason H. Steffen, Joseph D. Twicken, and Joshua N. Winn. Kepler-36: A Pair of Planets with Neighboring Orbits and Dissimilar Densities. *Science*, 337(6094):556, Aug 2012.
- [20] Eric D. Lopez, Jonathan J. Fortney, and Neil Miller. How Thermal Evolution and Mass-loss Sculpt Populations of Super-Earths and Sub-Neptunes: Application to the Kepler-11 System and Beyond. *ApJ*, 761(1):59, Dec 2012.

- [21] James E. Owen and Timothy. D. Morton. The Initial Physical Conditions of Kepler-36 b and c. *ApJ*, 819(1):L10, Mar 2016.
- [22] Peter Bodenheimer, David J. Stevenson, Jack J. Lissauer, and Gennaro D’Angelo. New Formation Models for the Kepler-36 System. *ApJ*, 868(2):138, Dec 2018.
- [23] Sean N. Raymond, Thibault Boulet, Andre Izidoro, Leandro Esteves, and Bertram Bitsch. Migration-driven diversity of super-Earth compositions. *MNRAS*, 479(1):L81–L85, Sep 2018.
- [24] Alice C. Quillen, Eva Bodman, and Alexander Moore. Origin scenarios for the Kepler 36 planetary system. *MNRAS*, 435(3):2256–2267, Nov 2013.
- [25] Gennaro D’Angelo, Willy Kley, and Thomas Henning. Orbital Migration and Mass Accretion of Protoplanets in Three-dimensional Global Computations with Nested Grids. *ApJ*, 586(1):540–561, Mar 2003.
- [26] Gennaro D’Angelo and Stephen H. Lubow. Evolution of Migrating Planets Undergoing Gas Accretion. *ApJ*, 685(1):560–583, Sep 2008.
- [27] W. Kley and R. P. Nelson. Planet-Disk Interaction and Orbital Evolution. *ARA&A*, 50:211–249, Sep 2012.
- [28] Hidekazu Tanaka, Taku Takeuchi, and William R. Ward. Three-Dimensional Interaction between a Planet and an Isothermal Gaseous Disk. I. Corotation and Lindblad Torques and Planet Migration. *ApJ*, 565(2):1257–1274, Feb 2002.
- [29] Peter Goldreich, Yoram Lithwick, and Re’em Sari. Final Stages of Planet Formation. *ApJ*, 614(1):497–507, October 2004.
- [30] C. Hayashi. Structure of the Solar Nebula, Growth and Decay of Magnetic Fields and Effects of Magnetic and Turbulent Viscosities on the Nebula. *Progress of Theoretical Physics Supplement*, 70:35–53, January 1981.
- [31] M. Podolak and S. Zucker. A note on the snow line in protostellar accretion disks. *Meteoritics and Planetary Science*, 39(11):1859–1868, November 2004.
- [32] Rebecca G. Martin and Mario Livio. On the evolution of the snow line in protoplanetary discs. *MNRAS*, 425(1):L6–L9, September 2012.
- [33] Renu Malhotra. Orbital Resonances in the Solar Nebula: Strengths and Weaknesses. *Icarus*, 106(1):264–273, Nov 1993.
- [34] I. Adachi, C. Hayashi, and K. Nakazawa. The gas drag effect on the elliptical motion of a solid body in the primordial solar nebula. *Progress of Theoretical Physics*, 56:1756–1771, December 1976.

- [35] Ke Zhang and Douglas P. Hamilton. Orbital resonances in the inner neptunian system. II. Resonant history of Proteus, Larissa, Galatea, and Despina. *Icarus*, 193(1):267–282, Jan 2008.
- [36] D. Adams. *The Hitchhiker’s Guide to the Galaxy*. 1979.
- [37] J. Wisdom. The resonance overlap criterion and the onset of stochastic behavior in the restricted three-body problem. *AJ*, 85:1122–1133, Aug 1980.
- [38] Beibei Liu, Chris W. Ormel, and Douglas N. C. Lin. Dynamical rearrangement of super-Earths during disk dispersal. I. Outline of the magnetospheric rebound model. *A&A*, 601:A15, May 2017.
- [39] Yoram Lithwick and Yanqin Wu. Resonant Repulsion of Kepler Planet Pairs. *ApJ*, 756(1):L11, September 2012.
- [40] R. Greenberg. Apsidal precession of orbits about an oblate planet. *AJ*, 86:912–914, June 1981.
- [41] Nicole Borderies-Rappaport and Pierre-Yves Longaretti. Test Particle Motion around an Oblate Planet. *Icarus*, 107(1):129–141, Jan 1994.
- [42] B. D. Tapley, M. M. Watkins, J. C. Ries, G. W. Davis, R. J. Eanes, S. R. Poole, H. J. Rim, B. E. Schutz, C. K. Shum, R. S. Nerem, F. J. Lerch, J. A. Marshall, S. M. Klosko, N. K. Pavlis, and R. G. Williamson. The Joint Gravity Model 3. *J. Geophys. Res.*, 101(B12):28,029–28,049, December 1996.
- [43] L. Iess, B. Militzer, Y. Kaspi, P. Nicholson, D. Durante, P. Racioppa, A. Anabtawi, E. Galanti, W. Hubbard, M. J. Mariani, P. Tortora, S. Wahl, and M. Zannoni. Measurement and implications of Saturn’s gravity field and ring mass. *Science*, 364(6445):aat2965, June 2019.
- [44] M. Podolak and R. Helled. What Do We Really Know about Uranus and Neptune? *ApJ*, 759(2):L32, November 2012.
- [45] T. Gehrels, L. R. Baker, E. Beshore, C. Blenman, J. J. Burke, N. D. Castillo, B. Dacosta, J. Degewij, L. R. Doose, J. W. Fountain, J. Gotobed, C. E. Kenknight, R. Kingston, G. McLaughlin, R. McMillan, R. Murphy, P. H. Smith, C. P. Stoll, R. N. Strickland, M. G. Tomasko, M. P. Wijesinghe, D. L. Coffeen, and L. W. Esposito. Imaging Photopolarimeter on Pioneer Saturn. *Science*, 207(4429):434–439, January 1980.
- [46] B. A. Smith, L. Soderblom, R. M. Batson, P. M. Bridges, J. L. Inge, H. Marsursky, E. Shoemaker, R. F. Beebe, J. Boyce, G. Briggs, A. Bunker, S. A. Collins, C. Hansen, T. V. Johnson, J. L. Mitchell, R. J. Terrile, A. F. Cook, J. N. Cuzzi, J. B. Pollack, G. E. Danielson, A. P. Ingersoll, M. E. Davies, G. E. Hunt, D. Morrison, T. Owen, C. Sagan, J. Veverka, R. Strom, and V. E. Suomi. A New Look at the Saturn System: The Voyager 2 Images. *Science*, 215(4532):504–537, January 1982.

- [47] J. A. Bastin and D. H. Smith. Saturn's ringlets. *Moon and Planets*, 26(1):97–100, February 1982.
- [48] C. C. Porco. Narrow rings: Observations and theory. *Advances in Space Research*, 10(1):221–229, January 1990.
- [49] Philip D. Nicholson, Richard G. French, Matthew M. Hedman, Essam A. Marouf, and Joshua E. Colwell. Noncircular features in Saturn's rings I: The edge of the B ring. *Icarus*, 227:152–175, January 2014.
- [50] Philip D. Nicholson, Richard G. French, Colleen A. McGhee-French, Matthew M. Hedman, Essam A. Marouf, Joshua E. Colwell, Katherine Longergan, and Talia Sepersky. Noncircular features in Saturn's rings II: The C ring. *Icarus*, 241:373–396, October 2014.
- [51] J. L. Elliot and P. D. Nicholson. The rings of Uranus. In R. Greenberg and A. Brahic, editors, *IAU Colloq. 75: Planetary Rings*, pages 25–72, January 1984.
- [52] Ellis D. Miner, Randii R. Wessen, and Jeffrey N. Cuzzi. *Planetary Ring Systems*. 2007.
- [53] Linda J. Horn, John Hui, Arthur L. Lane, and Joshua E. Colwell. Observations of Neptunian rings by Voyager Photopolarimeter Experiment. *Geophys. Res. Lett.*, 17(10):1745–1748, September 1990.
- [54] Carolyn C. Porco. An Explanation for Neptune's Ring Arcs. *Science*, 253(5023):995–1001, August 1991.
- [55] J. L. Elliot, E. Dunham, and D. Mink. The rings of Uranus. *Nature*, 267(5609):328–330, May 1977.
- [56] R. L. Millis and L. H. Wasserman. The occultation of BD -15 3969 by the rings of Uranus. *AJ*, 83:993–998, August 1978.
- [57] P. D. Nicholson, S. E. Persson, K. Matthews, P. Goldreich, and G. Neugebauer. The rings of Uranus: results of the 10 April 1978 occultation. *AJ*, 83:1240–1248, October 1978.
- [58] J. L. Elliot, J. A. Frogel, J. H. Elias, I. S. Glass, R. G. French, D. J. Mink, and W. Liller. The 20 March 1980 occultation by the Uranian rings. *AJ*, 86:127–134, January 1981.
- [59] J. L. Elliot, R. G. French, J. A. Frogel, J. H. Elias, D. J. Mink, and W. Liller. Orbits of nine Uranian rings. *AJ*, 86:444–455, March 1981.
- [60] J. L. Elliot, J. H. Elias, R. G. French, Jay A. Frogel, W. Liller, K. Matthews, K. J. Meech, D. J. Mink, P. D. Nicholson, and B. Sicardy. The rings of Uranus: Occultation profiles from three observatories. *Icarus*, 56(2):202–208, November 1983.

- [61] B. A. Smith, L. A. Soderblom, R. Beebe, D. Bliss, J. M. Boyce, A. Brahic, G. A. Briggs, R. H. Brown, S. A. Collins, A. F. Cook, S. K. Croft, J. N. Cuzzi, G. E. Danielson, M. E. Davies, T. E. Dowling, D. Godfrey, C. J. Hansen, C. Harris, G. E. Hunt, A. P. Ingersoll, T. V. Johnson, R. J. Krauss, H. Masursky, D. Morrison, T. Owen, J. B. Plescia, J. B. Pollack, C. C. Porco, K. Rages, C. Sagan, E. M. Shoemaker, L. A. Sromovsky, C. Stoker, R. G. Strom, V. E. Suomi, S. P. Synnott, R. J. Terrile, P. Thomas, W. R. Thompson, and J. Veverka. Voyager 2 in the Uranian System: Imaging Science Results. *Science*, 233(4759):43–64, July 1986.
- [62] Mark R. Showalter and Jack J. Lissauer. The Second Ring-Moon System of Uranus: Discovery and Dynamics. *Science*, 311(5763):973–977, February 2006.
- [63] J. L. Elliot, D. J. Mink, J. H. Elias, R. L. Baron, E. Dunham, J. E. Pin-  
gree, R. G. French, W. Liller, P. D. Nicholson, T. J. Jones, and O. G. Franz. No evidence of rings around Neptune. *Nature*, 294(5841):526–529, December 1981.
- [64] W. B. Hubbard, G. H. Rieke, M. J. Lebofsky, B. H. Zellner, H. J. Reitsema, L. A. Lebofsky, H. Campins, F. Vilas, D. J. Tholen, and M. Alvarez. Negative Results of Occultation Searches for Neptunian Rings. In *Bulletin of the American Astronomical Society*, volume 13, page 728, June 1981.
- [65] B. Sicardy, F. Roques, A. Brahic, J. P. Maillard, D. P. Cruikshank, and E. E. Becklin. Limit of Detection of Faint Rings around Uranus and Neptune from Stellar Occultations. In *Bulletin of the American Astronomical Society*, volume 15, page 816, June 1983.
- [66] F. Vilas, W. B. Hubbard, J. E. Frecker, D. M. Hunten, T. Gehrels, L. A. Lebofsky, B. A. Smith, D. J. Tholen, B. H. Zellner, W. Wisniewski, J. A. Gehrels, B. Capron, H. J. Reitsema, M. D. Waterworth, H. H. Fu, H. H. Wu, H. P. Avey, and A. A. Page. Occultations by Pallas (83/5/29) and Neptune (83/6/15) - Preliminary Results. In *Bulletin of the American Astronomical Society*, volume 15, page 816, June 1983.
- [67] W. B. Hubbard, A. Brahic, P. Bouchet, L. R. Elicer, R. Haefner, J. Manfroid, F. Roques, B. Sicardy, and F. Vilas. Occultation detection of a Neptune ring segment. *Journal of Geophysical Research Supplement*, 90:35–37, November 1985.
- [68] J. Manfroid, R. Haefner, and P. Bouchet. New evidence for a ring around Neptune. *A&A*, 157(1):L3–L5, March 1986.
- [69] B. Sicardy, F. Roques, and A. Brahic. Neptune’s rings, 1983-1989: Ground-based stellar occultation observations I. Ring-like arc detections. *Icarus*, 89(2):220–243, February 1991.

- [70] Christophe Dumas, Richard J. Terrile, Bradford A. Smith, Glenn Schneider, and E. E. Becklin. Stability of Neptune’s ring arcs in question. *Nature*, 400(6746):733–735, August 1999.
- [71] F. Braga-Ribas, B. Sicardy, J. L. Ortiz, C. Snodgrass, F. Roques, R. Vieira-Martins, J. I. B. Camargo, M. Assafin, R. Duffard, E. Jehin, J. Pollock, R. Leiva, M. Emilio, D. I. Machado, C. Colazo, E. Lellouch, J. Skottfelt, M. Gillon, N. Ligier, L. Maquet, G. Benedetti-Rossi, A. Ramos Gomes, P. Kervella, H. Monteiro, R. Sfair, M. El Moutamid, G. Tancredi, J. Spagnotto, A. Maury, N. Morales, R. Gil-Hutton, S. Roland, A. Ceretta, S. H. Gu, X. B. Wang, K. Harpsøe, M. Rabus, J. Manfroid, C. Opitom, L. Vanzi, L. Mehret, L. Lorenzini, E. M. Schneiter, R. Melia, J. Lecacheux, F. Colas, F. Vachier, T. Widemann, L. Almenares, R. G. Sandness, F. Char, V. Perez, P. Lemos, N. Martinez, U. G. Jørgensen, M. Dominik, F. Roig, D. E. Reichart, A. P. Lacluyze, J. B. Haislip, K. M. Ivarsen, J. P. Moore, N. R. Frank, and D. G. Lambas. A ring system detected around the Centaur (10199) Chariklo. *Nature*, 508(7494):72–75, April 2014.
- [72] J. L. Ortiz, R. Duffard, N. Pinilla-Alonso, A. Alvarez-Cand al, P. Santos-Sanz, N. Morales, E. Fernández-Valenzuela, J. Licandro, A. Campo Bagatin, and A. Thirouin. Possible ring material around centaur (2060) Chiron. *A&A*, 576:A18, April 2015.
- [73] J. L. Ortiz, P. Santos-Sanz, B. Sicardy, G. Benedetti-Rossi, D. Bérard, N. Morales, R. Duffard, F. Braga-Ribas, U. Hopp, C. Ries, V. Nascimbeni, F. Marzari, V. Granata, A. Pál, C. Kiss, T. Pribulla, R. Komžík, K. Hornoch, P. Pravec, P. Bacci, M. Maestripieri, L. Nerli, L. Mazzei, M. Bachini, F. Martinelli, G. Succi, F. Ciabattari, H. Mikuz, A. Carbognani, B. Gaehrken, S. Mottola, S. Hellmich, F. L. Rommel, E. Fernández-Valenzuela, A. Campo Bagatin, S. Cikota, A. Cikota, J. Lecacheux, R. Vieira-Martins, J. I. B. Camargo, M. Assafin, F. Colas, R. Behrend, J. Desmars, E. Meza, A. Alvarez-Candal, W. Beisker, A. R. Gomes-Junior, B. E. Morgado, F. Roques, F. Vachier, J. Berthier, T. G. Mueller, J. M. Madiedo, O. Unsalan, E. Sonbas, N. Karaman, O. Erece, D. T. Koseoglu, T. Ozisik, S. Kalkan, Y. Guney, M. S. Niaei, O. Satir, C. Yesilyaprak, C. Puskullu, A. Kabas, O. Demircan, J. Alikakos, V. Charmandaris, G. Leto, J. Ohlert, J. M. Christille, R. Szakáts, A. Takácsné Farkas, E. Varga-Verebélyi, G. Marton, A. Marciniak, P. Bartczak, T. Santana-Ros, M. Butkiewicz-Bak, G. Dudziński, V. Alí-Lagoa, K. Gazeas, L. Tzouganatos, N. Paschalis, V. Tsamis, A. Sánchez-Lavega, S. Pérez-Hoyos, R. Hueso, J. C. Guirado, V. Peris, and R. Iglesias-Marzoa. The size, shape, density and ring of the dwarf planet Haumea from a stellar occultation. *Nature*, 550(7675):219–223, October 2017.
- [74] Larry W. Esposito. Planetary rings. *Reports on Progress in Physics*, 65(12):1741–1783, December 2002.

- [75] P. Goldreich and S. Tremaine. Towards a theory for the Uranian rings. *Nature*, 277:97–99, January 1979.
- [76] N. Borderies, P. Goldreich, and S. Tremaine. Sharp edges of planetary rings. *Nature*, 299:209–211, September 1982.
- [77] Nicole Borderies, Peter Goldreich, and Scott Tremaine. Nonlinear density waves in planetary rings. *Icarus*, 68(3):522–533, December 1986.
- [78] N. Borderies, P. Goldreich, and S. Tremaine. The formation of sharp edges in planetary rings by nearby satellites. *Icarus*, 80(2):344–360, August 1989.
- [79] Ignacio Mosqueira. Local Simulations of Perturbed Dense Planetary Rings. *Icarus*, 122(1):128–152, July 1996.
- [80] Ignacio Mosqueira, Paul R. Estrada, and Leigh Brookshaw. Hydrodynamical Simulations of Narrow Planetary Rings. I. Scaling. *Icarus*, 139(2):260–285, June 1999.
- [81] E. I. Chiang and P. Goldreich. Apse Alignment of Narrow Eccentric Planetary Rings. *ApJ*, 540(2):1084–1090, September 2000.
- [82] Ignacio Mosqueira and Paul R. Estrada. Apse Alignment of the Uranian Rings. *Icarus*, 158(2):545–556, August 2002.
- [83] J. N. Cuzzi, A. D. Whizin, R. C. Hogan, A. R. Dobrovolskis, L. Dones, M. R. Showalter, J. E. Colwell, and J. D. Scargle. Saturn’s F Ring core: Calm in the midst of chaos. *Icarus*, 232:157–175, April 2014.
- [84] Joseph N. Spitale. Saturn’s Misbegotten Moonlets. In *AAS/Division of Dynamical Astronomy Meeting #48*, AAS/Division of Dynamical Astronomy Meeting, page 400.04, June 2017.
- [85] Ke Zhang, Douglas P. Hamilton, and Soko Matsumura. Secular Orbital Evolution of Compact Planet Systems. *ApJ*, 778(1):6, November 2013.
- [86] D. C. Richardson. Tree Code Simulations of Planetary Rings. *MNRAS*, 269:493, July 1994.
- [87] Matthew S. Tiscareno, Joseph A. Burns, Philip D. Nicholson, Matthew M. Hedman, and Carolyn C. Porco. Cassini imaging of Saturn’s rings. II. A wavelet technique for analysis of density waves and other radial structure in the rings. *Icarus*, 189(1):14–34, July 2007.
- [88] J. Salmon, S. Charnoz, A. Crida, and A. Brahic. Long-term and large-scale viscous evolution of dense planetary rings. *Icarus*, 209(2):771–785, October 2010.

- [89] Thomas Rimlinger, Douglas Hamilton, and Joseph M. Hahn. Ringing in an HNBody Upgrade. In *AAS/Division of Dynamical Astronomy Meeting #48*, AAS/Division of Dynamical Astronomy Meeting, page 205.05, June 2017.
- [90] R. A. Jacobson, P. G. Antreasian, J. J. Bordi, K. E. Criddle, R. Ionasescu, J. B. Jones, R. A. Mackenzie, M. C. Meek, D. Parcher, F. J. Pelletier, Jr. Owen, W. M., D. C. Roth, I. M. Roundhill, and J. R. Stauch. The Gravity Field of the Saturnian System from Satellite Observations and Spacecraft Tracking Data. *AJ*, 132(6):2520–2526, December 2006.
- [91] Yasuhito Sekine and Hidenori Genda. Giant impacts in the Saturnian system: A possible origin of diversity in the inner mid-sized satellites. *Planet. Space Sci.*, 63:133–138, April 2012.
- [92] Robin M. Canup. Origin of Saturn’s rings and inner moons by mass removal from a lost Titan-sized satellite. *Nature*, 468(7326):943–946, December 2010.
- [93] J. I. Lunine and D. J. Stevenson. Formation of the galilean satellites in a gaseous nebula. *Icarus*, 52(1):14–39, October 1982.
- [94] Jr. Graboske, H. C., J. B. Pollack, A. S. Grossman, and R. J. Olness. The structure and evolution of Jupiter: the fluid contraction stage. *ApJ*, 199:265–281, July 1975.
- [95] P. Bodenheimer, A. S. Grossman, W. M. Decampli, G. Marcy, and J. B. Pollack. Calculations of the evolution of the giant planets. *Icarus*, 41(2):293–308, February 1980.
- [96] Robin M. Canup and William R. Ward. Formation of the Galilean Satellites: Conditions of Accretion. *AJ*, 124(6):3404–3423, December 2002.
- [97] Y. Alibert, O. Mousis, and W. Benz. Modeling the Jovian subnebula. I. Thermodynamic conditions and migration of proto-satellites. *A&A*, 439(3):1205–1213, September 2005.
- [98] Robin M. Canup and William R. Ward. A common mass scaling for satellite systems of gaseous planets. *Nature*, 441(7095):834–839, June 2006.
- [99] Y. Alibert and O. Mousis. Formation of Titan in Saturn’s subnebula: constraints from Huygens probe measurements. *A&A*, 465(3):1051–1060, April 2007.
- [100] T. Sasaki, G. R. Stewart, and S. Ida. Origin of the Different Architectures of the Jovian and Saturnian Satellite Systems. *ApJ*, 714(2):1052–1064, May 2010.
- [101] T. Ronnet and A. Johansen. Formation of moon systems around giant planets. Capture and ablation of planetesimals as foundation for a pebble accretion scenario. *A&A*, 633:A93, January 2020.

- [102] Yuhito Shibaïke, Satoshi Okuzumi, Takanori Sasaki, and Shigeru Ida. Satellitesimal Formation via Collisional Dust Growth in Steady Circumplanetary Disks. *ApJ*, 846(1):81, September 2017.
- [103] P. R. Estrada, I. Mosqueira, J. J. Lissauer, G. D’Angelo, and D. P. Cruikshank. *Formation of Jupiter and Conditions for Accretion of the Galilean Satellites*, page 27. 2009.
- [104] A. Crida and S. Charnoz. Formation of Regular Satellites from Ancient Massive Rings in the Solar System. *Science*, 338(6111):1196, November 2012.
- [105] Craig B. Agnor and Douglas P. Hamilton. Neptune’s capture of its moon Triton in a binary-planet gravitational encounter. *Nature*, 441(7090):192–194, May 2006.
- [106] Scott Tremaine, Jihad Touma, and Fathi Namouni. Satellite Dynamics on the Laplace Surface. *AJ*, 137(3):3706–3717, March 2009.
- [107] Erik Asphaug and Andreas Reufer. Late origin of the Saturn system. *Icarus*, 223(1):544–565, March 2013.
- [108] Luciano Iess, Robert A. Jacobson, Marco Ducci, David J. Stevenson, Jonathan I. Lunine, John W. Armstrong, Sami W. Asmar, Paolo Racioppa, Nicole J. Rappaport, and Paolo Tortora. The Tides of Titan. *Science*, 337(6093):457, July 2012.
- [109] Valéry Lainey, Robert A. Jacobson, Radwan Tajeddine, Nicholas J. Cooper, Carl Murray, Vincent Robert, Gabriel Tobie, Tristan Guillot, Stéphane Mathis, Françoise Remus, Josselin Desmars, Jean-Eudes Arlot, Jean-Pierre De Cuyper, Véronique Dehant, Dan Pascu, William Thuillot, Christophe Le Poncin-Lafitte, and Jean-Paul Zahn. New constraints on Saturn’s interior from Cassini astrometric data. *Icarus*, 281:286–296, January 2017.
- [110] Ke Zhang and Francis Nimmo. Recent orbital evolution and the internal structures of Enceladus and Dione. *Icarus*, 204(2):597–609, December 2009.
- [111] Jennifer Meyer and Jack Wisdom. Tidal evolution of Mimas, Enceladus, and Dione. *Icarus*, 193(1):213–223, January 2008.
- [112] S. J. Peale, P. Cassen, and R. T. Reynolds. Tidal dissipation, orbital evolution, and the nature of Saturn’s inner satellites. *Icarus*, 43(1):65–72, July 1980.
- [113] Valéry Lainey, Luis Gomez Casajus, Jim Fuller, Marco Zannoni, Paolo Tortora, Nicholas Cooper, Carl Murray, Dario Modenini, Ryan S. Park, Vincent Robert, and Qingfeng Zhang. Resonance locking in giant planets indicated by the rapid orbital expansion of Titan. *Nature Astronomy*, June 2020.

- [114] Jim Fuller, Jing Luan, and Eliot Quataert. Resonance locking as the source of rapid tidal migration in the Jupiter and Saturn moon systems. *MNRAS*, 458(4):3867–3879, June 2016.
- [115] Ayano Nakajima, Shigeru Ida, Jun Kimura, and Ramon Brasser. Orbital evolution of Saturn’s mid-sized moons and the tidal heating of Enceladus. *Icarus*, 317:570–582, January 2019.
- [116] R. Malhotra and S. F. Dermott. The role of secondary resonances in the orbital history of Miranda. *Icarus*, 85(2):444–480, June 1990.
- [117] Adam P. Showman, David J. Stevenson, and Renu Malhotra. Coupled Orbital and Thermal Evolution of Ganymede. *Icarus*, 129(2):367–383, October 1997.
- [118] William M. Kaula. Tidal Dissipation by Solid Friction and the Resulting Orbital Evolution. *Reviews of Geophysics and Space Physics*, 2:661–685, January 1964.
- [119] S. J. Peale and P. Cassen. Contribution of tidal dissipation to lunar thermal history. *Icarus*, 36(2):245–269, November 1978.
- [120] Junko Kominami and Shigeru Ida. The Effect of Tidal Interaction with a Gas Disk on Formation of Terrestrial Planets. *Icarus*, 157(1):43–56, May 2002.
- [121] Valéry Lainey, Jean-Eudes Arlot, Özgür Karatekin, and Tim van Hoolst. Strong tidal dissipation in Io and Jupiter from astrometric observations. *Nature*, 459(7249):957–959, June 2009.